공학박사 학위논문

Manipulation of primary nanocrystallization and mechanical responses in Al−TM−RE metallic glasses

Al−TM−RE 비정질 합금의 나노결정화 거동 및 기계적 특성의 제어

2020 년 2 월

서울대학교 대학원
재료공학부
김 완

Abstract

Manipulation of primary nanocrystallization and mechanical responses in Al-TM-RE metallic glasses.

Wan Kim
Department of Materials Science and Engineering
College of Engineering
Seoul National University

Metallic glass possesses outstanding mechanical properties such as high strength, large elastic limit, high wear resistance and long fatigue life-time [1,2]. However, the lack of intrinsic deformation mechanism makes the metallic glass be susceptible to localized displacement highly concentrated in narrow shear bands. It has been revealed that the collective activation of shear transformation zones (STZ) is responsible for the macroscopic shear displacements and the catastrophic failure of metallic glass. Thus, it is important to understand the relation between the atomic/nano-scaled structural features with the mechanical dynamics for developing the metallic glasses with advanced plasticity. Among the various glass forming systems, Al-TM-RE systems can be considered as a good candidate for the investigation of mechanical responses depending on their structural variation.

Since the first discovery of a series of ductile Al-based metallic glasses, the

Al-rich (> 80 at%) Al-TM-RE (TM = transition metal, RE = rare earth metal) glass formers have been attracted the great attention from researchers. Al-TM-RE is the ductile metallic glass with the average strength of 1 GPa. Especially, Al-TM-RE glass formers have been highlighted due to the partial crystallization of FCC-Al. This interesting crystallization behavior only can be derived from the high Al base component (> 85 at%). At the Al-rich corner, alloys possess the high portion of Al-MRO in amorphous matrix, which can trigger the heterogeneous nucleation of FCC-Al at relatively low annealing temperature. Because of the low solubility of FCC-Al, precipitated soft FCC-Al nanocrystalline phases can cause the local solute enrichment, and ultimately act as the hard second phase which can improve the strength up to 1.5 GPa. On the other hand, the addition of RE elements stabilize the RE-centered quasi-equivalent clusters which can enhance the glass forming ability (GFA) of the system, but the system stops to show the primary crystallization behavior. Addition of the higher portion of RE elements up to the certain amount can manipulate the metallic glass with wide super-cooled liquid region. And it is possible to manufacture the Al-based metallic glass via thermo-plastic forming process. However, Al-based metallic glass with clear T_g does not produce the primary FCC-Al and deform inhomogeneously along the shear plane in the temperature range below T_g, and no distinct plastic elongation has been reported yet. Thus, to manipulate the Al-based metallic glass with good mechanical properties and high glass forming ability, it is important to understand the (1)effect of atomic level structural variation on thermal properties and crystallization behavior, (2)nucleation kinetics of primary FCC-Al crystallization and (3)deformation behavior controlled by the FCC-Al nanocrystals.

In this study, the nucleation kinetics of FCC-Al and mechanical properties of $Al_{90-x}Ni_{10}RE_x$ metallic glasses (x=2,4,6) were systematically investigated. First, to investigate the effects of RE on thermal properties of Al-based metallic glasses, various RE elements (La, Ce, Nd, Gd, Y, Er) were added in the equiatomic ratio. Based on the knowledge about RE effect on thermal properties, $Al_{90-x}Ni_{10}MM_x$ (MM = Ce-rich misch metal, x=2,4,6) alloys were chosen to study the crystallization behavior of FCC-Al. To investigate the crystallization behavior of FCC-Al in the $Al_{90-x}Ni_{10}MM_x$ glass system, microstructure of as-spun and annealed amorphous alloys was carefully analyzed by transmission electron microscopy (TEM) and in-situ synchrotron small angle X-ray scattering (SAXS). Not only the heating process, but also the cooling processing was also adapted to control the size and the number density of the FCC-Al in $Al_{88}Ni_{10}MM_2$ metallic glass. Combining with the classical nucleation theory, nucleation kinetics of FCC-Al was carefully investigated. Especially, by using the fast heating calorimetry (FDSC), incubation time for nucleation of FCC-Al were experimentally measured. XRD and TEM analysis confirmed that the measurement of the incubation time via FDSC is correct. Collection of the incubation times resulted in the TTT diagram of FCC-Al. This is the first report of the TTT diagram for the marginal Al-based metallic glasses. To confirm the accuracy of the TTT diagram, thermodynamic calculation was conducted based on the classical nucleation theory. To evaluate the relation between structural variation (RE addition effect and FCC-Al nanocrystal effect) and shear deformation behavior, nanoindentation analysis was systematically performed. Room temperature creep test was performed to reveal the interface effect on the anelastic deformation behavior. In addition, macro-scaled bending and tensile test also performed to investigate the plasticity of the Al-based metallic glasses with FCC-Al nanocrystals.

From the results of this study, crystallization behavior of FCC-Al was deeply studied and TTT-diagram that can explain the crystallization behavior of FCC-Al was obtained. It is expected that the sound understanding of the relation between mechanical properties and structural variation of Al-based MGs will contribute significantly to the new strategies for developing not only the Al-based system but also the overall glass forming systems and MG composites.

Keywords : Metallic glass, Nucleation kinetics, TTT diagram, Nanoindentation, Fast heating calorimetry.

***Student Number* :** 2014-21450

Table of Contents

List of Figures

List of Tables

List of Abbreviations

STZ	Shear transformation zone
MG	Metallic glass
TTT diagram	Time-Transition-Temperature diagram
TM	Transition metal
RE	Rare earth metal
MRO	Medium range ordering
GFA	Glass forming ability
TEM	Transmission electron microscopy
SAXS	Small angle X-ray scattering
FDSC	Fast heating calorimetry
DSC	Differential scanning calorimetry
MM	Misch metal (=$Ce_{50.19}La_{25.31}Nd_{19.5}Pr_{4.99}$)
BMG	Bulk metallic glass
FCC	Face-centered cubic structured
SAED	Selected area electro diffraction
FIB	Focused ion beam
APT	Atom probe tomography
TMA	Thermo-mechanical analysis
VFT	Vogel-Fulcher-Tammann relation
SDZ	Self-organized deformed zone
CDZ	Chaotic deformed zone
SRO	Short range ordering
XRD	X-ray diffraction

List of Symbols

Re	Resilience
σ_y	Yield strength
E	Elastic modulus
T_g	Glass transition temperature
T_x	Crystallization temperature
T_p	Crystallization peak tempeature
ΔT_x	Super cooled liquid region
τ	Incubation time
Δ	Width of random walk zone
ΔG^*	Critical activation energy for nucleation
k	Boltzmann constant (1.38064852 × 10^{-23} m^2 kg s^{-2} K^{-1})
T	Temperature
r^*	Critical nucleation size
r	Radius
β	Attachment frequency
Z	Zeldovich factor
N_s	Number of nucleation sites
D	Diffusion coefficient
Q_s	Diffusion activation energy
U	Growth rate of crystalline phase
ψ	Electronegativity
ϵ	Atomic radius of atom

$W_{A\text{-}B}$	Compound forming tendency between A and B element
m	Fragility
m_{dyn}^{r}	Dynamic fragility
ϕ	Heating rate
D_f	Fragility parameter for dynamic fragility
T_g^0	VFT temperature for dynamic fragility
h	Height variation of ribbon sample
η	Viscosity
L	Sample (ribbon) thickness
D^*	Fragility parameter for kinetic fragility
T_0	VFT temperature for kinetic fragility
m_{kin}^{v}	Kinetic fragility
H	Hardness
E_r	Reduced elastic modulus
S	Shear burst size (normalized pop-in size)
β_s	Scaling exponent
S_c	Cut-off value of S
λ_0	Topological instability parameter
C_i	Composition of i elements
T_m	Melting temperature (=liquidus temperature, T_l)
T_s	Solidus temperature
$\sigma_{\frac{s}{l}}$	Interfacial energy between solid and liquid
ΔG_v	Free volume energy

I_{SS}	Steady state nucleation rate
U	Growth rate of crystalline phase
ΔH_f	Enthalpy of fusion
ΔH_X	Enthalpy of crystallization
q	Scattering factor for small angle scattering
λ	X-ray wavelength
V_f	Volume fraction of FCC-Al in amorphous matrix
$I(q)$	Intensity of scattered X-ray beam (SAXS)
R_g	Radius of guinier
R	Radius of scatterer (or radius of FCC-Al in amorphous matrix)
E_{act}	Activation energy
T_d	Decoupling temperature
T_c	Critical temperature
X	Volume fraction of crystal in amorphous matrix
J_v	Nucleation frequency per unit volume
$f(\theta)$	Pre-catalytic factor
ρ	Density
α_i	Thermal conductivity of i
b_i	Thermal storage coefficient of i
χ	Ribbon sample thickness
ω	Atomic vibration frequency factor
C_0	Number of atoms per unit volume in phase

ΔG_m	Atomic migration energy per atom
ΔT_c	Critical undercooling
p	Applied load
R_{con}	Radius of conical tip for nanoindentation
m_{ss}	Strain rate sensitivity
$\dot{\varepsilon}$	Strain rate
h_i	Indentation depth for calculation of Kelvin model
τ_i	Retardation time for the ith anelastic process in Kelvin model
μ_0	Constant proportional to the viscosity coefficient of the last dashpot
ε_{el} & ε_{pl}	Portion of elastic & plastic deformation

Chapter 1.

Introduction

1.1. Formation of metallic glass

When the molten alloys are subjected to large undercooling conditions, limited nucleation of stable crystalline phases can extend the metastability of the system due to the suppression of the kinetically favored metastable phases. The formation of metastable phase can be expanded into the significantly wide range of microstructural options that are feasible to synthesis the new materials, especially metallic glasses (MGs). Metallic glass is the metastable amorphous solid with no long-range order [1]. Due to the lack of structural defects, metallic glasses have the higher strength than that of crystal counterparts and have the polymer level of elastic limit around 2% (figure 1.1). High strength and low elastic modulus of the metallic glass results in the high resilience ($Re = \sigma_y^2/2E$). Thus, metallic glass has been gained great attention as the future structural materials [1,2].

The solid can be determined as glass when no long-range transitional order can be detected down to 2 nm and volume fraction of crystallization in as-casted alloy is smaller than 10^{-6} [1,3]. In the solidification pathways described in schematic images shown in Fig. 1.1 (a), the solidification into the glassy state of the metastable liquid (path 2) can occur when crystallization (path 1) is bypassed. To suppress the crystallization, the given quench rate must be faster than the nucleation rate of the alloys and undercooled below the glass transition temperature where the viscosity of liquid is 10^{12} pa·s (figure 1.1.(b)). Unlike with the crystallization process, which is involved with an equilibrium phase transformation and the discontinuous change of the extensive properties, the glass transition is a continuous transformation in terms volume, enthalpy or entropy [5]. The glass transition is reversible reaction. When the glass is continuously heated above the glass transition temperature, it transforms into a super cooled liquid state. As a result of the glass transition, the viscosity of super-cooled liquid decrease by several orders of magnitude. And accelerated atomic mobility triggers the nucleation and growth of equilibrium crystallization phases in metastable glass (path 3).

As described above, the introduction of undercooled melt which can work as the key parameter for microstructural development during solidification provides an important connection between glass stability and researches related with undercooled phase. In contrast with oxide glasses metallic melts have non-directional bonding and atomic rearrangements occur very rapidly. Hence very high cooling rates (>10^5 K/s) are required to form the metallic glasses. To successfully produce the metallic glasses, various experimental approaches have been applied to achieve large undercooling before the nucleation of crystalline phases. And this let us to understand how to control the thermal pathway during solidification. Consequently, as shown in figure 1.2, it has become clear that the conditions of casting processes play a important role in determining the selection of the microstructural morphologies and solidified phases [4]. Due to the difference properties of crystals and glasses, which are resulted from their different atomic structure, selective introduction of crystalline phases and amorphous phases can optimize the properties of the alloys Thus, the flexibility in microstructural selection represents a key challenge to conduct the proper guide to the control of processing which can help us to optimize the alloy design and processing in order to achieve improved properties in metallic glasses. Thus, to develop the metallic glass with optimized properties, satisfaction of three important aspect is mandatory: 1)how to avoid the nucleation during the cooling of the liquid, 2)How to control of crystallization upon cooling of the liquid and heating of the glass.

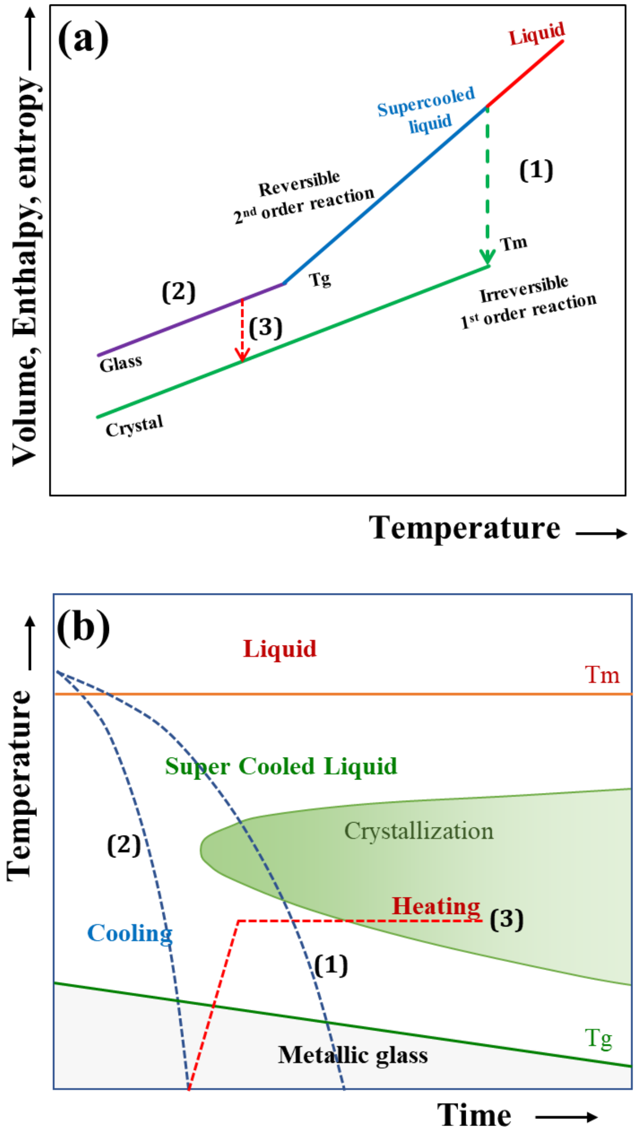

Figure 1.1. (a) Schematic diagram of the change in volume, enthalpy and entropy with temperature as an undercooled liquid quenched bypass the glass transition temperature. (b) Schematic TTT diagram and thermal pathway for the formation of crystalline phase (path 1,3) and glass (path 2)

Nucleation control

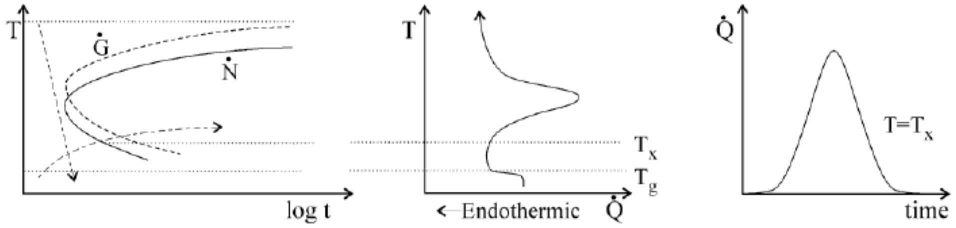

Growth control

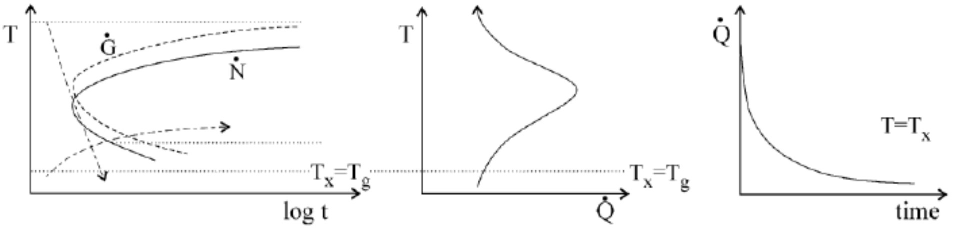

Figure 1.2. schematic images showing the kinetics of metallic glass formations (nucleation control vs growth control). Cooling and heating paths for the crystalline phase and glass formation are drown on the TTT diagram and the thermograms. (Reprinted from ref [4] with permission though “Copyright Clearance Center”)

1.2. Background of Al-based metallic glasses

Since the first discovery of Au-Si amorphous alloys, there has been an effort to extend the glass forming compositions [5]. Figure 1.3 shows the typical T_g range and mechanical properties of various metallic glass systems. Among them, Al-based MGs occupied special engineering and scientific portion because of their exceptional features related with crystallization behavior. In the 1970s, it was reported that the partially vitrified microstructure in the Al-metalloid and Al-TM (Transition metal) binary systems. [6,7]. In 1981, researchers of Tohoku university successfully prepared fully vitrified Al-(Fe,Co)-B amorphous alloys by using the melt spinning process [8]. However, these amorphous alloys in Al-TM-metalloid systems was too brittle and hence no systematic study was related to the fundamental properties were obtained. In the 1988, Y. He and co-workers reported [9] strong and ductile Al-TM-RE ternary glasses (Al->80at%). Since then, various compositions were tested to obtain the ductile Al-TM-RE amorphous alloy. As shown in figure 1.4, most of the glass forming area in Al-TM-RE system places at Al-rich corner, and they possess relatively poor GFA [10]. Recently, N.C. Wu et.al successfully manipulated the Al-based bulk metallic glass (BMG) (composition : $Al_{86}Ni_{6.75}Co_{2.25}Y_{3.25}La_{1.75}$) with 1.5 mm diameter by copper mould casting technique [11]. 1.5 mm is the best GFA in Al-based metallic glass. As an alternative method for Al-based bulk metallic glasses, Spark plasma sintering has been widely applied [12]. Through the solid-state sintering process, it is possible the solidify the powdered Al-based metallic glasses into ductile Al-based bulk metallic glass with the centimeter sized diameter. And recent study successfully casted the high-entropy Al-based BMG composite bigger than 1 cm [13].

As mentioned before, thermal properties and crystallization behavior of Al-based metallic glasses have interesting features. First, due to the coincidence of glass transition temperature and crystallization temperature, it is difficult to detect the clear T_g signal in Al-based metallic glasses by the continuous heating of different scanning calorimetry (DSC). And numerous numbers of Al-based metallic glasses possess a wide first crystallization peak at relatively low temperature. And the shallow first crystallization peak is related with the FCC-Al nanocrystalline phases which are precipitated from the amorphous matrix with the high number density (10^{21} – 10^{23} m^3). Because of the higher driving force for nucleation of $Al_{100-x}RE_x$ or $Al_{100-x}Ni_x$ compounds, primary crystallization of FCC-Al within hypereutectic composition range is unfavored. So, one must consider that the precipitation of FCC-Al is triggered by a nucleation catalyst by thermal treatment. The Al-based metallic glasses have the great potential as the future structural materials requiring high strength with relatively low density. Figure 1.5 [14] is the good explanation that shows the relation of specific strength and microstructural scale of Al alloys. As graph shows, the strength of the al alloy exponentially inversely increases with the microstructural scale of the system. when the amorphous Al alloys have the partial crystallization of FCC-Al in amorphous matrix, they can achieve the ultrahigh strength of about 1.5 GPa which are even stronger than the steels [14,15].

In addition, partial precipitation of FCC-Al cannot aggravate the corrosion resistance of the Al-based metallic glasses. And high temperature tensile test shows that Al-based metallic glasses start to show specific plasticity at the high temperature where the FCC-Al can be precipitated [16]. However, the coarsening of the FCC-Al nanocrystals and formation of brittle $Al_{100-x}RE_x$ intermetallic compound lowers the hardness [17]. And there are no reports that clearly proving the room temperature plasticity of Al-based metallic glasses composition. Thus, to utilize the Al-based metallic glass with nanocrystals for the structural application, it is urgent to confirm the FCC-Al effect on the plasticity.

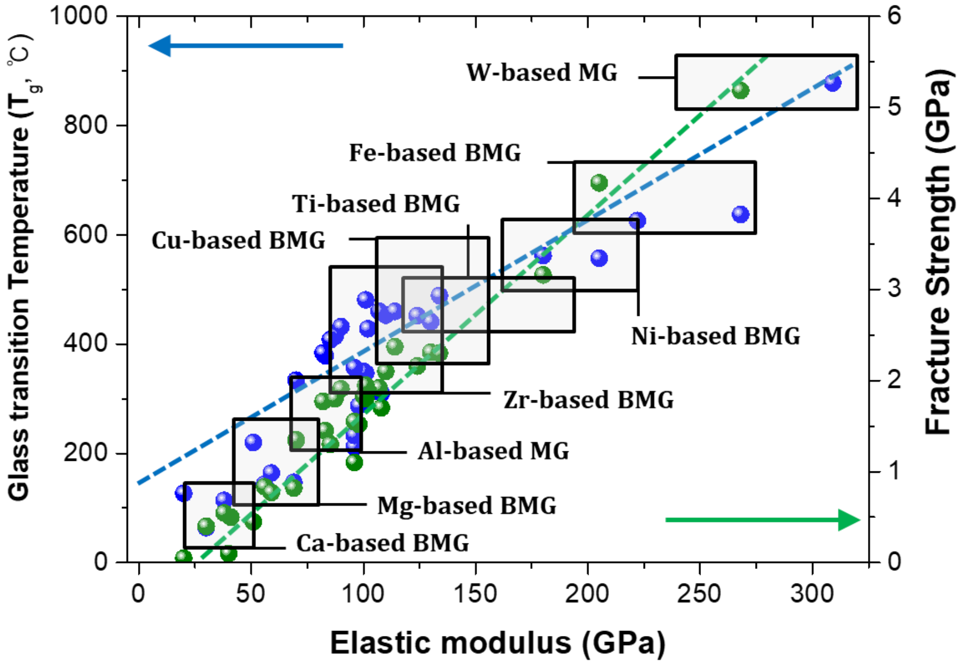

Figure 1.3. Collective data map showing relationship between the thermal properties (glass transition temperature) and mechanical properties (Fracture strength and elastic modulus) of various metallic glasses.

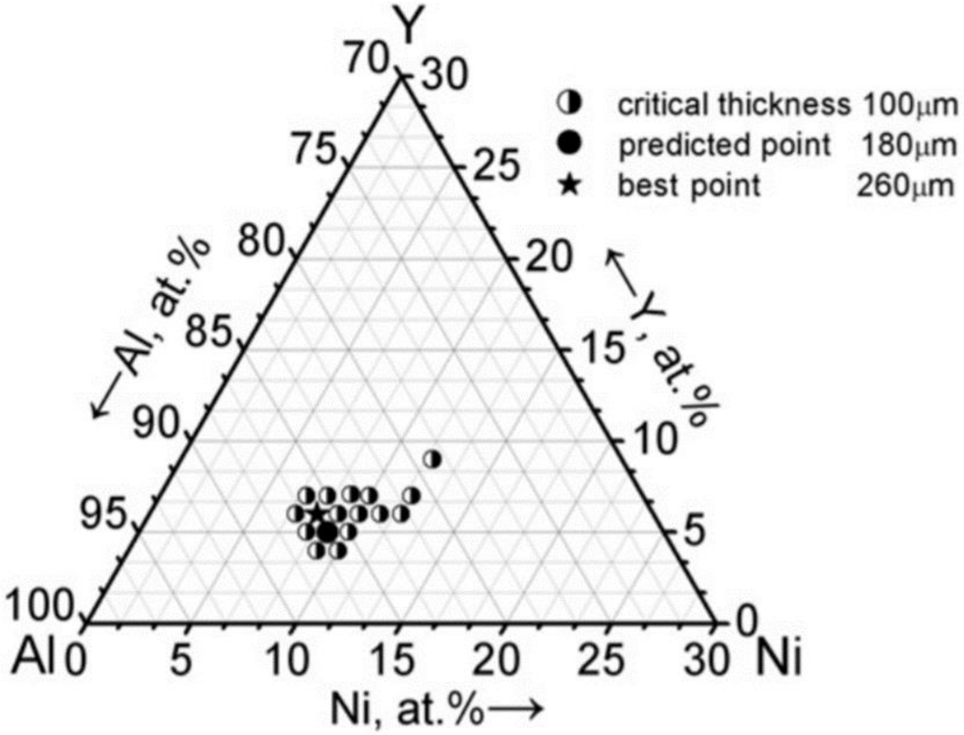

Figure 1.4. Ternany diagram for GFA (= critical ribbons thickness) in the Al–Ni–Y system. (Reprinted from ref [10])

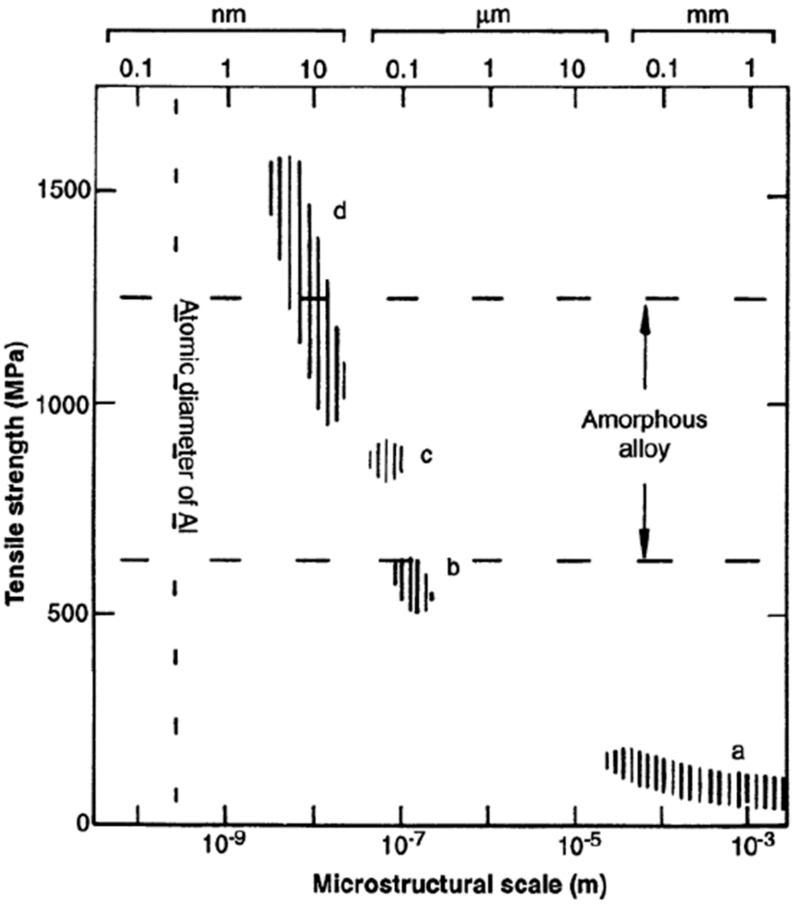

Figure 1.5. The tensile strengths of aluminum alloys compared as a function of micro-structural scale: (a) Pure aluminum with commercial purity, (b) the conventional precipitation-hardened Al alloys, (c) amorphous Al-TM-RE alloys, (d) partially crystallized amorphous Al-TM-RE alloys with FCC-Al nanocrystals. (Reprinted from ref [14] with permission though “Copyright Clearance Center”)

1.3. Devitrification behavior of metallic glass.

The crystallization behavior of metallic glasses has been focused for its importance in explaining the glass stability of the alloys and in the synthesis of the new nanostructured materials with advanced mechanical properties. Typically, the precipitation of nano-scaled crystalline phases into the amorphous matrix can be achieved through the two kinetic pathways. The one is the modification of devitrification modes, and the other is appropriate selection of cooling rate that allows for proper partial crystallization during rapid quenching. Both approaches require the profound understanding about the crystallization behavior of metallic glasses. The first route is more widely accepted because it offers the advantages on the alloy systems which are too sensitive to control the quench conditions. A more comprehensive knowledge of crystallization behavior will promote successful synthesis of bulk amorphous alloys by avoiding crystallization during solidification of glass forming liquid. On the other hand, gauging crystallization process in the amorphous phase can lead to successful manufacturing of novel metallic glasses with tailored nanostructures.

A hypothetical diagram of free energy for the Fe-rich Fe-B alloy system commonly used as an example to explain the thermodynamics of crystallization processes. [18]. In binary Fe-B alloy system, both α-Fe and Fe_2B are stable phases and Fe_3B is a metastable phase. The driving force for crystallization of glass is defined with the free energy difference between the glass (= liquid) and the appropriate crystalline phases. As shown in the schematic image in figure1.3, there are three crystallization reactions that amorphous alloys can follow: (1) polymorphic crystallization, (2) eutectic crystallization, (3) primary crystallization.

Polymorphic crystallization involves the crystallization of the amorphous alloy without compositional changes into a supersaturated solid solution, metastable phase or a stable crystalline phase. This type of transformation is named as polymorphous since this behavior is similar with the transformation occurs in the pure metals or intermetallic compounds. The occurrence of polymorphous crystallization is only possible in the limited compositional ranges where the glassy was formed at a composition corresponding to either a stable or metastable solid solution phase or intermetallic phase. The reaction 3 in figure 1.6 (transformation of glassy phase into the Fe_3B) is the one of the well-known example for the polymorphous reaction.

Eutectic crystallization is the type of transformation occurs with simultaneous crystallization of more than two phases. Subsequence decomposition can take place through the reaction 2 or 4 as show in figure. As consequence, mixture of α-Fe and Fe_3B or Fe_2B can be formed. the reaction front of the two components has to be separated into two phases and it usually take longer time than the polymorphous crystallization. The eutectic crystallization mode requires the largest driving force and can occur in the whole concentration ranges.

Primary crystallization is consisted with the nucleation and growth of one crystalline phase which possess the difference composition with the matrix. Like the reaction 1 in figure 1.6, solute atoms will be diffused out into the amorphous matrix until the equilibrium is reached. The primary crystalline phase could be either a terminal solid solution or an intermediate compound phase. The morphology of the primary crystal ranges from the spherical to highly dendritic and is highly dependent on solute compositions.

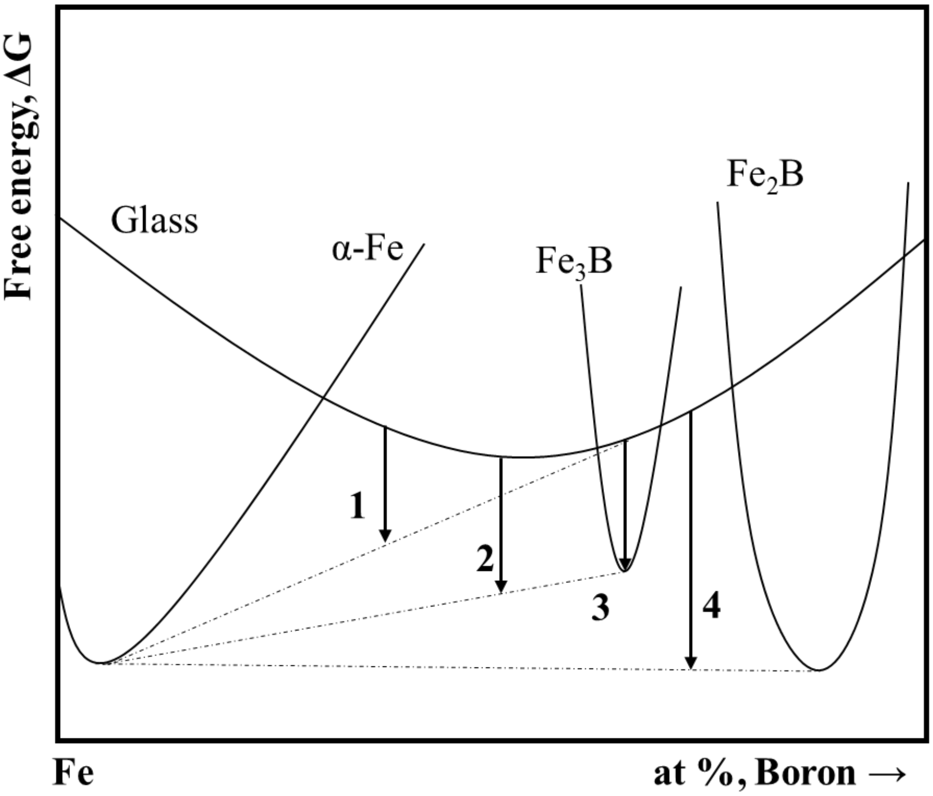

Figure 1.6. Schematic free energy vs. composition diagram for the Fe-rich Fe–B alloy system.

1.3.1. Thermodynamics of phase transition.

Al-TM-RE glass formers can be classified into three categories of alloys, (1) Glassy alloys (clear T_g and eutectic crystallization) (2) Nano-glassy alloys (clear T_g and primary crystallization) and (3) nanocrystalline alloys (unclear T_g and primary crystallization) which can be distinguished from each other by their different thermal properties and the crystallization reactions [19,20]. Among them, nanocrystalline type involved with the primary FCC-Al nanocrystals have been paid great attention. Understanding of the primary crystallization mechanisms not only attribute to the designing of the novel Al-based metallic glass with nanocrystals, but also helps us to understand the secret of glass formation and advanced fabrication processes [21,22]. To solve this question, several models are proposed, including “quenched-in nuclei” [23], “Coupled-flux model”[24] and “phase separation of amorphous matrix”[25,26].

Quenched-in cluster model : In liquid state, due to the fast diffusion rate, size of the Al clusters is small. But if these clusters grow over critical size after the fast cooling, Quenched-in clusters can provide the high density of heterogeneous nucleation sites for FCC-Al and subsequent growth results in the metastable amorphous alloy.

Coupled-flux model : When Al diffuse into the clusters, out-diffusion of solute atoms occurs together. Thus, growth of clusters is influenced by the diffusion rates of solute elements in the amorphous matrix. This means that number of quenched-in clusters connected with not only the Al cluster size, but also the concentration of solute elements around the clusters. From this diffusion kinetics, a new nucleation model names as coupled-flux model, which consider the long-ranged interfacial diffusion fluxes was proposed by K.Kelton [27]. The coupled-flux model has successfully explained the formation of the nanocrystal in $Al_{88}Y_7Fe_5$ without phase separation during the relatively low temperature heating process.

Phase separation model : Phase separation is also one of the commonly considered phenomenon in the Al-based MGs. Based on the splitted X-ray diffraction patterns and electron SAED pattern that can be observed in Al-based MGs, nanoscale phase separation model was proposed. Prior to crystallization, fast diffusion of Al makes the Al-rich phase separated zone, where catalyze the nucleation of FCC-Al.

1.3.2. Nucleation kinetics of primary FCC-Al

Regardless of the various models described above, primary crystallization of FCC-Al must consider the transient nucleation. During the isothermal annealing of metallic glasses below T_x or solidification of liquid, the materials undergo a transient stage of nucleation followed by steady state nucleation stage, where the rate of nucleation is constant. Nucleation of new phases is the process that involves the clustering of atoms as embryos which develop into nuclei when the size of embryos reaches over the critical size. The delayed time for the nucleation of new phase can be defined as incubation time, τ. From the aspect of growth of embryos into the nuclei with critical size, the incubation time can be defined as the time of diffusion motion of atoms in an random walk zone, (Δ, bounded by $\Delta G^* - kT$) in the vicinity of the critical cluster size, r^*. This means that only in the vicinity of the critical size n, embryo can evolve into the nucleation. Considering this, the incubation time can be expressed as $\tau = \tau_c + \tau_\Delta$ [28]. Where τ_c is the time related with the nucleation under the influence of an thermodynamic free energy difference, and τ_Δ describes the time that requires the random walk from a cluster size of $n^* - 0.5\Delta$ to $n^* + 0.5\Delta$. The value of Δ represents the cluster size distribution for which random walk is the rate limiting step for growth.

The incubation time is the parameter that can directly provide the attachment frequency, β and random walk zone at the given temperature as defined in equation 1-1 ;

$$\tau = \frac{1}{2Z^2\beta} \quad . \qquad \text{Eq. 1-1}$$

In here, Z is the Zeldovich factor. Z gives the probability that a nucleus in the vicinity of critical size will evolve into the new phase, and it can define the width of random walk zone, $(\Delta = 1/(Z\sqrt{\pi}))$. Classical nucleation theory can predict the nucleation rate as described below;

$$I = Z\beta N_s exp(-\Delta G^*/kT) \quad . \qquad \text{Eq. 1-2}$$

Where, $\Delta G^*$is the activation energy for nucleation N_s is the number of nucleation sites. This equation is the multiplication of the thermodynamic factor and kinetic factor In equation, $N_s exp(-\Delta G^*/kT)$, which is the thermodynamic part represents the instantaneous number of nuclei at the top of the nucleation barrier. So, large ΔG^* value decreases the probability of nuclei forming. $Z\beta$ is the kinetic part explaining the effectivity of the atomic diffusion along the radial axis. Therefore, proper observation of the incubation time is important to understand the nucleation behavior and glass formation of the Al-based glass forming systems. In the case of bulk glass forming alloys under nucleation control, the crystallization signal can be shown by isothermal DSC analysis, making it feasible to measure the nucleation incubation time directly [29]. However, for the marginal Al-based metallic glasses under growth control, growth of quenched-in cluster or nanocrystals hinder the proper prediction of the incubation time. Hence TEM analysis by plotting the number density of FCC-Al and annealing time applied to establish the nucleation rate and incubation time [30]. However, this direct method takes long time and is not a preferable method.

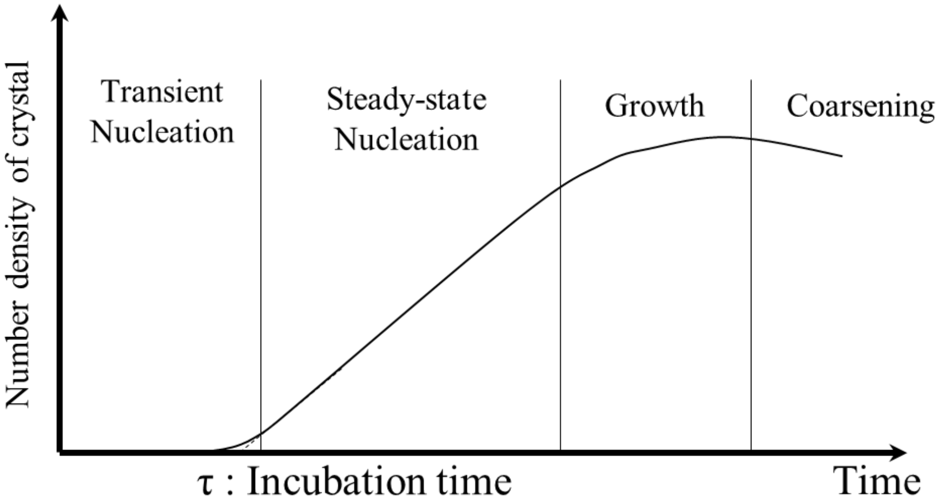

Figure 1.7. Schematic plot for relation between the number density and time showing crystallization stages: transient nucleation, steady-state nucleation and growth/coarsening.

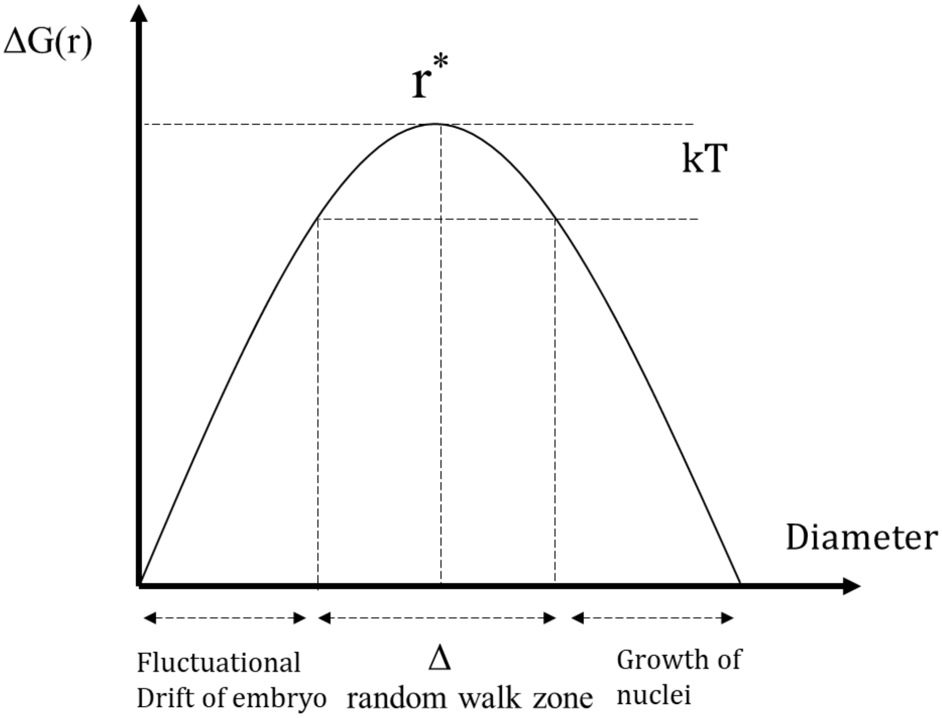

Figure 1.8. Schematic plot for critical nucleation size and random walk zone

1.3.3. Growth kinetics of primary FCC-Al

Figure 1.9 is the one of the good examples that shows the growth behavior of FCC-Al [31]. Figure 1.9 (a) is the TEM analysis obtained from the $Al_{88}Y_7Fe_5$ metallic glass sample which are annealed at 245 °C for 10 min. and figure 1.9 (b) is the histogram of FCC-Al nanocrystals in TEM images. The value of crystallization enthalpy for nucleation and growth is same for every FCC-Al. Thus, as described by K.F. Kelton, the earlier the FCC-Al nucleated, the bigger the FCC-Al size. The lower the number density of the larger crystals, then, largely reflects a time-dependent nucleation rate; at first, the production rate is slow and increased to the steady-state rate with the annealing time. For the longer annealing times (small crystal sizes), due to the overlapping of the diffusion fields of the grown crystalline phases (or grains), the nucleation rate decreases [32]. This type of precipitation behavior can have the bell-shaped size distribution when the transient nucleation occurs at the limited number of nucleation site in combination with interface-controlled growth. Consequently, saturation of growth of FCC-Al yields the bell-shaped size distribution as shown in figure 1.9 (b).

In the case of polymorphic crystallization, which is involved with no compositional fluctuation, the growth rate shows simple linear relation with the time and temperature. However, the growth rate for the primary FCC-Al crystallization should consider the morphology and composition changes. To satisfy this condition, parabolic growth mode adapted for growth of primary crystalline phase [33]. The diffusion coefficient, D is the function of the temperature and is expressed as equation 1-3

$$D = D_0 \exp\left[-\frac{Q_s}{kT}\right] \quad . \qquad \text{Eq. 1-3}$$

In here, D_0 is the pre-factor and Q_s is the diffusion activation energy. The radius of crystalline phase is given as the function of time;

$$r(t) = \alpha\sqrt{Dt} \quad . \qquad \text{Eq. 1-4}$$

By inserting equation 1-3 into equation 1-4 yield the growth rate as below;

$$U = \frac{dr(t)}{dt} = \frac{\alpha D}{2\sqrt{Dt}} \quad . \qquad \text{Eq. 1-5}$$

Where α is a dimensionless parameter involving the composition of the crystal and matrix away from the crystals. Köster has used the parabolic growth rate equation for the primary crystalline phases of various system [33]. At the beginning of the crystallization of FCC-Al, the volume of nucleated phase is small and growth is under interface control Thus, the parabolic growth rate model can be accepted to express the growth rate in the early stage when the crystals remain spherical shape. After the certain time, the growth mode translates into diffusion control due to longer diffusion path between FCC-Al and the amorphous matrix. Finally, because the depleted Al around the interface of FCC-Al, saturation of the number density of FCC-Al occurs. The impingement of the diffusion field around the FCC-Al cannot supply the Al atoms into the FCC-Al. Once a metastable equilibrium is reached between the FCC-Al and amorphous matrix, the overall free energy decreases by coarsening through growth of the largest crystals at the expense of the smallest [34].

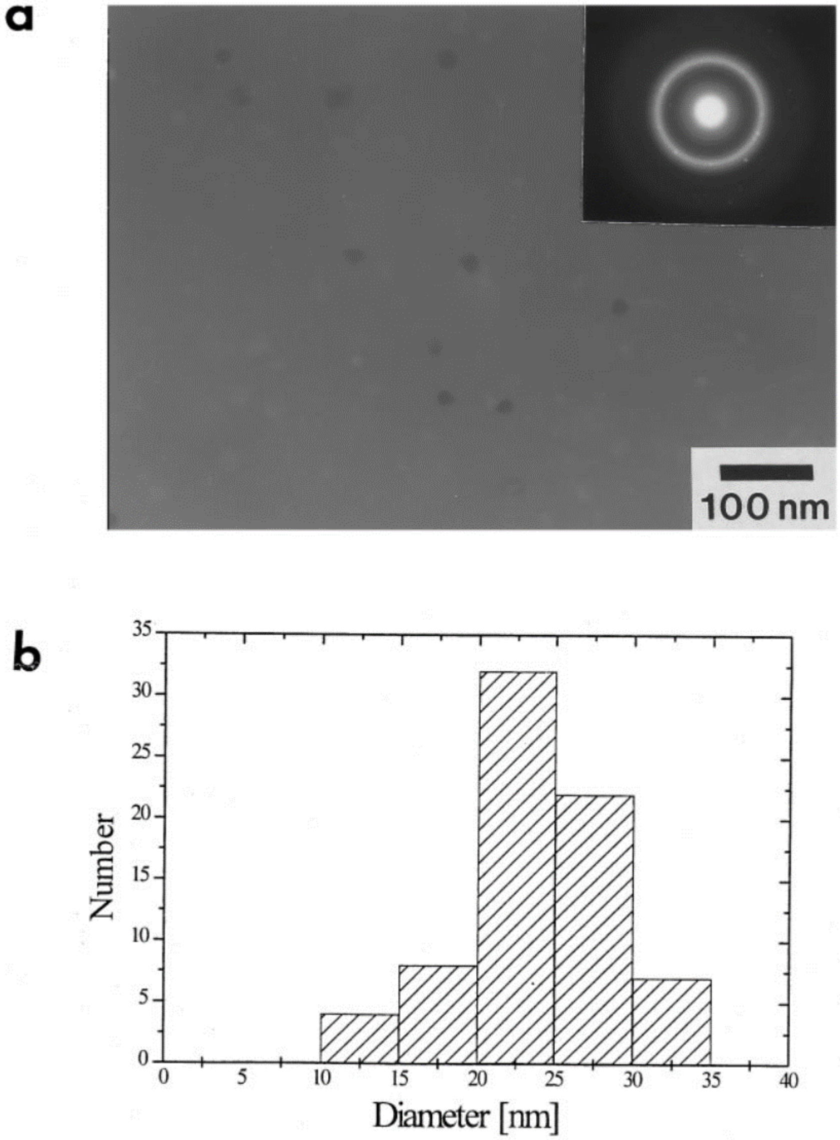

Figure 1.9. (a) bright-field TEM image for Al87Y7Fe5 metallic glass annealed at 245 °C for 10min. inserted image is the SAED patten of the annealed sample. (b) histogram of FCC-Al nanocrystal diameter. (Calculated volume fraction of FCC-Al is $1.4 \cdot 10^{22}$ m^{-3}) ((Reprinted from ref [31] with permission though “Copyright Clearance Center”)

1.4. Thesis motivation and scopes.

Through the competitive phase selections of undercooled liquid, it is possible to product the Al-based MGs with high number density of nano-scaled FCC-Al. Proper precipitation of these crystalline phases can be achieved by the deep understanding about the crystallization kinetics of FCC-Al. And primary FCC-Al nanocrystals advance the mechanical properties of the Al-based MGs. Thus, studies on devitrification kinetics of Al-based glassy alloys is important in both of engineering and scientific point of view.

The fundamental aspects of the nucleation kinetics have been discovered to some extent, but many issues discussed only in schematic manners. And there are no direct reports showing the enhanced room temperature plasticity of Al-based MG composites. The primary goal of this research is (1) to conduct the comprehensive investigation on the crystallization behavior of primary FCC-Al. and (2) to develop the Al-based metallic glass composite which can beat the strength-ductility trade-off.

Among the various topics regarding this research issue, three major research topics have been concentrated deeply.

1. Numerous studies have been conducted to discover the new design method for multicomponent Al-Ni-RE metallic glass with good liquid stability. Controlling of T_g, T_x is one of the key factors for manipulating the phase stability of glassy alloys. In addition, phase selection kinetics which is related with the primary or eutectic crystallization is also important physical issue for glass forming ability. In here, intensive research was performed to find out the parameter which can link the phase stability with the chemical

bonding nature of Al-RE.

2. Because of limited GFA and high number density of pre-existing nuclei ($>10^{21}m^{-3}$), quantitative investigation on transient effect such as incubation time, nucleation rate of FCC-Al has been restricted. If it is possible to obtain the exact nucleation rate of FCC-Al depending on the temperature, more sensitive controlling of microstructure in Al-base MG composite would be feasible. To overcoming these spatial features that constrain the proper investigation of nucleation behavior, based on the classical nucleation theory, fast heating calorimetry study was intensively performed.

3. It has been considered that introduction of soft FCC-Al nanocrystal can increase the strength and room temperature plasticity. However, due to the structural complexity of the composite matrix, detailed interpretation on deformation behavior have merely been reported except the simple bending and microhardness test. Thus, to understand the deformation behavior of Al-based MGs, which can be modified by the compositions and volume fraction of FCC-Al, nano and micro scaled mechanical responses were conducted by various mechanical test.

Chapter 2.

Experimental procedures

2.1. Sample preparation

2.1.1. Arc melting

Preparation of the master alloy with the desired composition was conducted by arc melting of high-purity elements. The mixtures of high-purity elements (99.9 % in purity) were placed on a water-cooled copper hearth inside of the vacuum chamber of arc-melter (SAMHAN vacuum development Cooperation; figure 2.1(a)). The chamber was evacuated into a high vacuum state under $2.0\cdot10^{-5}$ torr followed by backfilling of Ti-gettered argon with total pressure of 5N. The mixtures of elements were melted with arc plasma generated from the tungsten electrode. And re-melted more than four times to ensure homogeneously alloyed master alloys.

2.1.2. Melt spinning

The arc-melted master alloys were crushed into proper size for putting inside a quartz tube. To control the amount of injected liquid, nozzle hole was drilled on the quartz tube in 0.5 and 1.0 mm diameter, respectively. And quartz tube with rectangular shape (7 X 0.5 mm) of nozzle also used for wide ribbons. The quartz tube containing piece of alloy was installed in the melt-spinner (SAMHAN Vacuum development Cooperation; figure 2.1 (b)) and the chamber was evacuated and backfilled by pure argon gas with a pressure of 5 N. Then, the piece of alloy was re-melted by induction heating and the melt was injected on a rotating copper wheel. To adjust the cooling rate, rotating speed of copper wheel was modulated from 10 m/s to 40 m/s. Quartz tubes with various nozzle size were alternatively used. Depending on the melt spinning condition, ribbon samples with various thickness (from 18 to 45 μm) was obtained as shown in figure 2.1(c). In this study, except the chapter 4.4.3 and chapter 6, ribbons with the 18 μm thickness were used.

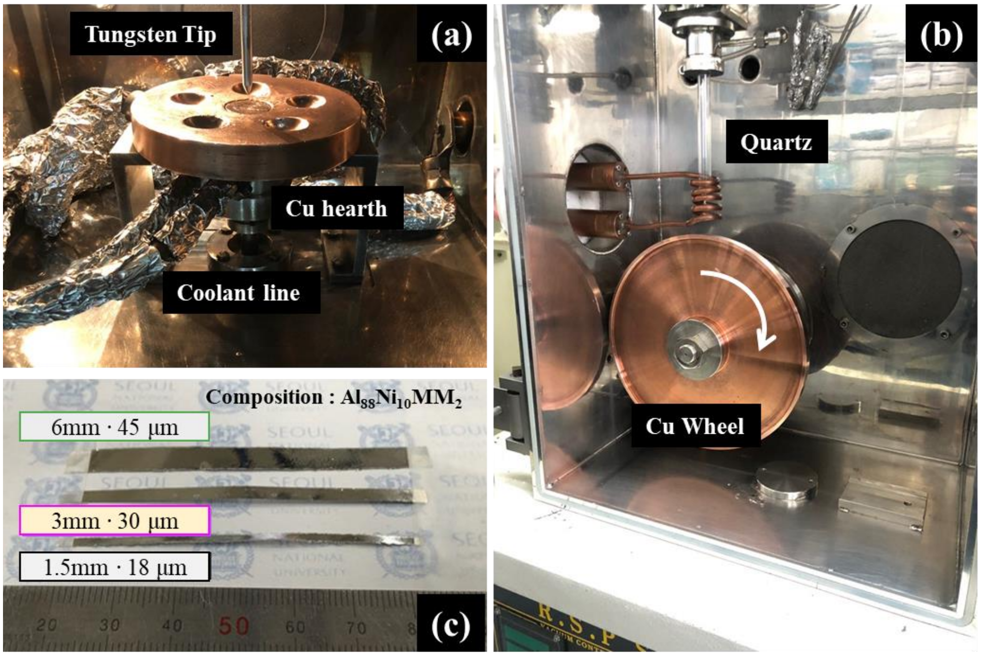

Figure 2.1. (a) picture of inside of chamber of arc-melter, (b) melt-spinner and (c) $Al_{88}Ni_{10}MM_2$ ribbon samples with various size.

2.1.3. Specimen preparation for TEM and APT

Thin foils of $Al_{90-X}Ni_{10}MM_x$ amorphous alloys for TEM (Transmission electron microscopy) analysis were prepared by using a PIPS (Gatan; PIPS II). $Al_{88}Ni_{10}MM_2$ is the amorphous alloy with exceptional low crystallization temperature. To avoid the crystallization in $Al_{88}Ni_{10}MM_2$ via high energy ion beam, liquid N_2 cooling stage was applied to keep the sample temperature below -443 K (-170 °C). At first, double-sided milling at 2.5 keV was conducted and final milling was done at 1.0 keV. Due to the low T_x, conventional Ga+ ion beam can generate the crystallization in $Al_{88}Ni_{10}MM_2$ metallic glass. To prepare nano tip of $Al_{88}Ni_{10}MM_2$ amorphous alloys for APT (Atom probe tomography), Xenon-plasma FIB microscope (Helios G4 PFIB, Thermo fisher) with a cryogenic-stage reaching -408 K (-135 °C) was used. Specimen was lifted out from the bulk sample and mounted on the Si-post (CAMECA Instruments).

2.2. Structural analysis

2.2.1. X-ray diffraction (XRD)

X-ray diffraction measurement of as-spun and annealed Al-TM-RE samples were performed with a Bruker D8 Discovery X-ray diffractometer using monochromatic Cu Kα radiation. The 2θ range is 20 – 80° with a scanning rate of 0.5 degree per second. The ribbon samples were placed on the plate glasses to prepare flat surface for the diffraction.

2.2.2. Small angle X-ray scattering (SAXS)

To investigate the size change of nano-meter sized FCC-Al precipitated in $Al_{88}Ni_{10}MM_2$ depending on the annealing temperature, in-situ small angle X-ray scattering (BL4C beamline, Pohang Accelerate Laboratory II, Pohang, South Korea) was conducted [35] (figure 2.3 (a)). Accelerated X-ray are monochromated with a Si (111) double crystal monochromater (DCM) placed 18.0 m from the X-ray source. Energy of incident beam was 18.0 keV, and wavelength was 0.07 nm. The sample to detector (2D SX165, Rayonix) distance was 5.0 m. Customed in-situ heating stage (figure 2.3 (b)) was installed on the sample stage. The maximum temperature and of the heating stage was 400 ℃, controllable heating rate range is 0.5 to 20 K/min.

2.2.3. Transmission electron microscopy (TEM)

For the observation of microstructure and the corresponding diffraction patterns of as-spun and annealed metallic glasses, transmission electron microscope operated at 200 kV (Tecnai F20, Termo-Fisher Scientific).

2.2.4. Atom probe tomography (APT)

For APT analysis, LEAP 5000 XR (CAMECA Instrument, US) was utilized. The measurement was conducted at a base temperature of 60K under voltage pulsing mode. The value of pulse fraction (V_p/V_{dc}) and pulse rate were 20% and 50Hz, respectively. The 3D tomogram was obtained by IVAS software (CAMECA Instrument) following a general protocol to range the mass spectrum.

2.3. Thermal analysis

2.3.1. Differential scanning calorimetry (DSC)

A Perkin-Elmer DSC 8500 was used for thermal analysis with the heating rate of 20 K/min or 40 K/min. The samples were sealed in an aluminum pan, which can be heated up to 873 °C. The sample weight was 5 mg and the obtained DSC signals were normalized from the sample weight. The Heat flow and temperature were calibrated using the standard indium and zinc samples. To get the flat DSC traces showing clear T_g and T_x, the thermal signal obtained from the first heating cycle was subtracted by the flat thermal signal obtained from the second heating cycle.

2.3.2. Fast heating calorimetry (FDSC)

Fast scanning chip calorimeter, which is known as FDSC (Flash DSC 2+, Mettler Toledo, figure 2.2 (a)) was used to perform isothermal and continuous thermal scanning at fast heating rates. As shown in figure 2.2(b), metallic glass ribbon samples were cut into the small pieces (smaller than 0.1 X 0.1 mm^2), and loaded on the MultiSTAR UFS 1 MEMS chip sensors. To attach the samples with rough surfaces with the thermal sensor, a little drop of distilled water was applied to the sensor with the sample. Distilled water can glue the sample onto the thermal sensor and does not damage thermal sensor or sample.

2.3.3. Thermo-mechanical analysis (TMA)

In order to detect the softening point and the drastic viscosity change (=super cooled liquid region), the temperature versus strain rate relation of metallic glass ribbon samples under the constant loading condition was conducted by TMA (TMA Q400, TA instruments). The heating rate of temperature scanning was 10 K/min. 0.1N of constant compression stress was applied on the stacked ribbon samples (Total thickness ~ 500 μm) by 1 mm diameter quartz tip.

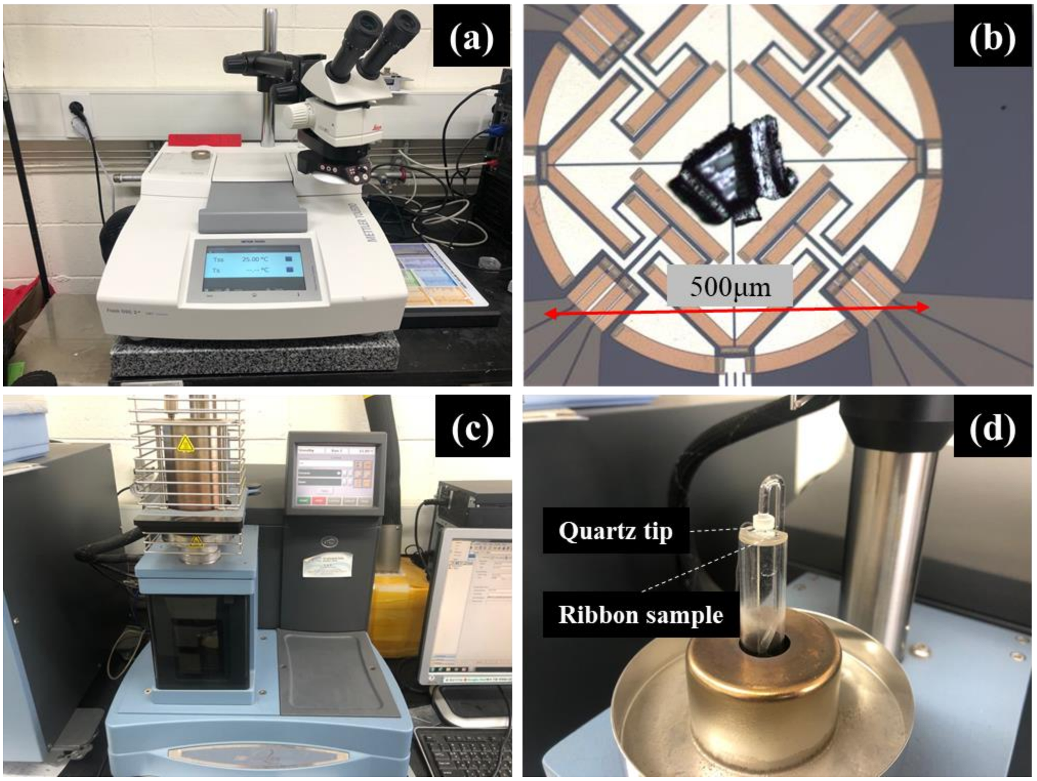

Figure 2.2. (a) Flash-DSC 2+ used in this research and (b) optical microscopy image of the UHS sensor with the metallic glass sample. (c) TMA and (d) TMA compression mode for temperature vs dimension change.

2.4. Mechanical analysis

2.4.1. Nanoindentation

Nanoindentation analysis (TriboLab 750, Bruker) was conducted to measure the hardness, elastic modulus and the pop-in size of the metallic glass ribbons. The mirror like polished cross-section of the ribbons were indented by Sphero-conical diamond tip (Radius = 1 μm) in load-controlled mode at the constant loading rate of 0.1 mN/s. 200 times of indentation test were repeated to collect the enough number of pop-ins for statistical analysis of pop-ins which will be described in chapter 6.

2.4.2. Ribbon bending test.

Macro-scaled deformation behavior of metallic glass was investigated by bending test. To control the bending speed and distance, costumed bending tester (Bending/fatigue tester, CK Trade figure 2.3(a)) was used. Ribbon sample placed in between two plates in which one plate is fixed on light side while other is moving toward the fixed plate. The moving plate can be moved at constant speed and it can be stopped at the certain distance from the fixed plate. the moving spped and the final distance between two plates can be controlled by software. After the bending, bended sample removed from the two plate. Kink angle and the shear displacement of the bended ribbons were examined by optical microscopy. To observe the clear shear displacement image, dark-field mode was applied.

2.4.3. Tensile test.

Tensile test of ribbon samples was performed (QUASAR 5, Galdibini, figure 2.3(b)) at room temperature at the strain rate of $4 \cdot 10^{-4}$ s^{-1}. At least 3 samples for each material were tested to confirm the reproductibility. Ribbon samples were polished in similar dimension, and plastic guide-plate were glued to help the tensile test. For the cyclic tensile test, maximum stress for each tensile test was applied from 600 MPa until the sample failure with a increment of 50 MPa.

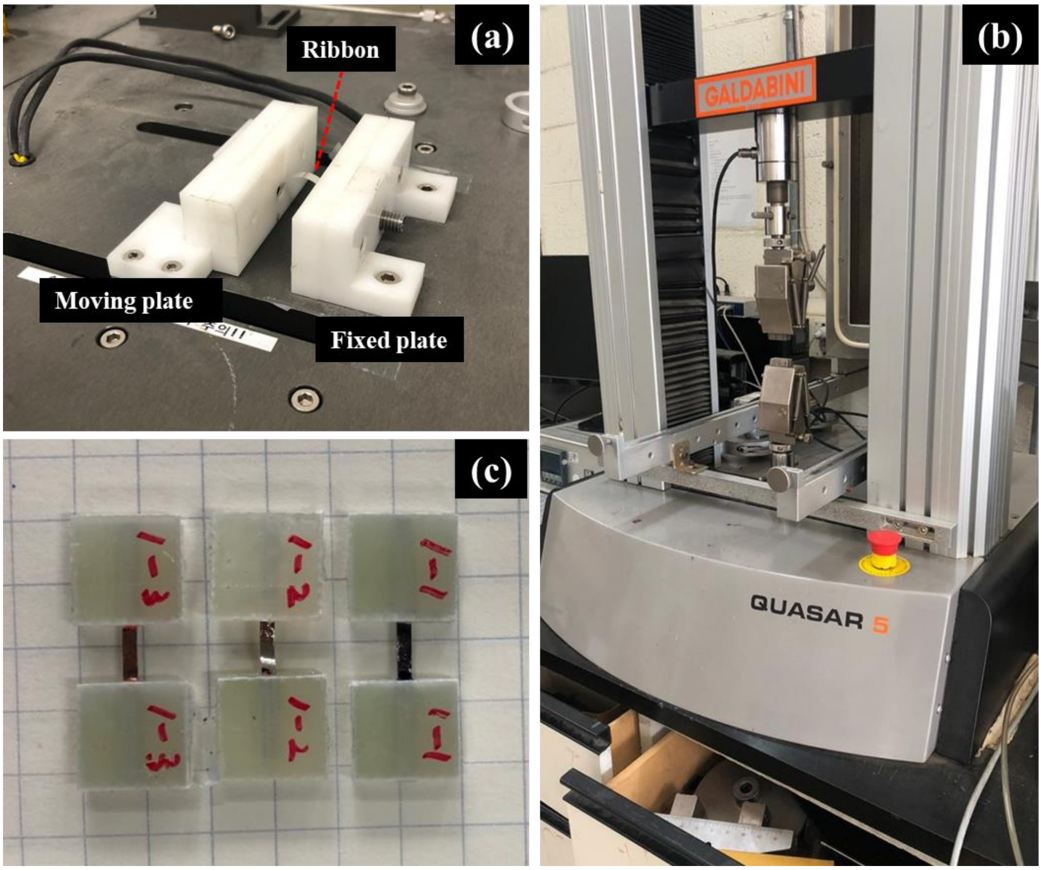

Figure 2.3. (a) bending tester for thin plate type of sample including metallic glass ribbon, (b) QUASAR 5 tensile tester for precise tensile test of ribbon sample and (c) picture of the ribbon samples used in this research.

Chapter 3.

Phase stability of $Al_{84}Ni_{10}RE_6$ MGs

* Detailed results of this chapter are published in W.Kim, H.S. Oh, E.S. Park, *Intermetallics,* **91,** 8 (2017)

3.1. Introduction

Traditionally, Inoue's three empirical rules have been considered as an invariable guideline for developing metallic glasses: (1) Consisting of more than two elements, (2) Atomic size mismatch which is greater than 12%, (3) A large negative heat of mixing between the elements [37]. Multicomponent systems will lead to relatively stable and slow kinetics, because of significant redistribution of constituent atoms and large driving forces for crystallization [38]. More specifically, certain atomic size ratios, along with the negative mixing enthalpy between the constituent elements are required for efficient packing of constituent atoms and subsequent formation of icosahedral short-range ordering, that may provide metastability of the undercooled melts [39]. Atomic packing efficiency is of importance to manipulate the stable glasses. The content (or the atomic ratio) of Al in Al-based MGs is exceptionally high, being more than 80 at%. Also, the atomic radius difference between Al and the RE elements are large enough. This yields the RE-centered icosahedral cluster with the 16 – 18 of average coordination number [38]. It is typically considered that the higher the atomic packing efficiency of solute centered clusters is the better the glass forming ability is for the alloys. Consequently, it is expected that the addition of more RE elements results in higher GFA of Al-TM-RE system.

In this chapter, to focus on the relation of Al-RE atomic nature with the phase stability of Al-TM-RE metallic glass system, multiple addition effect of RE elements was systematically observed. From 1 to 5 number of RE elements, chosen from La, Ce, Nd, Gd, Y, and Er was added in the order of electronegativity. Results of this research propose effective design parameters for (1) thermal properties, (2) crystallization behavior and (3) mechanical property.

3.2. Optimization of thermal properties by addition of multiple RE elements

3.2.1. Multiple RE addition effects on thermal properties

Figure 3.1 shows DSC traces of $Al_{84}Ni_{10}RE_6$ MGs with a different single RE and multiple equatomic REs chosen from La, Ce, Nd, Gd, Y, and Er in the order of average value of electronegativity (ψ). The black and red arrows point the T_g and T_x of each MGs, and normalized values of crystallization enthalpy are marked together. First peaks whose enthalpy value is small than 40 J/g are related with the primary crystallization of FCC-Al. As summarized in figure 3.2, it is experimentally confirmed that T_g and T_x of the MGs are largely increased when the average ψ values of RE decreased. Based on the Darken-Gurry theory, the intensity of the interaction ($W_{A\text{-}B}$), which reflects the bonding nature between two atoms associated with compound-forming tendency, can be defined as equation 3-1 [40,41]

$$W_{A-B} = (\frac{\Delta\epsilon_{AB}}{0.15})^2 + (\frac{\Delta\psi_{AB}}{0.4})^2 \quad . \qquad \text{Eq. 3-1}$$

For instance, $Al_{84}Ni_{10}La_6$ with the highest T_g and T_x among MGs in this research exhibits relatively shorter atomic bonding length between Al and La than $Al_{84}Ni_{10}Er_6$ because $W_{Al\text{-}La}$ value (10.167) is higher than $W_{Al\text{-}Er}$ value (5.127). Interestingly, it was reported that the decrease of $W_{Al\text{-}RE}$ in Al-TM-RE MGs with a different REs results in higher liquid stability during cooling due to the enhanced topological homogeneity (lower T_g), but promotes the cluster formation of FCC-Al during heating (lower T_x) [42]. Likewise, addition of multiple REs leads to a relatively smaller decrease in T_x

than in T_g due to confusion of crystallization by compositional complexity [14]. To further strengthen the understanding about thermal properties, variations of T_g and T_x depending on W_{Al-RE} were summarized as shown in figure 3.3. For a different single RE and multiple REs, the T_g change depending on the W_{Al-RE} exhibits the similar slop (single RE : 5.37 K/W_{Al-RE} Multiple REs : 5.77 K/W_{Al-RE}). But, the slop for the T_x variation shows profound difference (single RE : 5.26 K/W_{Al-RE} Multiple REs : 6.28 K/$_{Al-RE}$). This means that addition of multiple RE can effectively prohibit the crystallization

Interestingly, the T_x change in $Al_{84}Ni_{10}RE_6$ shows clear inflection at the point (W_{Al-RE}) =7.59) where the crystallization behavior divides into primary and eutectic crystallization. Below the 7.59 W_{Al-RE}, $Al_{84}Ni_{10}RE_6$ system crystalize through the primary crystallization behavior. FCC-Al in Al-TM-RE glassy system is the stable phase which can be precipitated at lower temperature than $Al_{11}RE_3$ or $AlRE_3$ compounds. Thus, as shown in figure 3.4, the abnormal changes of Tx (1) induced by multicomponent effect and (2) precipitation of FCC-Al results in a triangle shaped super cooled liquid region (ΔT_x) change. Among the various multicomponent MGs, $Al_{84}Ni_{10}(NdGdY)_6$ has the widest ΔT_x of 27K. To extend the knowledge about ΔT_x, $Al_{84}Ni_{10}(NdGdY)_6$ was examined with the extremely high speed of heating (up to 10000 K/s) by FDSC. Figure 3.6(a) shows the FDSC traces depending on the heating rate, and figure 3.5(b) shows the results of T_g, T_x and T_p change as a function of heating rate. Interestingly, with the heating rate, ΔT_x of $Al_{84}Ni_{10}(NdGdY)_6$ increased up to 1000 K due to the abnormal increase of T_x with the heating rate. In conventional manufacturing processes, such as fast annealing, electric joule heating, fast processing along with fast heating rate is required. Thus, FDSC results of

$Al_{84}Ni_{10}(NdGdY)_6$ claim that marginal Al-based MGs with relatively narrow ΔT_x have the possibilities for for thermo-plastic forming due to their increased super-cooled liquid region at fast heating rate.

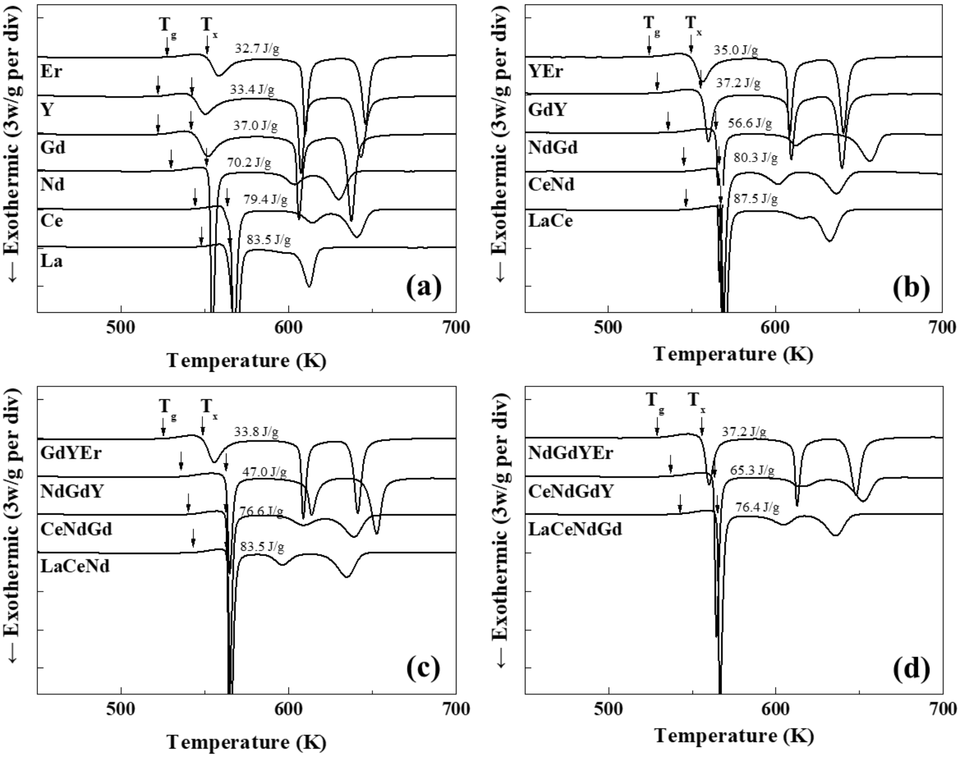

Figure 3.1. DSC traces of $Al_{84}Ni_{10}RE_6$ with (a) single RE, (b) binary REs, (c) ternary REs and (d) quaternary REs, which are added in the order of their electronegativity values. (heating rate = 40 K/min)

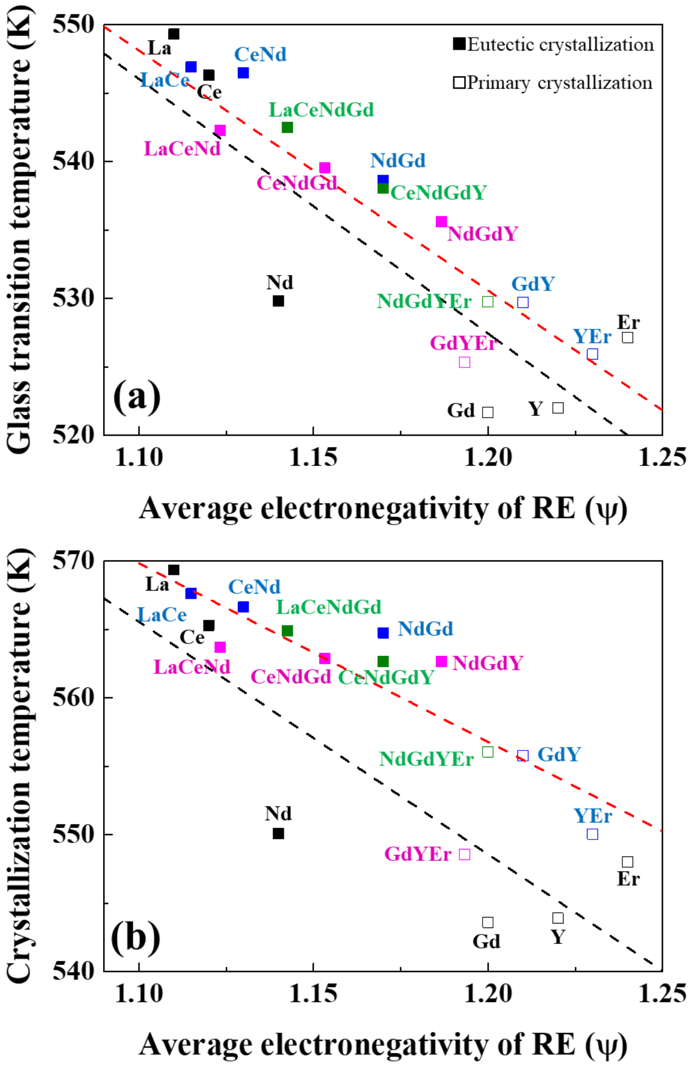

Figure 3.2. (a) T_g and (b) T_x change of $Al_{84}Ni_{10}RE_6$ as a function of average electronegativity (ψ) of REs. Solid and halo point means that the first crystallization mode of $Al_{84}Ni_{10}RE_6$ is eutectic crystallization and primary crystallization, respectively. Back dashed lines are the linear fitting results of $Al_{84}Ni_{10}RE_6$ with single RE and red dashed lines are linear fitting results of $Al_{84}Ni_{10}RE_6$ with multiple REs.

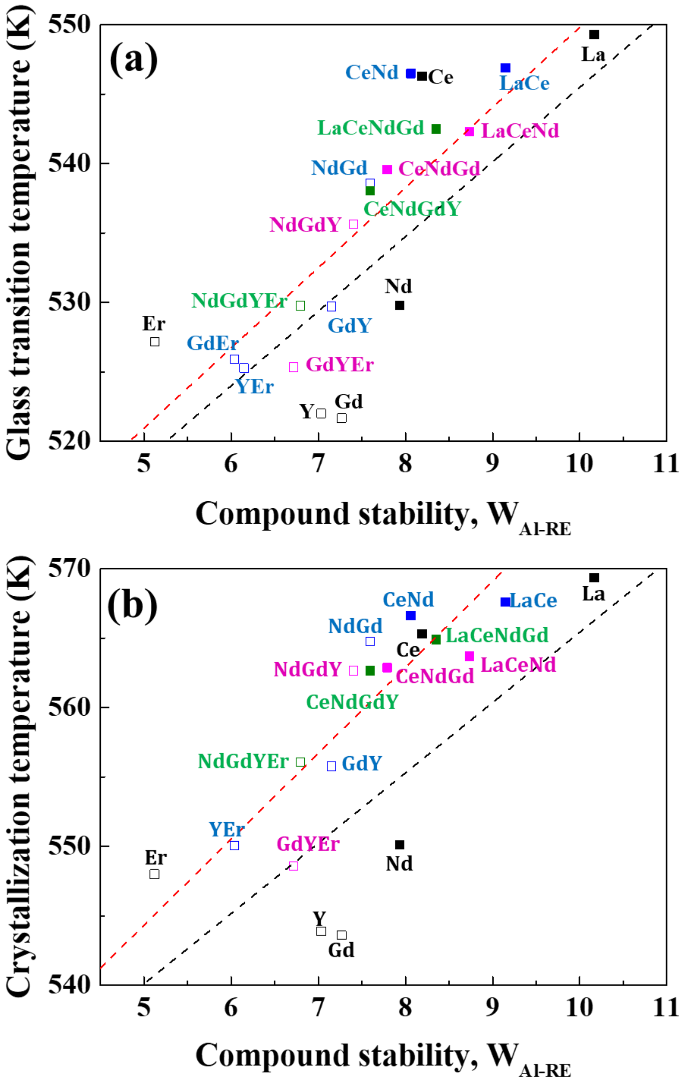

Figure 3.3. (a) T_g and (b) T_x change of $Al_{84}Ni_{10}RE_6$ as a function of compound stability ($W_{Al\text{-}RE}$) and average electronegativity value of REs. Solid and halo point means that the first crystallization mode of $Al_{84}Ni_{10}RE_6$ is eutectic crystallization and primary crystallization, respectively. Back solid lines are the linear fitting results of $Al_{84}Ni_{10}RE_6$ with single RE and red solid lines are linear fitting results of $Al_{84}Ni_{10}RE_6$ with multiple REs.

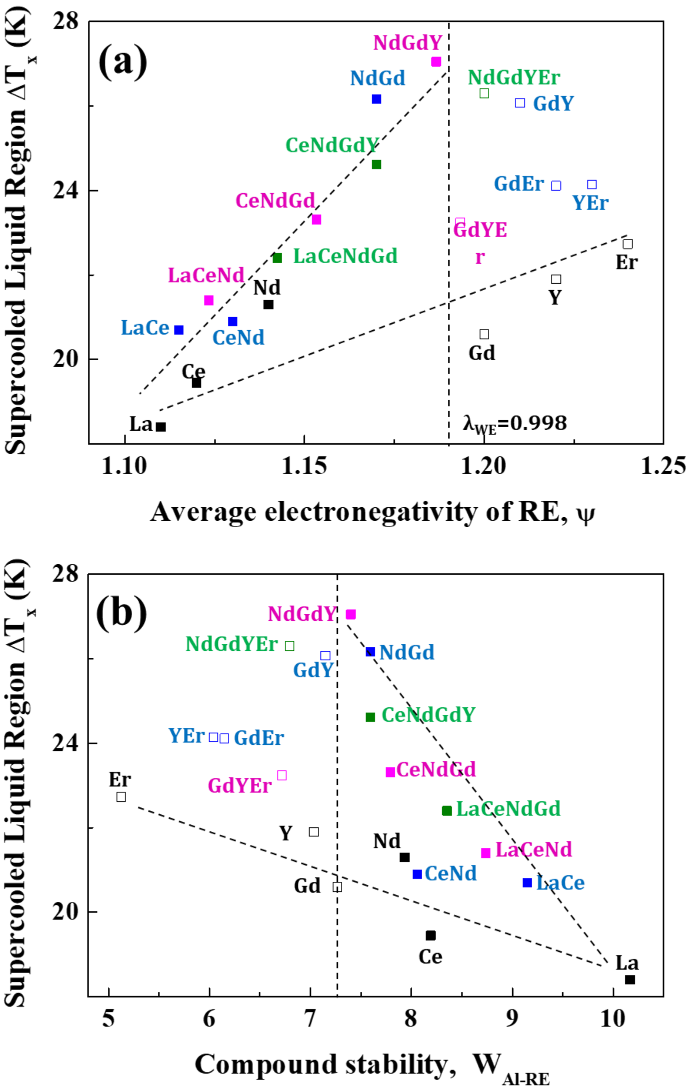

Figure 3.4. Width of super-cooled liquid region as a function of (a) average electronegativity value and (b) compound stability ($W_{Al\text{-}RE}$) of REs in $Al_{84}Ni_{10}RE_6$. Solid and halo point means that the first crystallization mode of $Al_{84}Ni_{10}RE_6$ is eutectic crystallization and primary crystallization, respectively.

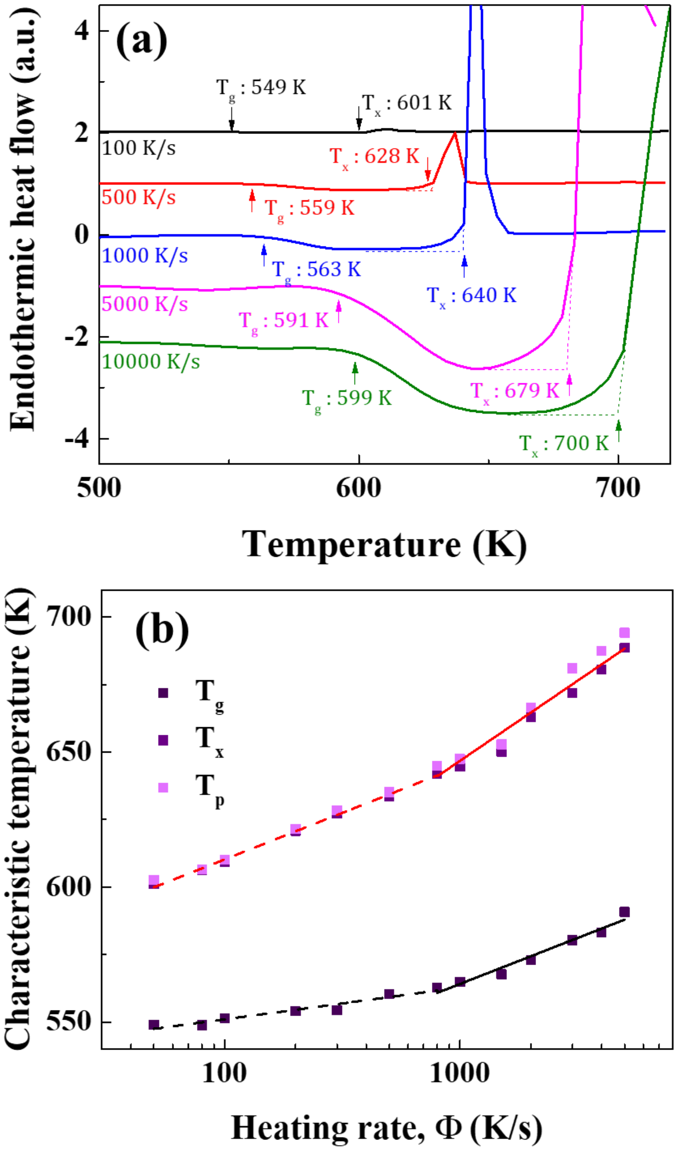

Figure 3.5. (a) FDSC results of $Al_{84}Ni_{10}(LaCeNd)_6$ and (b) summary of T_g, T_x, and T_p as a function of heating rate.

3.2.2. Dynamic and kinetic fragility

The packing efficiency of amorphous structure in MGs can be quantitatively evaluated via the fragility index, m. The stronger the liquid becomes (lower m), the higher the amorphous stability is, which is related to denser packing structure as well as higher GFA. It is considered that the chemical properties between aluminum and lanthanides elements are similar [43]. Thus, bonding nature effect is ignorable. To understand the structural variation induced by the addition of multiple REs in $Al_{84}Ni_{10}RE_6$ MG, dynamic fragility measured by two different dynamic variables, 1) relaxation time and 2) viscosity was carefully investigate with $Al_{84}Ni_{10}La_6$, $Al_{84}Ni_{10}(LaCeNd)_6$ and $Al_{84}Ni_{10}(LaCeNdGdY)_6$.

T_g variation for $Al_{84}Ni_{10}La_6$, $Al_{84}Ni_{10}(LaCeNd)_6$ and $Al_{84}Ni_{10}(LaCeNdGdY)_6$ as a function of $\ln(\phi)$ (ϕ : heating rate K/min) is summarized in Figure 3.6. Relationship of T_g and $\ln(\phi)$ can be fitted via Vogel-Fulcher-Tammann (VFT) type of function defined as below:

$$ln\phi = \ln A + D_f \cdot \frac{T_g^0}{T_g^0 - T_g} \quad . \qquad \text{Eq. 3-2}$$

D_f and T_g^0 are obtainable parameters from the fitting of the equation 3-2 [44]. The dynamic fragility by the rate of change in relaxation time at a given T_g, m_{dyn}^r can be calculated using the equation 3-3:

$$m_{dyn}^r = \frac{[D_f \cdot T_g^0 \cdot T_g]}{[ln10(T_g - T_g^0)^2]} \quad . \qquad \text{Eq. 3-3}$$

The value of $\ln A$, D_f and T_g^0 are summarized in figure 3.6 by the best fit to the experimental data and m_{dyn}^r values are evaluated at ϕ of 20 K/min by using equation 3-3. The m_{dyn}^r value of $Al_{84}Ni_{10}La_6$, $Al_{84}Ni_{10}(LaCeNd)_6$ and $Al_{84}Ni_{10}(LaCeNdGdY)_6$ enhance from 67 to 87, with an increase in the number of REs. Indeed, it was experimentally confirmed that the addition of multiple REs in $Al_{84}Ni_{10}RE_6$ MG increased ΔT_x together with m_{dyn}^r.

To strengthen the understanding of dynamic fragility results, viscosity change in supercooled liquid region was investigated. To measure the viscosity of the Al-based MG ribbons in the supercooled liquid region, the height (h) variation depending on time (dh/dt) of laminated ribbons was investigated by TMA under compression mode with the constant heating rate. Then the viscosity of the supercooled MG can be calculated by using the equation 3-4 :

$$F = -\frac{3\pi\eta R^4}{2L_0^3}\frac{dL}{dt} \quad . \qquad \text{Eq. 3-4}$$

In here, F is the applied force (1.2N), η is the viscosity of the MG ribbon, L is the sample thickness, which is the function of the temperature, and R is the diameter of the compression tip (1.5 mm) that imply the constant load on the sample. Figure 3.7 (a) shows viscosity changes of the $Al_{84}Ni_{10}La_6$, $Al_{84}Ni_{10}(LaCeNd)_6$ and $Al_{84}Ni_{10}(LaCeNdGdY)_6$. Dashed lines on the right side of the graph are the measured strain obtained from dividing the thickness variation (ΔL) by the original sample thickness (L_0). The initial deflection points of the viscosities and strain reflect T_g, and the temperature at the lowest viscosity (η_{min}) is T_x. The addition of multiple REs leads to a relatively smaller decrease in T_x than in T_g (=larger ΔT_x), which results in lower η_{min}, $1.1 \cdot 10^9$ Pa·s in $Al_{84}Ni_{10}(LaCeNdGdY)_6$. The measured viscosity data obtained by TMA can be described well with the following VFT relation:

$$\eta = \eta_0 exp\left(\frac{D^* \cdot T_0}{T - T_0}\right) \quad . \qquad \text{Eq. 3-5}$$

η_0 in this equation is set as $4.0 \cdot 10^{-5}$ Pa·s, D^* is the fragility parameter, and T_0 is VFT temperature when the viscosity become infinite value. Figure 3.7 (b) is the Angell plot which represent the correlation between viscosity and T_g^*/T. Indeed, the dynamic fragility by the rate of change in viscosity at $T = T_g^*$, where the temperature at equilibrium viscosity is $1.0 \cdot 10^{12}$ Pa·s, is defined as

$$m_{kin}^v = \left.\frac{d \log \eta}{d(T_g/T)}\right|_{T=T_g^*} \quad . \qquad \text{Eq. 3-6}$$

Similar with the m_{dyn}^r values, m_{kin}^v increases from 35 of $Al_{84}Ni_{10}La_6$ to 40 $Al_{84}Ni_{10}(LaCeNdGdY)_6$ with an increase in the number of REs, which means that $Al_{84}Ni_{10}(LaCeNdGdY)_6$ is a more fragile glass than $Al_{84}Ni_{10}La_6$ MG.

Indeed, a question that arises is how multiple REs in $Al_{84}Ni_{10}RE_6$ MG can have such marked effects on the dynamic behavior of MG from the microstructural point of view. Figure 3.8 is the schematic diagrams that explains the hypothetical topological structure of $Al_{84}Ni_{10}La_6$ $Al_{84}Ni_{10}(LaCeNd)_6$, and $Al_{84}Ni_{10}(LaCeNdGdY)_6$ based on the efficient cluster packing model by considering $W_{Al\text{-}RE}$ values. As mentioned before. the RE-centered clusters in Al-TM-RE MGs play an important role in the structural variation, which means that the multiple REs can remarkably change the local bonding as well as local configurational entropy. Thus, as described in figure 3.8, MGs with La-centered clusters will show relatively homogeneous bonding nature between Al and RE (W_{Al-La} = 10.167). However, addition of multiple equiatomic REs can maximize the long-range compositional fluctuation and increase the density of free volume due to a variety of $W_{Al\text{-}RE}$ from 8.1 to 10.2. Furthermore, it can be understood that a larger m_{dyn}^{r} and m_{kin}^{v} values of Al-Ni-RE MG with the addition of multiple equiatomic REs can be related to enhanced fragile manner due to much relaxed surrounding area near REcentered clusters by interrelationship as well as complex configuration space by multiple equiatomic REs with different electronegativity and atomic radius, which are distinct from those operating in $Al_{84}Ni_{10}RE_6$ MGs with a different single RE

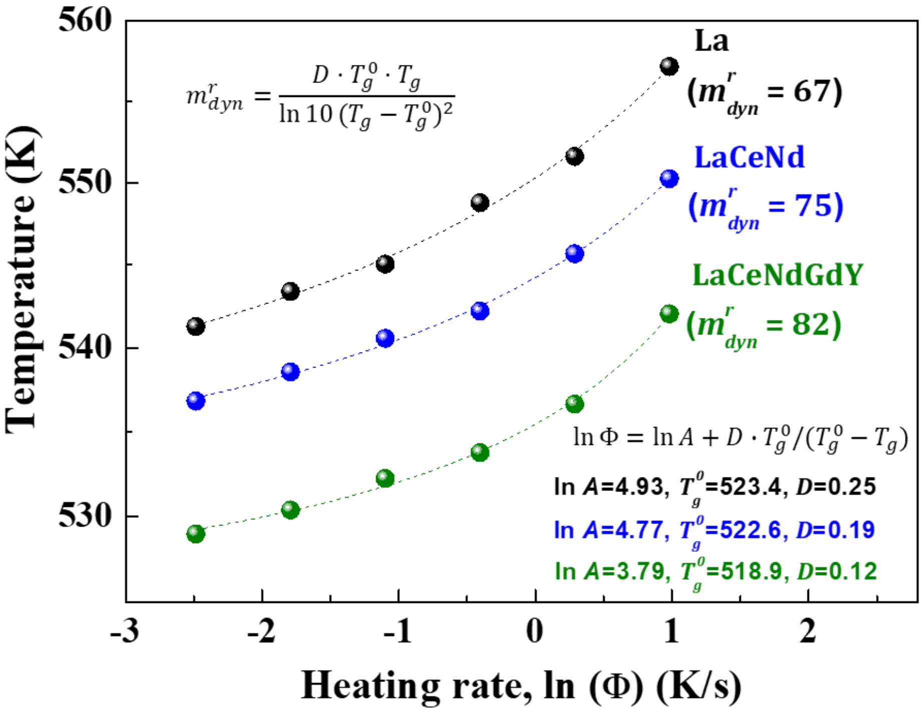

Figure 3.6. T_g variation of $Al_{84}Ni_{10}La_6$, $Al_{84}Ni_{10}(LaCeNd)_6$ and $Al_{84}Ni_{10}(LaCeNdGdY)_6$ as a function of ln(ϕ) (ϕ = heating rate).

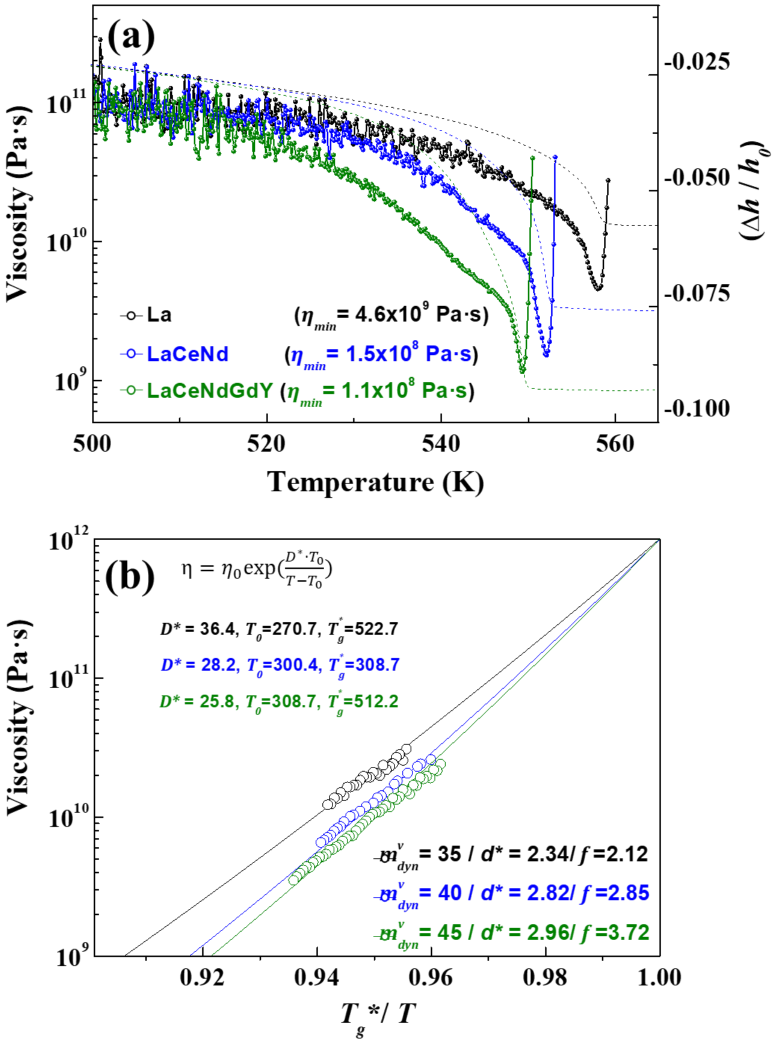

Figure 3.7. (a) Results of viscosity measurement for $Al_{84}Ni_{10}La_6$, $Al_{84}Ni_{10}(LaCeNd)_6$ and $Al_{84}Ni_{10}(LaCeNdGdY)_6$ MGs using TMA technique (heating rate: 10 K/min). Inset of $\Delta h/h_0$ (dotted lines) shows significant height drop in supercooled liquid region. (b) Viscosity versus T_g^*/T for $Al_{84}Ni_{10}La_6$, $Al_{84}Ni_{10}(LaCeNd)_6$ and $Al_{84}Ni_{10}(LaCeNdGdY)_6$ MGs

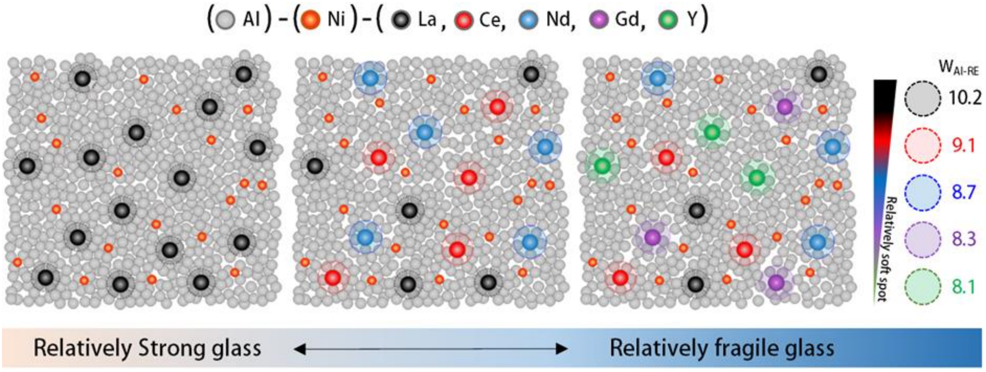

Figure 3.8. Schematic diagrams showing local structural variation depending on the change of WAl-RE for $Al_{84}Ni_{10}La_6$, $Al_{84}Ni_{10}(LaCeNd)_6$ and $Al_{84}Ni_{10}(LaCeNdGdY)_6$ MGs

3.3. Optimization of mechanical properties by addition of multiple RE elements

Through the structural investigation in chapter 3.2, it is easy to extend the influence of RE-centered clusters (higher stiffness and resistance to yield) and the resultant surrounding regions (lower stiffness and a greater tendency to undergo shear transformations) in the $Al_{84}Ni_{10}RE_6$ MGs on mechanical stability. Fig. 3.9(a) shows hardness (H) and reduced elastic modulus (E_r) in $Al_{84}Ni_{10}La_6$, $Al_{84}Ni_{10}(LaCeNd)_6$ and $Al_{84}Ni_{10}(LaCeNdGdY)_6$ MGs measured by nano-indentation test. The H and E_r values of the samples in the present study are similar within the experimental error, which results from the competition between $^{(1)}$strengthening due to larger cohesive strain energy differences by compositional fluctuation and $^{(2)}$softening due to lower value of $W_{Al\text{-}RE}$. Figure. 3.9 (b) shows the load-displacement of $Al_{84}Ni_{10}RE_6$ (RE = La, LaCeNd, LaCeNdGdY). On the loading stages with the constant loading rate (=200 μN/s), small pop-ins can be observed as a result of intermittent deformation of MGs. However, it is very difficult to compare directly the variation of amplitude and numbers of pop-ins from the load-displacement curves of $Al_{84}Ni_{10}RE_6$ (RE = La, LaCeNd, LaCeNdGdY). To identify the unclear pop-ins in loading curves in figure 3.9 (b), it is required to eliminate the influences from the increase of the indentation depth (h) and contact area in the pop-in events. A polynomial function is used to fit the loading stage in load-displacement curves to get a baseline (Figure 3.10(a–c)). After subtraction of the baseline, the pop-in events as a function of the h value are visible. Since each pop-in event reflects a formation and propagation of shear deformed zones, the depth drops (Δh, height difference between the peak and valley values as marked in Figure. 3.10(d–f)), can reflect the shear displacement size detectable by the indentation tip. However, the instrumental noise could also cause pop-in events and needs to be removed. The pop-in events free from the background noise can be extracted from the 2 seconds holding segment at peak load through linear fitting, which shows that the noise generates a shear step size of 0.4 nm in the present study. Thus, the pop-in events with shear step sizes less than 0.4 nm were not considered. After removing the noise, normalization of the *Δh* value by h is carried out to eliminate the statistical error, which generates strain burst size (S = *Δh/h*). The distributions of the S value versus the h value at a constant loading rate of 0.2 mN/s exhibit random fluctuations due to normalization process [45]. To acquire a better understanding of the mechanism in the intermittent pop-in events depending on local structural instability, we carried out a statistical analysis of *S*. Figure 11 shows cumulative probability distributions of the *S(P)* obtained from 20 different indentation curves (> 150 serrations for each sample, noise of shear step size < 0.4 nm) of $Al_{84}Ni_{10}La_6$, $Al_{84}Ni_{10}(LaCeNd)_6$ and $Al_{84}Ni_{10}(LaCeNdGdY)_6$ MGs at a constant loading rate of 0.2 mN/s. *P* can be predicted by an empirical relation: [46,47]

$$P(>S) = AS^{-\beta_s}\exp\{-(S/S_c)^2\} \qquad . \qquad \text{Eq. 3-7}$$

Here, A is a normalization constant, β_s is a scaling exponent, and S_c is the cut-off of S. The fitting parameters, S_c and β_s, reflect the dynamics of shear avalanches in MGs, which corresponds to cut-off size of self-organized shear avalanches and a tendency of a jamming/un-jamming transition of shear avalanches, respectively. Figure 3.10(b–d) show histograms for the number of strain bursts depending on S in $Al_{84}Ni_{10}La_6$, $Al_{84}Ni_{10}(LaCeNd)_6$ and $Al_{84}Ni_{10}(LaCeNdGdY)_6$ MGs. The solid lines exhibit the exponential distribution of S (slope reflects β_S) and dashed lines exhibit S_c. S_c of $Al_{84}Ni_{10}(LaCeNdGdY)_6$ MGs is much smaller than those of $Al_{84}Ni_{10}La_6$ and $Al_{84}Ni_{10}(LaCeNd)_6$. The result implies that $Al_{84}Ni_{10}(LaCeNdGdY)_6$ MG has a relatively small cut-off size of self-organized shear avalanches, which is closely related to much more formation of chaotic shear avalanches per loading (15% of all strain bursts) compared with those of $Al_{84}Ni_{10}La_6$ (5% of all strain bursts) and $Al_{84}Ni_{10}(LaCeNd)_6$ (7% of all strain bursts) as shown in Figure 3.10(b–d). Furthermore, P in $Al_{84}Ni_{10}(LaCeNdGdY)_6$ MG clearly shows the power law relation in a narrow range of S (=smaller β_S), suggesting a relatively chaotic state in the dynamics of the collective shear deformed areas. It can be suggested that larger S_c and β_S, such as in $Al_{84}Ni_{10}La_6$, preferentially formed a jamming state of shear deformed areas (self-organized deformed zone, SDZ), inducing SDZs with higher stored energy during deformation. On the other hand, with a decrease in S_c and β_S, such as in $Al_{84}Ni_{10}(LaCeNdGdY)_6$, the jammed state of the SDZs is weakened. Thus, the transition from jamming to unjamming states may occur mainly due to formation of chaotic deformed zones (CDZs) by easy destruction of elastic interaction among SDZs. The un-jamming state is unstable to perturbations exhibiting a chaotic state [46,48], which is manifested in the lack of power-law relation in the statistical distribution of strain bursts due to the influence from smaller S_c values. Indeed, the stress perturbations make it difficult to develop jamming state and finally result in successive formation of multiple CDZs at lower strain rate. The present result clearly shows that the amorphous stability depending on the number of multiple equiatomic REs in $Al_{84}Ni_{10}RE_6$ MG can change the distributions and dynamics of shear avalanches, which are strongly related to intrinsic ductility in Al-TM-RE MGs. In fact, the various REcentered clusters and their surrounding area in $Al_{84}Ni_{10}RE_6$ MG with lower S_c and β_S can act as precursors for the formation of thinner multiple shear bands due to enhanced formation of CDZs, which can distribute the applied strain more homogeneously, resulting in enhanced ductility of MG.

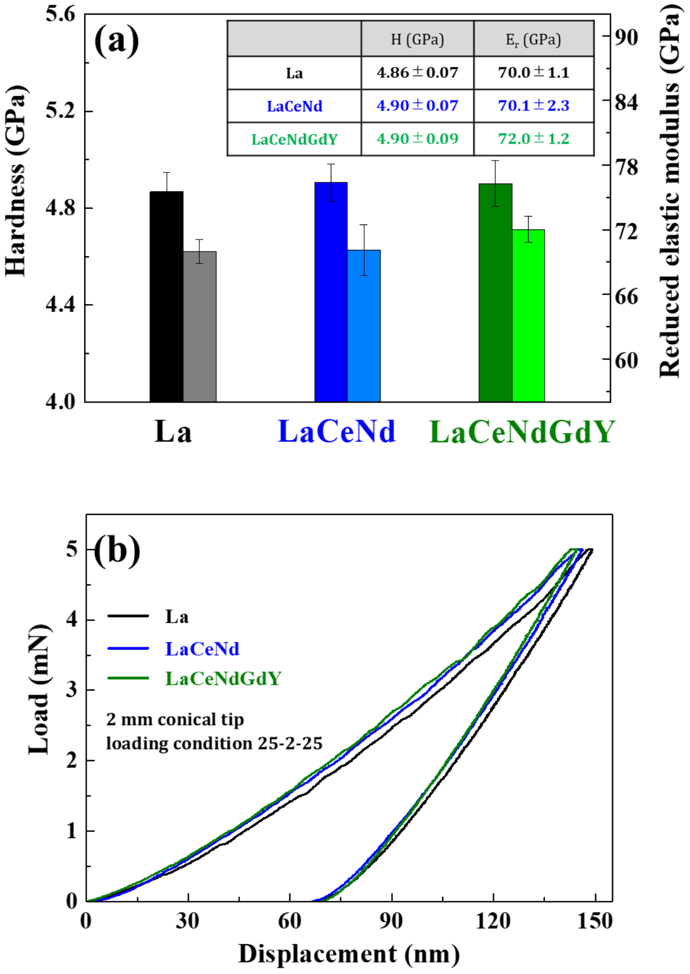

Figure 3.9. (a) Nano-hardness and (b) load-displacement curves of Al$_{84}$Ni$_{10}$La$_6$, Al Ni$_{10}$(LaCeNd)$_6$ and Al$_{84}$Ni$_{10}$(LaCeNdGdY)$_6$ MGs

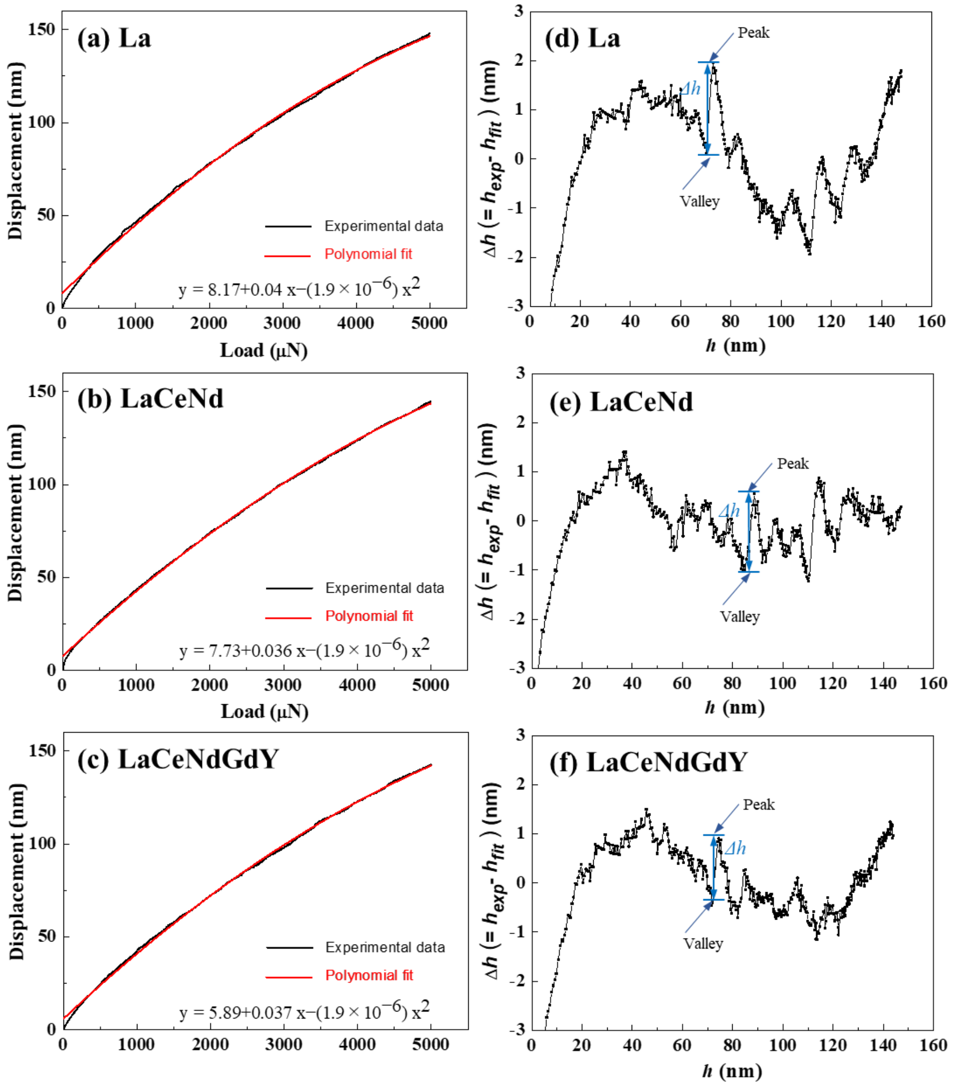

Figure 3.10. (a-c) Polynomial function fitting curves of the displacement-load for the loading segment at a constant loading rate of 0.2 mN/s, (d-f) the correlation between Δh and h showing the serration events in $Al_{84}Ni_{10}La_6$, $Al_{84}Ni_{10}(LaCeNd)_6$ and $Al_{84}Ni_{10}(LaCeNdGdY)_6$ MGs respectively.

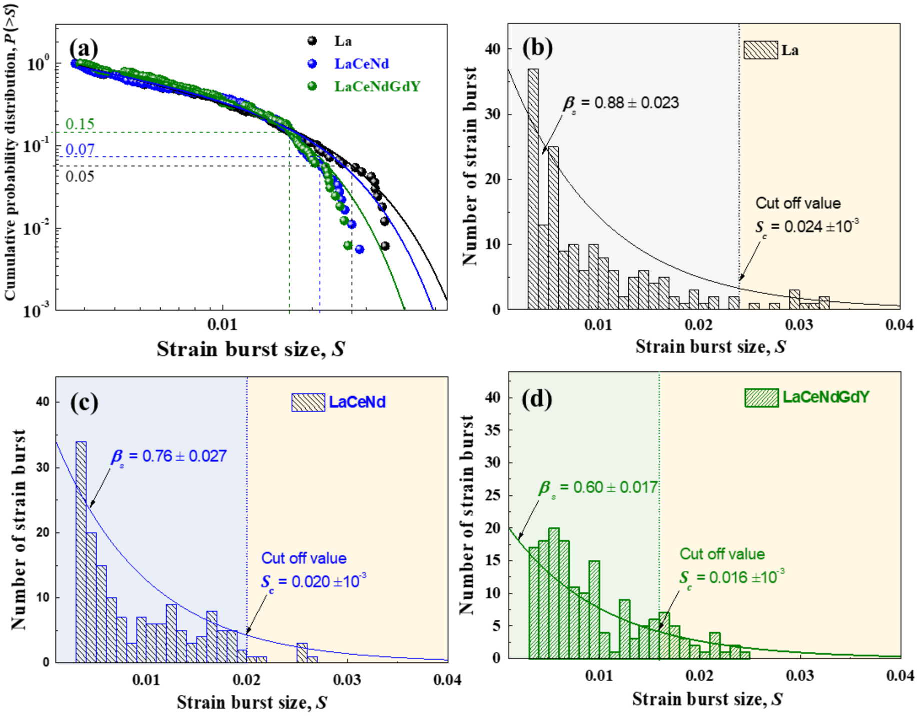

Figure 3.11. (a) Cumulative probability distributions of strain burst size of $Al_{84}Ni_{10}La_6$, $Al_{84}Ni_{10}(LaCeNd)_6$ and $Al_{84}Ni_{10}(LaCeNdGdY)_6$ MGs measured by the nanoindentation test. Solid lines are fitting curves by equation 3-6. (b–d) Histograms for the number of strain bursts depending on the strain burst sizes in $Al_{84}Ni_{10}La_6$, $Al_{84}Ni_{10}(LaCeNd)_6$ and $Al_{84}Ni_{10}(LaCeNdGdY)_6$ MGs. The solid lines exhibit the exponential distribution of S (Slope reflects β_s) and dashed lines exhibit cut-off value of strain bursts (S_c).

3.4. Summary

In this chapter, based on the Miracle's topological model, effect of addition of multiple REs on thermal properties was systematically investigated. It was confirmed that addition of multiple REs induces the complex bonding nature (fragility ↑) and systematically tuned the thermal properties including T_g and T_x. This resulted in the increased super-cooled liquid region (liquid stability ↑) of $Al_{84}Ni_{10}RE_6$ MGs. In addition, crystallization mode of $Al_{84}Ni_{10}RE_6$ MGs can be changed from eutectic crystallization to primary crystallization by the proper selection of REs (tuning of electronegativity difference). It is expected that these results can give us the good guideline for development of Al-based MGs with large super-cooled liquid region and advanced mechanical properties

Chapter 4.

Phase stability and crystallization behavior of $Al_{90-x}Ni_{10}MM_x$ MG

4.1. Introduction

Metallic glass composite formed via the partial precipitation of ductile crystalline phases within the amorphous matrix have novel properties including advanced strength and ductility [34]. One of the most advisable property tuning for mechanical applications can be achieved by partial crystallization of pure FCC-Al with the high number densities (10^{20} to 10^{23} m^{-3}) [49]. The desired crystal size and population can be introduced by quenching the homogeneous liquid alloy into the fully amorphous state followed by subsequence annealing. It is essential to consider that Al nanocrystalline phases can be grown only by diffusion of RE atoms out of the sites occupied by the nanocrystals [24,25,34]. Thus, precipitates consisted with pure Al will be surrounded by a solute enriched region. Consequently, introduction of soft FCC-Al, crystalline interface, and the solute-enriched area can effectively tune the mechanical properties.

In this chapter, systematic investigation related with the primary crystallization behavior of FCC-Al is carefully conducted. Based on the knowledge on the phase stability of Al-based metallic glasses (chapter 3), $Al_{90-x}Ni_{10}MM_x$ MGs (x= 2,4,6) was chosen to investigate the primary crystallization behavior. MM is the Ce rich misch metal (MM = $Ce_{50.2}La_{25.3}Nd_{19.5}Pr_{4.99}$) that can enhance the configurational entropy of the system and yield the enhanced glass stability. It was also reported that ratio of MM can change the thermal properties together with crystallization behavior of the system [50]. To understand the crystallization behavior for novel MG composites, firstly, thermal properties are discussed with and comprehensive nucleation thermodynamics. And microstructure change in MM2 is also studied.

4.2. MM addition effect on thermal properties

Different elements and compositional ratio in Al-TM-RE can change the local bonding structures which can result in the tuning of thermal properties and crystallization behaviors. Figure 4.1 is the diagram that shows the crystallization mode and ΔT_x of Al-Ni-MM system, changed with the compositional ratio. The blue line in the diagram is the $\lambda^{0.1}$ line (λ_0=0.1) connecting the minimum solute concentration for in Al-Ni-MM system. Supported by Egami and Waseda's topological instability model explaining amorphization boundary in binary system, the ratio of solute (i) to aluminum solvent (Al) metallic radius (r_i/r_{Al}) in multiple alloys was discovered to have the empirical relation with composition C_{min}^{i} through the topological instability parameter λ_0, if that is $\lambda_0 \approx 0.1$ [51]

$$\lambda = \sum_{i=B}^{Z} C_i \left| \left(\frac{r_i}{r_{Al}}\right)^3 - 1 \right| \approx 0.1 \qquad . \qquad \text{Eq. 4-1}$$

Thorough the experimental inspections confirming the correlation between λ_0 and the crystallization behavior, $\lambda_0 > 0.100$ resulted in polymorphous or eutectic crystallization under continuous heating, while nanocrystallization of FCC-Al occurred whenever $\lambda_0 < 0.100$ [20,52]. Calculated $\lambda^{0.1}$ line in Al-Ni-MM system is well-matched the experimentally confirmed crystallization mode. So, it is concluded that this "cluster line method" can be proposed to find out the optimal compositions for glass formation in the Al-TM-RE system.

Due to the bond strengthening effect induced by the strong s-p orbital interaction between Al and TM [51], addition of TM can distort the backbone structure of Al-TM-RE metallic glasses. However, the large and strong d-bonding character of RE atoms effectively suppress the Al-MRO and enhance the icosahedral SRO [53.54]. Based on these factors, $Al_{90-x}Ni_{10}MM_x$ (x=2,4,6) system with fixed Ni were chosen to inspect the primary nanocrystallization behavior.

Figure 4.2(a) shows the DSC traces obtain on continuous heating of the $Al_{90-x}Ni_{10}MM_x$ (x=2,4,6 at%) amorphous system. Observation of T_g and T_x was conducted with the heating rate of 20K/min from room temperature to 700 K via DSC 8500 (Perkin elmer), and the inspection of melting points was inspected in the temperature range of 800 K to 1200 K with the heating rate of 10 K/min by TGA/DSC 1+ (Metler toredo). Addition of the MM can produce the higher portion of RE-centered icosahedral cluster that enhance phase stability of the amorphous matrix. Stabilized liquid stability in MM6 results in a clear T_g at 536.8 K and 19K of ΔT_x. While, MM2 and MM4 alloys show no obvious endothermic peak related to glass transition but wide crystallization peak with relatively low T_x at 407.0 K for MM2 and at 506.1 K for MM4. T_m of alloys was increased from 1096 K to 1170 K with the addition of MM. But, T_s of the alloys almost similar with each other. Figure 4.3(a) is the XRD results of the as-spun MM2, MM4 and MM6 and figure 4.3(b) the annealed ribbon up to their peak temperature of the first peak respectively. All XRD patterns exhibit the diffused halo peak with the second shoulder at 45°. Peak position of the two halo peaks are corresponded to the peak of FCC-Al, and the intensity is inversely proportional to the MM contents. From the result of DSC and XRD, one can expect that high density of Al-MRO or FCC-Al are embedded in the amorphous matrix. And addition of MM systematically reduces the degree of Al clustering.

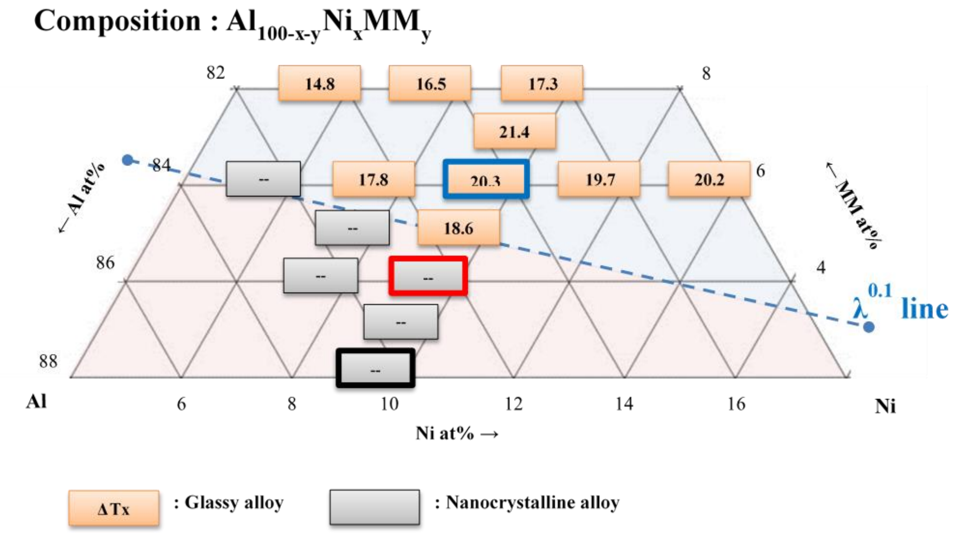

Figure 4.1. Compositional triangles for Al-Ni-MM system. the numbers in each point represent the width of ΔT_x. below the $\lambda^{0.1}$ line, amorphous alloys show no clear T_g and have the primary crystallization behavior.

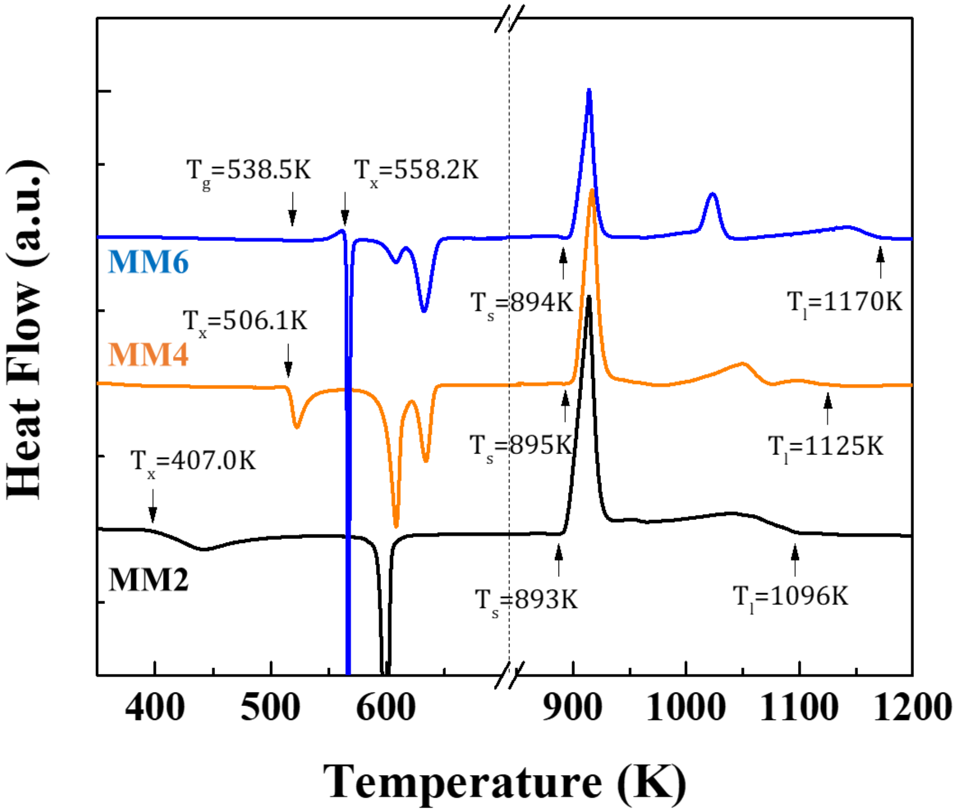

Figure 4.2. DSC traces of as-spun MM2, MM4 and MM6 MGs. From room temperature to 700 K, T_g and T_x were measured by DSC 8500 with the heating rate of 20 K/min. From 800 K to 1200 K, T_s and T_l were measured by TGA/DSC 1+ with the heating rate of 10 K/min

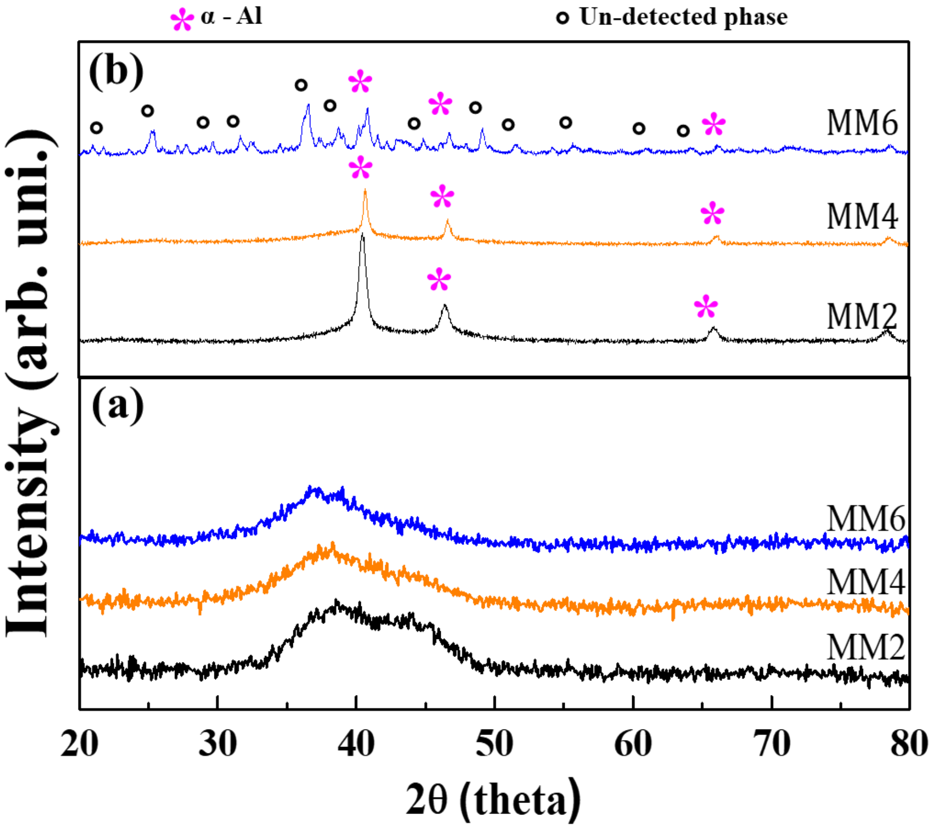

Figure 4.3. (a) XRD results of as-spun MM2, MM4, MM6 (b) annealed MM2, MM4, MM6. For annealing, samples were annealed up to 552 K (for MM2 and MM4), and 565 K (for MM6) with the heating rate of 20 K/min.

4.3. Partial distribution function for structural investigation

For the quantitative investigation of the atomic level structural variations induced by the MM contents on the Al-Ni-MM system, partial distribution function (PDF) is calculated via the electron diffraction measurement. Figure 4.4 (a), (b) is SAED pattern of as-spun MM2 and MM6 obtained from HR-TEM with 265 nm aperture. While XRD results detect no shape crystalline peaks, SAED pattern of MM2 identifies clear second ring and the bright spots that are identifies as FCC-Al. SAED pattern of MM6 also shows second ring, but no crystalline spot is detected. Thus, MM2 can be determined as the MG composite with the nanocrystals. Figure 4.3(c) is the rotational average intensity profile of MM2, MM6 obtained from the electron diffraction pattern. Average intensity profile can be expressed as $i(k) = (I'(k) - Nf)/Nf^2$, which is a function of reciprocal space (k(Å^{-1})). Through the derivation of reduced intensity function ($\phi(k) = ki(k) = \frac{I'_{eu} - Nf^2}{Nf^2} k$), reduced density function [$G(r) = \frac{2}{\pi} \int \phi(k) \sin kr \, dk$] reflect the number of atomic bonding of real space can be calculated. In this research, calculation processes for the above equations was done by using RDFTools software plugged-in a Gatan Digiatal Micrograph [55].

In the calculated RDF, MM6 shows the lower first peak intensity compared with MM2, but the 2nd intensity maxima is clearly detectable only in the results of MM2. It is reported that the atomic bonding length between Al and RE is around 3.2Å, 2.5 Å for Al-Ni bonding, and 2.7 Å for Al-Al bonding [52, 56]. Thus, it can be understood that the first maximum peak in the RDF is corresponded to mainly the Al bonding, and the second maximum peak is resulted from Al-RE bonding. The peak intensity corresponding to the Al-RE bonding is increased with the MM contents, this means that the addition of RE elements effectively yield the quasi-static RE centered clusters. [24,37]

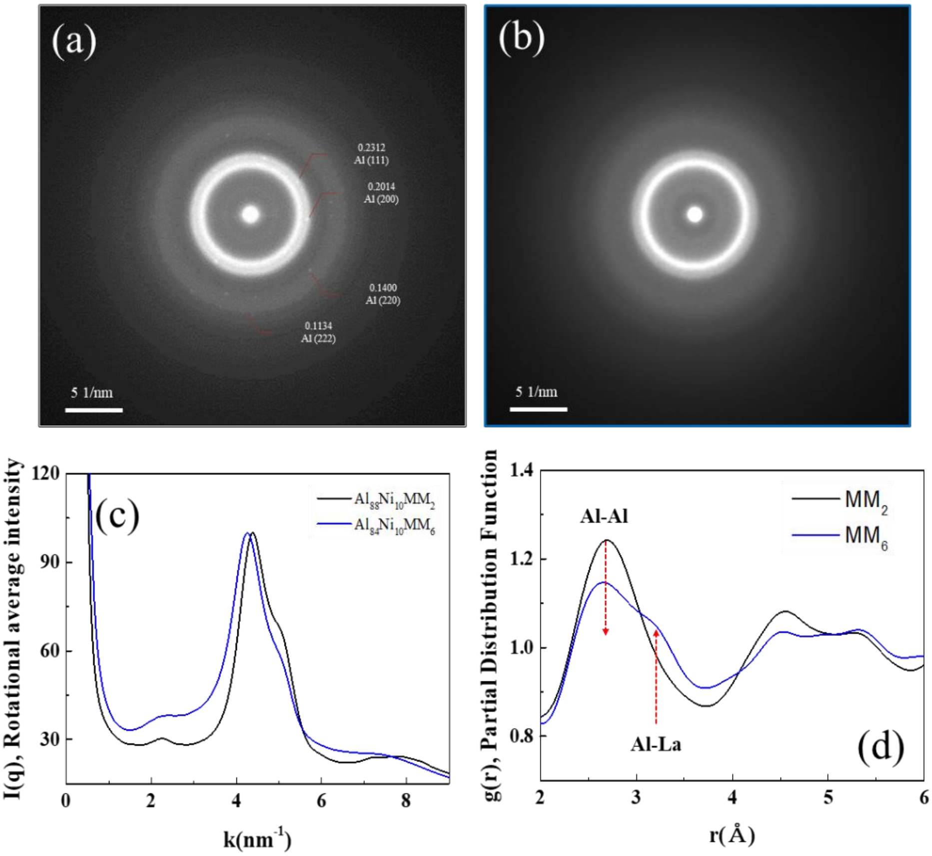

Figure 4.4. Selected area electron diffraction (SAED) pattern of the (a) MM2 and (b) MM6 amorphous alloys obtained by using the SA aperture with 230 nm diameter. (c) Intensity profile of the MM2, MM6 collected from the diffraction pattern. And (d) reduced density function, fourier transformed from the rotational average of the diffraction pattern.

4.4. Thermodynamic comprehension on the nucleation of FCC-Al

4.4.1 Asymmetric eutectic coupled zone

DSC study for melting temperature confirmed that $Al_{90-x}Ni_{10}MM_x$ (x=2,4,6) alloys are placed in the off-eutectic side. So, one can consider that dendritic growth of Al_3RE compounds should be precipitated followed by eutectic growth is expected. Based upon this composition range, FCC-Al nanocrystal is not favorable phase that can be precipitated from the metastable amorphous matrix of MM2 and MM4. However, considering of the kinetic competition during nucleation is necessary. This phase competition can be determined by the relative amplitude of the nucleation activation barrier, ΔG^*, which can be defined as $\Delta G^* = (\sigma_{s/l})^3/(\Delta G_v)^2$, where $\sigma_{s/l}$ is the interfacial energy between liquid and solid and ΔG_v is free volume energy. Consequently, the favored product phase at the given composition and temperature can be decided by the tangent point on the phase free energy curve that is parallel to the tangent to the tangent to the amorphous phase free energy curve as shown in figure 4.5 [61].(quantitative determination of ΔG^* of FCC-Al will be discussed in the chapter 4.3.3)

Due to the growth characteristics of the dendrite and eutectics, the actual phase observed will be the stable or metastable phase with the highest growth/tip temperature. This leads to the formation of a coupled zone representing the growth temperature/composition region [97]. It is well known that there are two types of coupled zone. One is symmetrical about the eutectic growth and the other is asymmetric that related with off-eutectic [57]. The symmetric coupled eutectic zone can be accounted for the regular eutectic growth, which involves the very center of eutectic composition. Whereas, an asymmetric coupled zone normally associated with irregular eutectic growth, and solid solution phase (=FCC-Al) is distorted toward the faceted phases ($Al_{11}MM_3$ or Al_3MM) due to the persistence of growth problems even at the high undercooling. If the system is glass former, faster cooling rate is given beyond that the growth rate of FCC-Al and compounds can vitrify the undercooled liquid. Consequently, actual phase diagram would be twisted, and glass forming regions should be considered together.

Consideration of nucleation activation energy (=parallel tangential model) and growth rate (=asymmetric eutectic coupled zone model) can suggest the schematic phase diagram as drawn in Figure 4.5. Liquidus line of FCC-Al can be extended below the eutectic composition. Extended liquidus line expand the FCC-Al area toward the off-eutectic composition. This skewed eutectic coupled zone results in the growth rate versus temperature relation as shown in figure 4.6(a) and (b). Melt-spun MM2 is the alloy possessing the nanocrystal in amorphous matrix. This means that the cooling rate given by melt-spinning process is stand in between critical rate for amorphous composite and crystal cooling rate for monolithic amorphous (figure 4.6(a)). While, composition of MM6 (figure 4.6(b)) is placed far from the FCC-Al phase region, and GFA is relatively larger than MM2.

The prediction of FCC-Al via asymmetric eutectic coupled zone seems reasonable. But this is rather improper because within the hypereutectic composition range, the thermodynamic driving force for crystallization prefers the Al rich intermetallic phase over the FCC-Al. it is reasonable to consider that the primary crystallization is promoted by a nucleation catalyst [22,23]. Thus, exact evaluation of nucleation thermodynamic is required further.

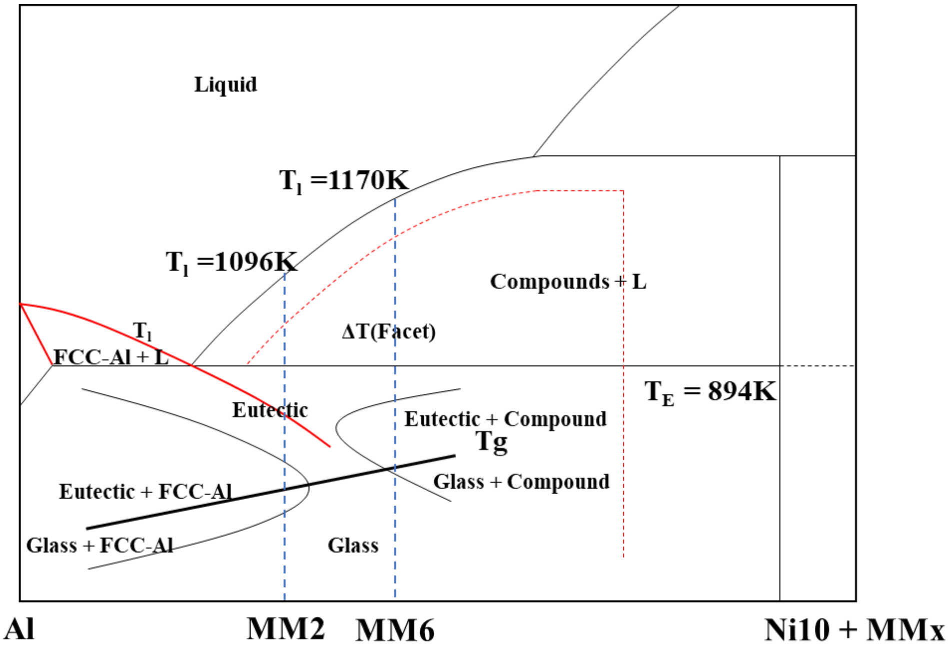

Figure 4.5. Schematic phase diagram showing a skewed eutectic coupled zone, glass forming and composite-forming regions related to the compositions

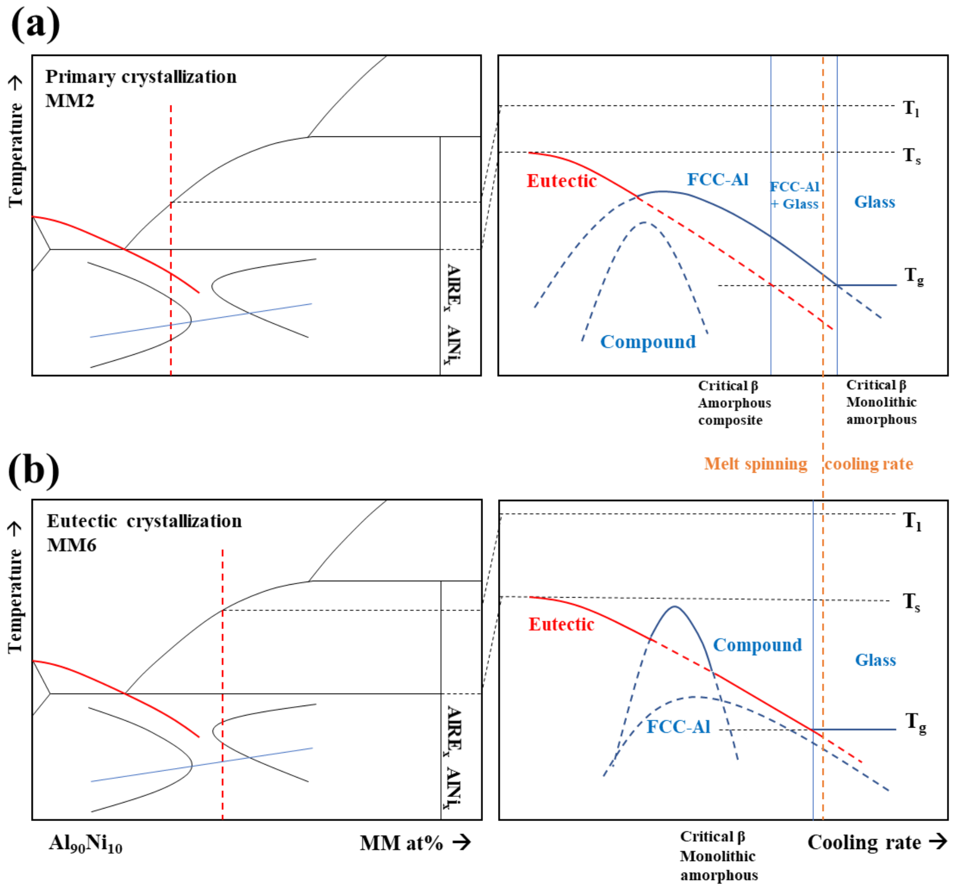

Figure 4.6. (a) Diagram showing growth temperature of the constituent in MM2 as a function of growth rate and the same growth temperature diagram for (b) MM6.

4.4.2. Nucleation thermodynamics of FCC-Al

In analyzing the crystallization behavior in Al-based metallic glasses, it is recognized that the MRO regions are considered to act as catalytic sites that promote Al nucleation [58-60]. As illustrated in figure 4.7, Al-MRO works as a core and Al atoms diffuse into the MRO to grow into nanocrystals. Al nanoparticles can grow only by moving RE atoms out of the crystallized volume and leave the solute-enriched area around nanocrystal. This means that as the nanocrystal growing, the MRO/glass interface state would be replaced by the MRO/crystal/glass interface. For the MRO catalyzed nucleation, nucleation activation energy, ΔG, can be derived as [60]:

$$\Delta G = \frac{4\pi}{3}(r^3 - r_0^3)\Delta G_v + \left[4\pi r_0^2\left(\sigma_{\frac{MRO}{cryst}} - \sigma_{\frac{MRO}{glass}}\right)\right] + 4\pi r^2 \sigma_{cryst/glass} \quad . \qquad \text{Eq. 4-2}$$

Because of the same chemical bonding nature, it is possible to assume that the interfacial energy between MRO/glass is same with that of crystal/glass. Then, ΔG^* can be finalized as equation below :

$$\Delta G = \frac{4\pi}{3}(r^3 - r_0^3)\Delta G_v + 4\pi r^2 \sigma_{cryst/glass} \quad . \qquad \text{Eq. 4-3}$$

As explained before, the volume free energy (ΔG_v) for FCC-Al in $Al_{90-x}Ni_{10}MM_x$ could be calculated by the parallel tangent method (figure 4.8) [61].

$$\Delta G_V = G_{FCC,Al} - (G_L - X_{Ni}\frac{\delta G_L}{\delta X_{Ni}} - X_{Ce}\frac{\delta G_L}{\delta X_{Ce}} - X_{La}\frac{\delta G_L}{\delta XL_{La}} - X_{Nd}\frac{\delta G_L}{\delta X_{Nd}}) \quad . \text{ Eq. 4-4}$$

$$G^L = refG^L + mixG^L + exG_{bin}^{liquid} + exG_{ter}^{liquid} \quad . \text{ Eq. 4-4-1}$$

$$refG^L = x_{Al}\cdot G_{Al}^{liquid} + x_{Ni}\cdot G_{Ni}^{liquid} + x_{Ce}\cdot G_{Ce}^{liquid} + x_{La}\cdot G_{La}^{liquid} + x_{Nd}\cdot G_{Nd}^{liquid} \quad . \text{ Eq. 4-4-2}$$

$$mixG^{liquid} = RT(x_{Al}\ln x_{Al} + x_{Ni}\ln x_{Ni} + x_{Ce}\ln x_{Ce} + x_{La}\ln x_{La} + x_{Nd}\ln x_{Nd}) \quad . \text{ Eq. 4-4-3}$$

$$G_{XS,L} = X_{Al}X_{MM}L_{L,Al-MM} + X_{Al}X_{Ni}L_{L,Al-Ni} + X_{Ni}X_{MM}L_{L,Ni-MM} \quad . \text{ Eq. 4-4-4}$$

Interaction parameters and liquid free energies are listed in table 4.1.

Calculated free volume energy for FCC-Al in MM2 and MM4 is derived as equations below:

$$\text{MM2} : \Delta G_V^{FCC} = -8.62\cdot 10^8 + 1.007\cdot 10^6\cdot T = 1.007\cdot 10^6(T-856) \quad . \text{ Eq. 4-5}$$

$$\text{MM4} : \Delta G_V^{FCC} = -8.72\cdot 10^8 + 1.140\cdot 10^6\cdot T = 1.140\cdot 10^6(T-765) \quad . \text{ Eq. 4-6}$$

To calculate the interface energy between crystal and glass, Spaepen's dimensionless interface model is used [62]. From the simple stacking patterns for hard-sphere atoms, surface tension of solid (=interfacial energy, σ) can be obtained as below :

$$\sigma = \widetilde{\sigma} \mathrm{T_M} \Delta \mathrm{S_f} \quad . \qquad \text{Eq. 4-7}$$

$$\widetilde{\sigma} = \tilde{\delta}(\widetilde{\mathrm{H}} - \widetilde{\mathrm{T}}\widetilde{\mathrm{S}} - 0.5\widetilde{\mathrm{T}} + 0.5) \quad . \qquad \text{Eq. 4-8}$$

Where, $\tilde{\delta}$ is dimensionless thickness of interface $\widetilde{\mathrm{H}}$ and $\tilde{\mathrm{S}}$ is dimensionless fusion enthalpy and entropy, respectively. $\widetilde{\mathrm{T}}$ is temperature normalized with Tm. Detailed values are summarized in table 4.2 Interfacial energy between FCC-Al and amorphous matrix of MM2 and MM4 also can be derived to the function of temperature.

$$\mathrm{MM2} : \sigma = 0.1558 + 0.953 \cdot 10^{-5} \cdot \mathrm{T} \quad . \qquad \text{Eq. 4-9}$$

$$\mathrm{MM4} : \sigma = 0.1625 + 0.969 \cdot 10^{-5} \cdot \mathrm{T} \quad . \qquad \text{Eq. 4-10}$$

When the size of cluster is small enough, the radius, r, of cluster can be converted to the number of atoms, n, for a spherical geometry :

$$\frac{4}{3}\pi r^3 = n v_a \quad . \qquad \text{Eq. 4-11}$$

Here, v_a is the atomic volume of aluminum atom ($1.64 \cdot 10^{-29} m^{-3}$).

$\Delta G(T)$ in equation can be transfer to the function of the number of Al atoms. Figure 4.9 is the graph shows the relation of $\Delta G(n)$ and number of atoms for cluster depending on the given temperature. Owing to high surface to volume ratio, ΔG increases until reaching the maxima. After the critical nucleation size where represent the maxima of $\Delta G(n)$, ΔG decreases and volumetric term (=free volume energy) become dominant. Maxima of the curvature means the ΔG at a critical cluster radius, r^*, where can be determined from $d\Delta G/dr|_{r=r^*} = 0$, and corresponds to activation barrier for nucleation. But it should be mentioned that a nucleus at a size of n^* is not stable equilibrium which can evolve into the crystal phase. Only the nucleus larger than the upper limit value of random walk zone, Δ, can keep growing into a stable nanocrystal. Random walk zone that determines the border for further growth and drift of nucleus can be expressed as below :

$$\Delta = \frac{1}{Z\sqrt{\pi}} \quad . \qquad \text{Eq. 4-12}$$

Z is the Zeldovich factor for a spherical cluster as

$$Z \equiv \left| \frac{1}{2\pi kT} \frac{\delta^2 \Delta G_n}{\delta n^2} \right|_{n^*} \right|^{0.5} = \frac{\Delta G_v^2 v_a}{8\pi\sqrt{kT\sigma^3}} \quad . \qquad \text{Eq. 4-13}$$

Length of random walk zone(Δ) is also defined the region which is bounded by $Z = \Delta G^* - kT$. In figure 4.9, random walk zone bounded from ΔG^* is also drawn. Random walk zones of two temperature close to each other are overlapped. This implies that there might be a way to promote crystallization by more than two steps of annealing experiments.

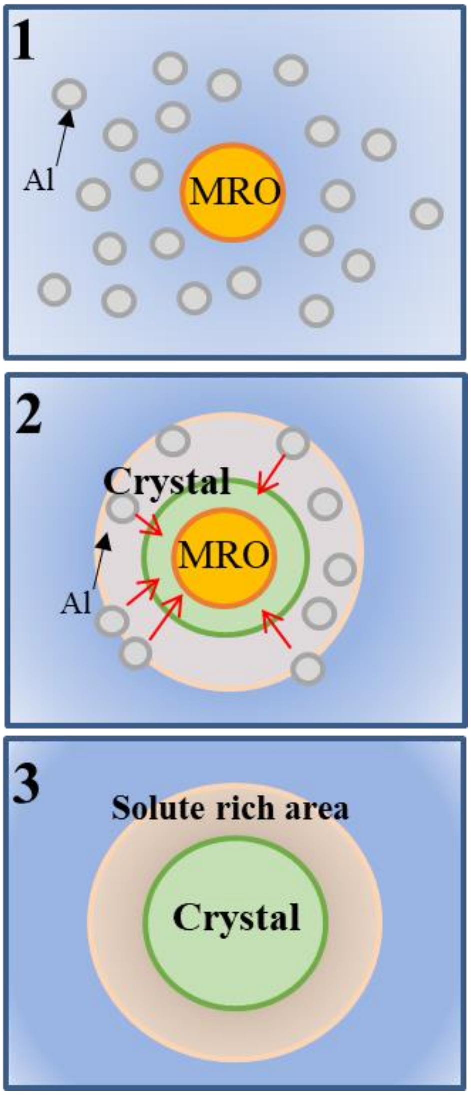

Figure 4.7. Schematics of Al-MRO model

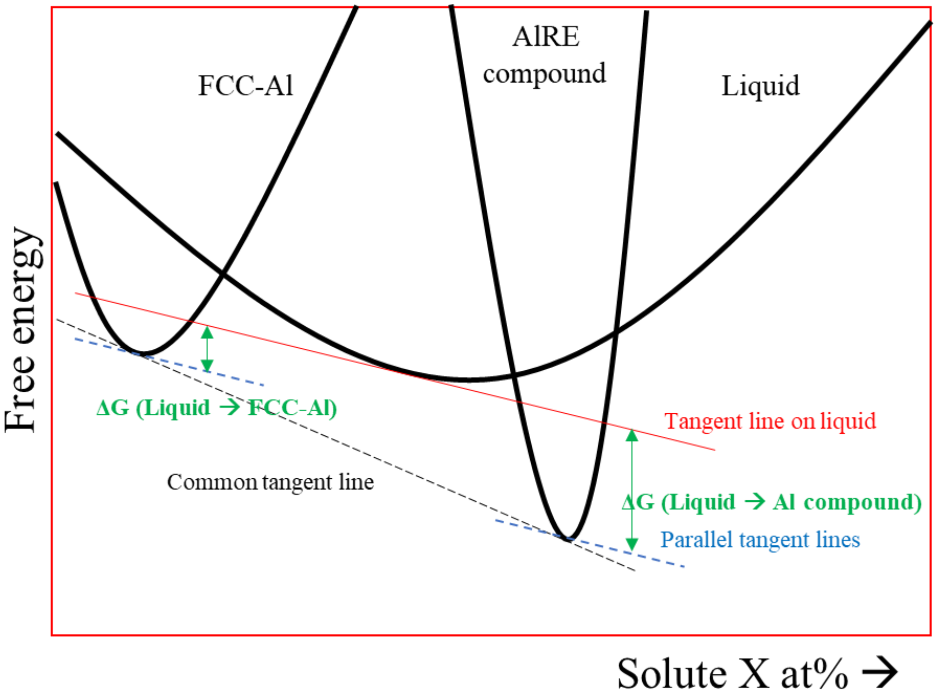

Figure 4.8. Illustration of the parallel tangent constructions to evaluate the driving force for competing crystallization reactions.

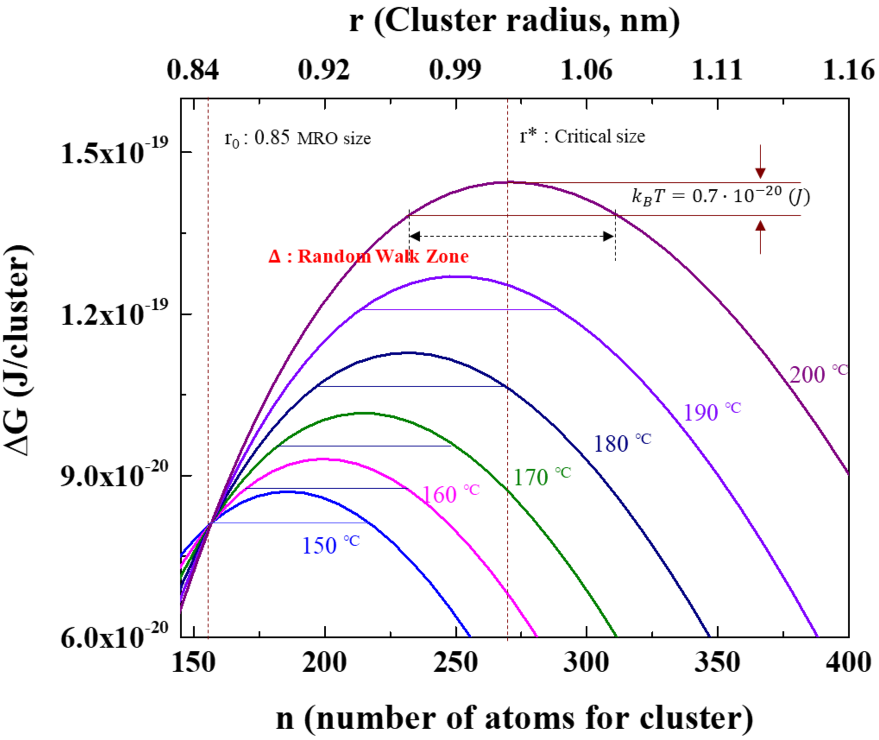

Figure 4.9. Diagram of cluster size versus free energy relationship a different temperature in $Al_{88}Ni_{10}MM_2$. The horizontal lines are the random walk zone defined by the thermal energy *kT*.

Free energy	Value
$G_{L,Al}(T < 700)$	$3028.879 + 125.251171T - 24.3671976T\ln(T) - 1.884662 \cdot 10^{-3}T^2 - 0.877664 \cdot 10^{-6} T^3 + 74092T^{-1} + 7.934 \cdot 10^{-20} T^7$
$G_{L,Al}(T > 700)$	$-271.21 + 211.206579T - 38.5844296T\ln(T) + 18.531982 \cdot 10^{-3}T^2 - 5.764227 \cdot 10^{-6} T^3 + 74092T^{-1} + 7.934 \cdot 10^{-20} T^7$
$G_{FCC,Al}(T < 700)$	$-7976.15 + 137.093038T - 24.3671976T\ln(T) - 1.884662 \cdot 10^{-3}T^2 - 0.877664 \cdot 10^{-6} T^3 + 74092T^{-1}$
$G_{FCC,Al}(T > 700)$	$-11276.24 + 223.048446T - 38.5844296T\ln(T) - 18.531982 \cdot 10^{-3}T^2 - 5.764227 \cdot 10^{-6} T^3 + 74092T^{-1}$
$G_{L,Ni}$	$11235.527 + 108.457T - 22.096T\ln(T) - 4.8407 \cdot 10^{-3}T^2 + 3.82318 \cdot 10^{-21} T^7$
$G_{L,La}$	$5332.653 + 18.23012T - 11.0188191T\ln(T) - 20.171603 \cdot 10^{-3}T^2 + 2.93775 \cdot 10^{-6}T^3 - 133541 T^{-1}$
G_{LPr}	$3848.961 - 29.099465T - 4.7344931T\ln(T) - 35.119723 \cdot 10^{-3}T^2 + 5.427467 \cdot 10^{-6}T^3 - 207406 T^{-1}$
G_{LCe}	$4117.865 - 11.423898T - 7.5383948T\ln(T) - 29.36407 \cdot 10^{-3}T^2 + 4.827734 \cdot 10^{-6}T^3 - 198834 T^{-1}$
$G_{L,Nd}$	$5350.01 - 86.593963T + 5.357301T\ln(T) - 46.955463 \cdot 10^{-3}T^2 + 6.860782 \cdot 10^{-6}T^3 - 374380 T^{-1}$
Interaction parameter	**Value**
$L_{Al,Ni}^{liquid}$	-207,109+41.32T
$L_{Al,Ni}^{FCC}$	-162.408+16.21T
$L_{Al,Ce}^{liquid}$	-154,400+64.41T
$L_{Al,La}^{liquid}$	-141,000+43.82T
$L_{Al,Nd}^{liquid}$	-150,300+58.89T
$L_{Ni,Ce}^{liquid}$	-116,660+2.248T
$L_{Ni,La}^{liquid}$	-113,090+26.350T
$L_{Ni,Nd}^{liquid}$	-100,800+14.310T

Table 4.1. Free energy and interaction parameter for constituent elements in Al-Ni-MM system. Here, MM is the Ce-rich mischmetal (Ce50.19La25.31Nd19.5Pr4.99)

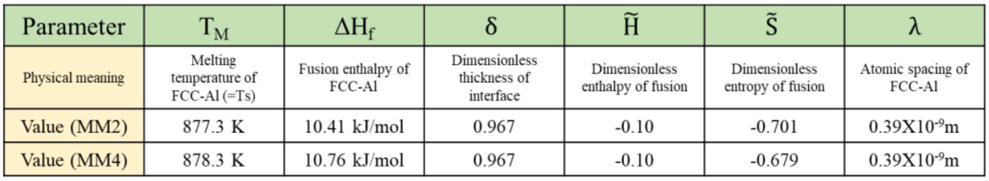

Parameter	T_M	ΔH_f	δ	$\tilde{H}$	$\tilde{S}$	λ
Physical meaning	Melting temperature of FCC-Al (=Ts)	Fusion enthalpy of FCC-Al	Dimensionless thickness of interface	Dimensionless enthalpy of fusion	Dimensionless entropy of fusion	Atomic spacing of FCC-Al
Value (MM2)	877.3 K	10.41 kJ/mol	0.967	-0.10	-0.701	$0.39\text{X}10^{-9}$m
Value (MM4)	878.3 K	10.76 kJ/mol	0.967	-0.10	-0.679	$0.39\text{X}10^{-9}$m

Table 4.2. Summary of physical meanings and exact values of the parameters for calculation of interface energy.

4.4.3. Nucleation and growth rate of FCC-Al

To achieve the deliberate precipitation condition of crystallization, nucleation and growth must be controlled. Both are also key processes to understand the glass formation behavior of undercooled liquid [63,64]. It has been suggested that sizes and distributions of crystalline phases can only be manipulated to some extent in conventional method involving quench of metallic melts. For bulk scaled glass formers such as Pb-, Zr-based multicomponent system, investigation of the crystallization velocities just below the T_m can be exploited to search the thermal pathway for manipulation of composite microstructures [65]. However, as a marginal glass former, prediction of nucleation and growth rate of Al-TM-RE were merely studies so far.

The steady state nucleation rate, I_{SS}, can be defined as [63]:

$$I_{SS} = AD \cdot exp\left[-\frac{\Delta G^*}{kT}\right] \quad . \qquad \text{Eq. 4-14}$$

Where A is a proportional constant D is the effective diffusion coefficient which is involved with the Al, ΔG^* is the activation energy for the formation of critical nucleus that can be expressed as $\Delta G^* = (16\pi/3)(\sigma^3/\Delta G^2)$. For most metallic glasses, the nucleation rate is expected to achieve their maximum rate near T_g [66]. Plus, calculated T_m of FCC-Al in MM2 and MM4 is 856 K and 765 K, respectively. Crystal growth rate, U is given by [67],

$$U(T) = \frac{D}{a}\left[1 - exp\left[-\frac{\Delta G}{kT}\right]\right] \quad . \qquad \text{Eq. 4-15}$$

Here, D represent the effective diffusion coefficient, a is average interatomic spacing. ΔG is free energy difference between liquid (or super-cooled liquid) and the crystalline phase, which can be approximated as $\Delta G = 2T \cdot \Delta H_f \cdot (T_m - T)/[T_m(T_m + T)]$, T_m and ΔH_f is the melting point and enthalpy of fusion, respectively. For the high temperature range, where the stokes-einstein relationship is applicable, D can be described as equation 4-16 and is proportional to reciprocal value of viscosity.

$$D(T) = \frac{kT}{c\eta(T)\pi R} \quad . \qquad \text{Eq. 4-16}$$

However, as Edger et al explained in their report [68], stokes-einstein relationship between viscosity and diffusivity (or growth velocity) breaks down and is replaced by a power-law relation in the form of $D^{super-cooled\ liquid} \propto \eta^{-\xi}$. As an alternative way, modified VFT relation was adapted to get the $D(T)$ of super-cooled liquid [69]. Detailed results are described in chapter 5.2.2.

Through the careful application and calculation, normalized nucleation and growth velocity of FCC-Al in MM2 and MM4 is obtained and the results are shown in figure 4.10. Dashed line is the growth rate. The growth rate of FCC-Al in MM2 and MM4 peaks at 650 K and 670 K respectively. Both homogeneous nucleation (θ = 180°) and heterogeneous nucleation with θ of 30, 60 and 90° is considered. where θ represents the contact angle between the crystal nucleus and catalyst. In the case of homogeneous nucleation (θ = 180°), the overlapped area between the growth rate and nucleation rates is not significant. As explained before, precipitation of FCC-Al is triggered from the MRO which has the same interface energy with crystals. In addition, formation of solute enriched area along the FCC-Al prevents the additional nucleation at the interface of MROs or crystals [60]. These factors claim, even though nucleation of FCC-Al is triggered from catalytic factor (= MRO, heterogeneous nucleation), actual nucleation kinetics of FCC-Al are thermodynamically homogeneous state. Nucleation and growth rate results in figure 4.10 also indicate that crystallization at large undercooling is controlled by growth kinetics, whereas the crystallization at small undercooling is nucleation limited. Thus, it is expected that the sort of asymmetry crystallization in heating and cooling processes can be observed in Al based marginal glass former as reported in Pd- Zr-based BMGs.

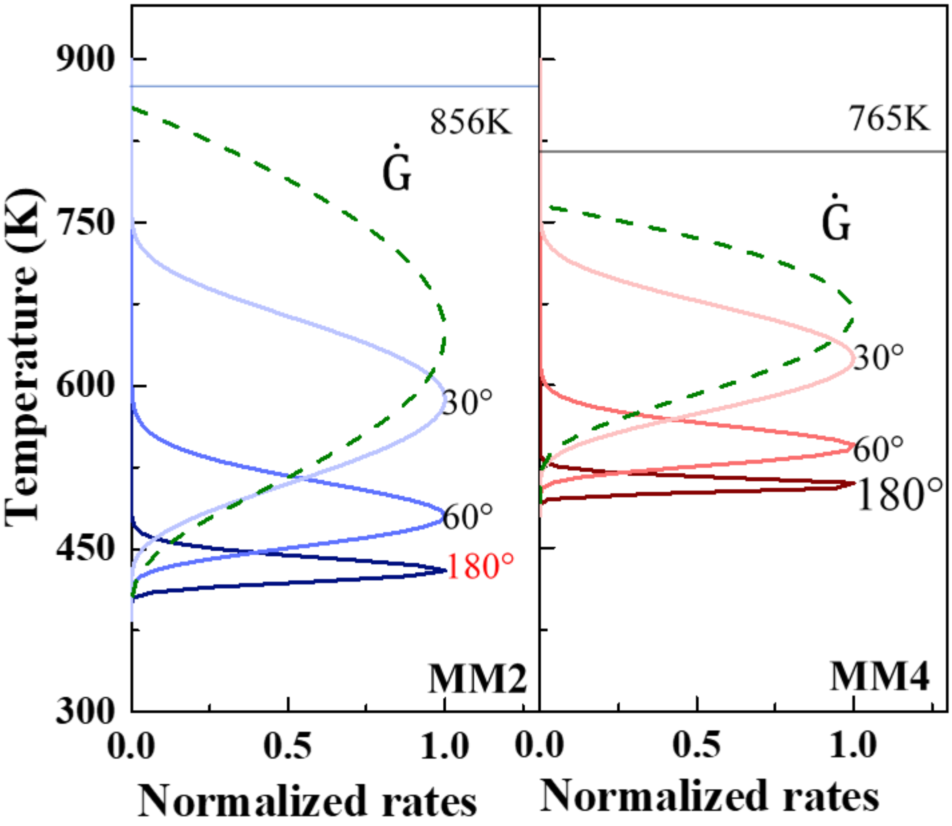

Figure 4.10. Normalized nucleation and growth rate of MM2 and MM4.

4.5. Partial precipitation of FCC-Al nanocrystals in amorphous matrix

4.5.1. Heating process for precipitation of FCC-Al

MG composite with nanocrystals were conducted via high resolution TEM. TEM images in figure 4.11 are the microstructure of (a) as spun MM2 and annealed MM2 up to (b) 440 K, (c) 465 K and (d) 552 K. For the precise controlling of heat-treatment, samples encapsulated in aluminum crucible were heated in DSC. In the as-spun state, 5% of the FCC-Al with average size of 5.2 nm are precipitated in matrix. With the annealing temperature, the volume fraction (V_f) increases up to about 55%. This value is well-matched with the calculated volume fraction. Average size of the precipitates also increased (12 nm). Normalization of integrated enthalpy of crystallization peak (blue line in figure 4.11(e)) shows that volume fraction measured by image analyzing technique is reasonable. To confirm the accuracy of HR-TEM results, in-situ SAXS profiles $I(q)$ ($q = \left(\frac{4\pi}{\lambda}\right) sin\theta$, q: scattering vector, 2θ: scattering angle, λ: wave length) were measured (figure 4.12 (a)). Incident x-ray beam was exposed for 7 seconds on the MM2 sample which was being annealed at the heating rate of 20 K/min. Except the thermal energy, no external forces were applied in the MM2 samples. From the room temperature to 523 K, intensity of interference maxima increases and the peak position shift to left side. After 606 K, intensity maxima disappears and scattered data shows linear plot. From the intensity and position of the intensity maxima, we can estimate the radius of scatterer (FCC-Al crystals) by using the equation below [70].

$$I(q) = Aexp\left(\frac{R_g^2 q^2}{3}\right) + C, (R_g^2 = \frac{R^2}{2}) \qquad . \qquad \text{Eq. 4-17}$$

Calculation of size distribution and mean size of the FCC-Al crystalline phases in annealed MM2 was determined by unified fitting plugging-in Irena tool in Igor Pro application. Figure 4.12 (b) shows the mean size of the FCC-Al fitted from the in-situ SAXS (Black line), and actual size get from the TEM image (Blue line). X-ray scattering can occur not only from the FCC crystalline phases but also from the solute enriched area around them. To interpret this complex structure, core-shell model for alloy composite is proposed. Based on a numerical study on the scattering distribution, S. Imhoff et. al derived the simple expression for scattering amplitude [34] :

$$q_{peak} = \alpha \frac{2\pi}{R_s + R_c} \qquad . \qquad \text{Eq. 4-18}$$

Where, R_s and R_c is the radius of overall scatterer (core + shell) and radius of core, respectively. q_{peak} is q value at maxima. α is the factor that depend on the solute concentration. Here, α assumed as 1.07. Size of scatterer calculated from core-shell model (Red line) and guinier plot (Black line) is summarized in figure 4.14(b). Those results are similar with each other and one can claim that fitted results from guinier plot also include the scattered data from solute-enriched area around FCC-Al. With the assumption that the concentration of atoms in the system is constant, the number of solute atoms displaced should be equal to the number added to the shell (=solute enriched are) and R_S can be expressed as

$$R_S = \left(\frac{x_{solute/shell}}{x_{solute/shell} - x_{solute/matrix}}\right)^{1/3} \cdot R_c \quad . \qquad \text{Eq. 4-19}$$

Approximate compositions of the solute enriched area around the FCC-Al can be solved using the following relation [71].

$$Al_{1-x-y}Ni_xMM_y = V_f \cdot Al + (1 - V_f) \cdot (Al_{1-V_f-x-y}Ni_xMM_y)_{1/(1-V_f)} \quad . \qquad \text{Eq. 4-20}$$

In here, x and y are the compositions of Ni and MM, respectively. Approximated composition change along the FCC-Al interfaces are displayed in figure 4.13. Input of the results of figure 4.13 and 4.12 in equation 4-18 can calculated the size change of FCC-Al with the annealing temperature. Calculated results (magenta line) in figure 4.14(a) are well-matched with TEM image analysis results. Consequently, Final form of precipitate in 552 K MM2 would have 4 nm thickness of solute-enriched area around them (figure 4.15(b)). Also, atom probe tomography results of FCC-Al in $Al_{87}Ni_{10}Ce_3$ revealed that the thickness of solute-enriched area is around 3nm [72]. Thus, calculated results for modeling of FCC-Al is reasonable.

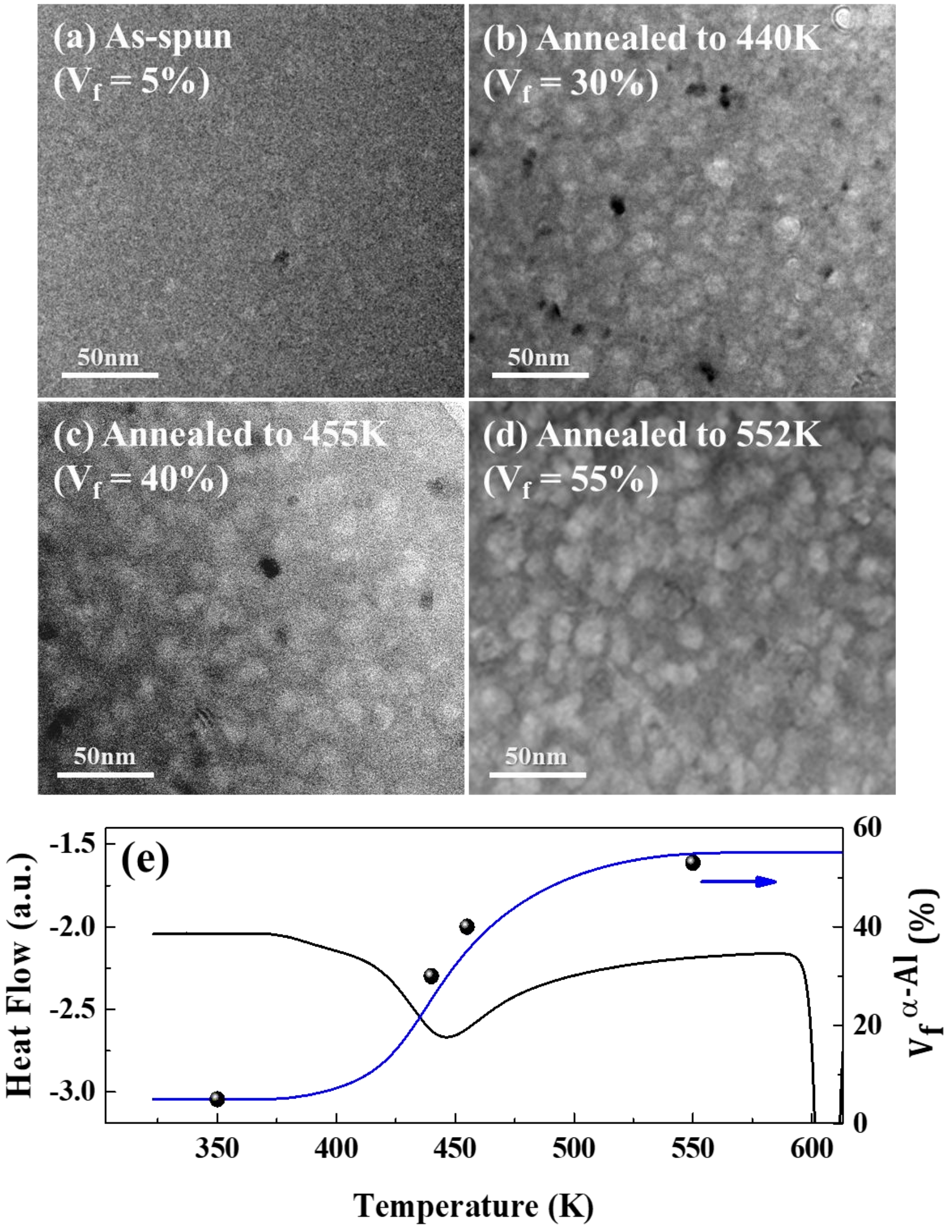

Figure 4.11. Bright TEM image of (a) as-spun MM2, and MM2 composite annealed to (b) 440 K (c) 465 K (d) 552K. V_f is the volume fraction of FCC-Al measured by image analysis technique. And (e) DSC trace (black line) and volume fraction (blue line) obtained from normalized heat flow of the crystallization peak. Dots in figure 4.11(e) are measured V_f value.

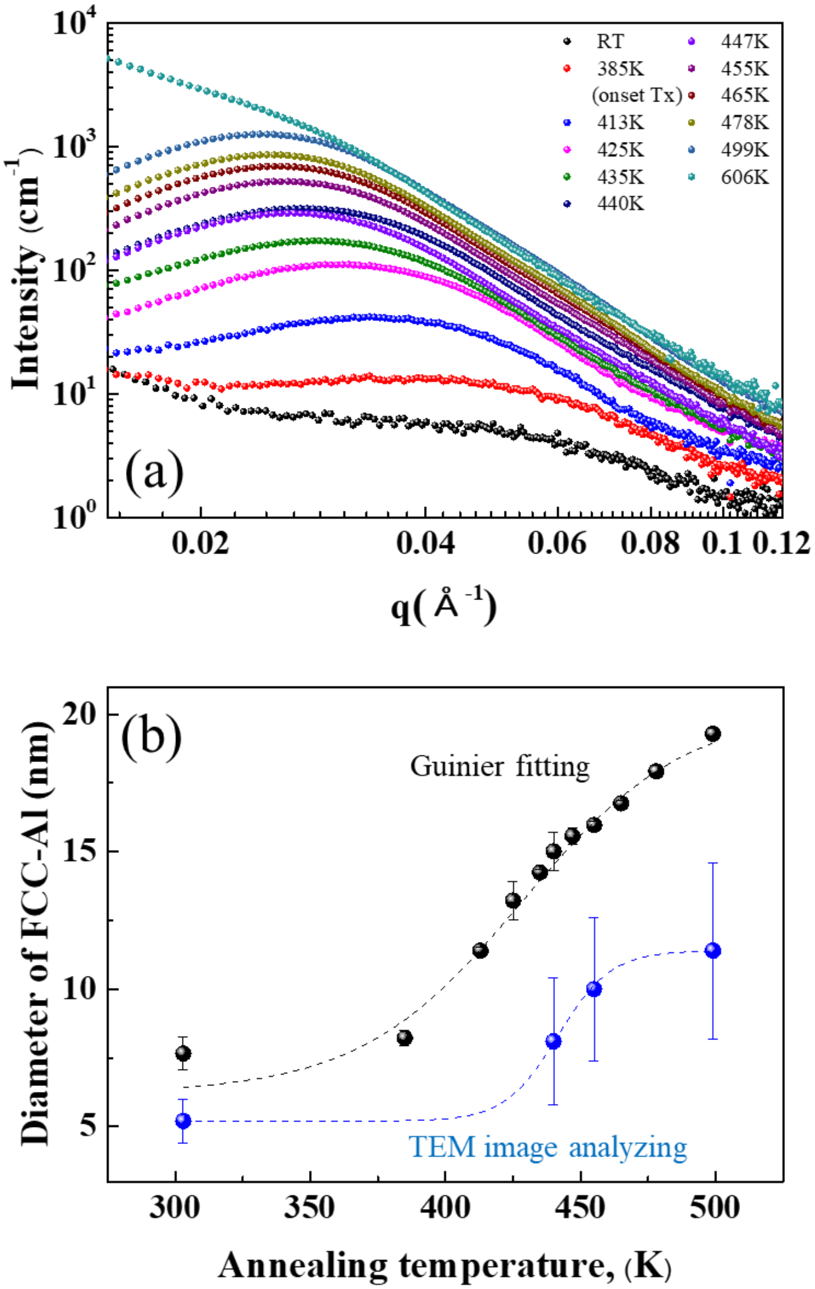

Figure 4.12. (a) In-situ small angle scattering of MM2 sample annealed with the heating rate of 20 K/min (b) diameter change of precipitated FCC-Al obtained by guinier fitting, and average diameter obtained from TEM images in figure 4.11(a-d).

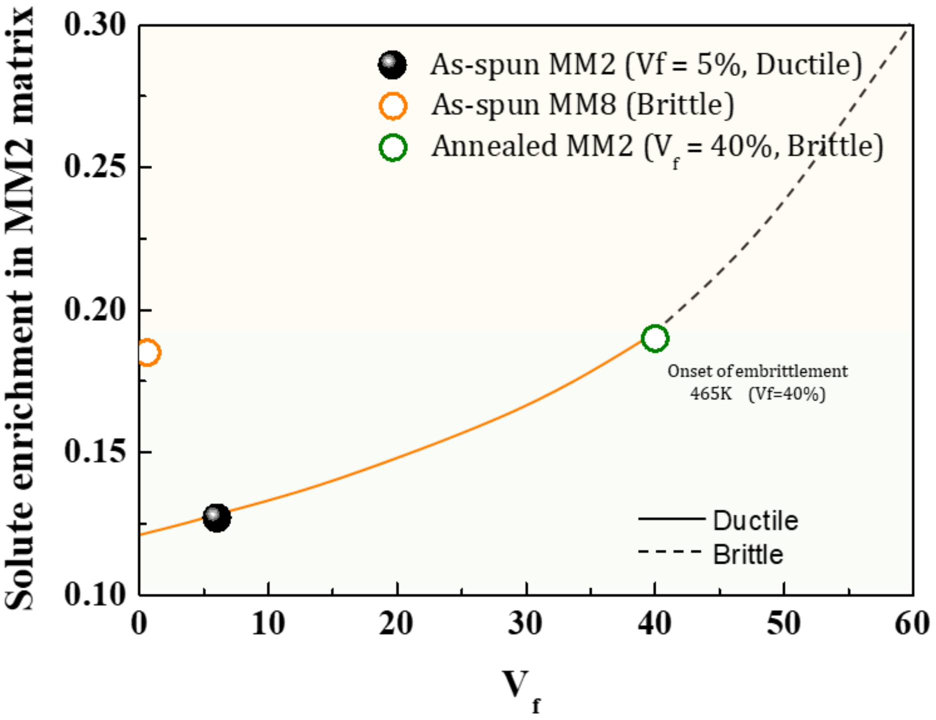

Figure 4.13. Average concentration of solute around FCC-Al as a function of V_f of FCC-Al.

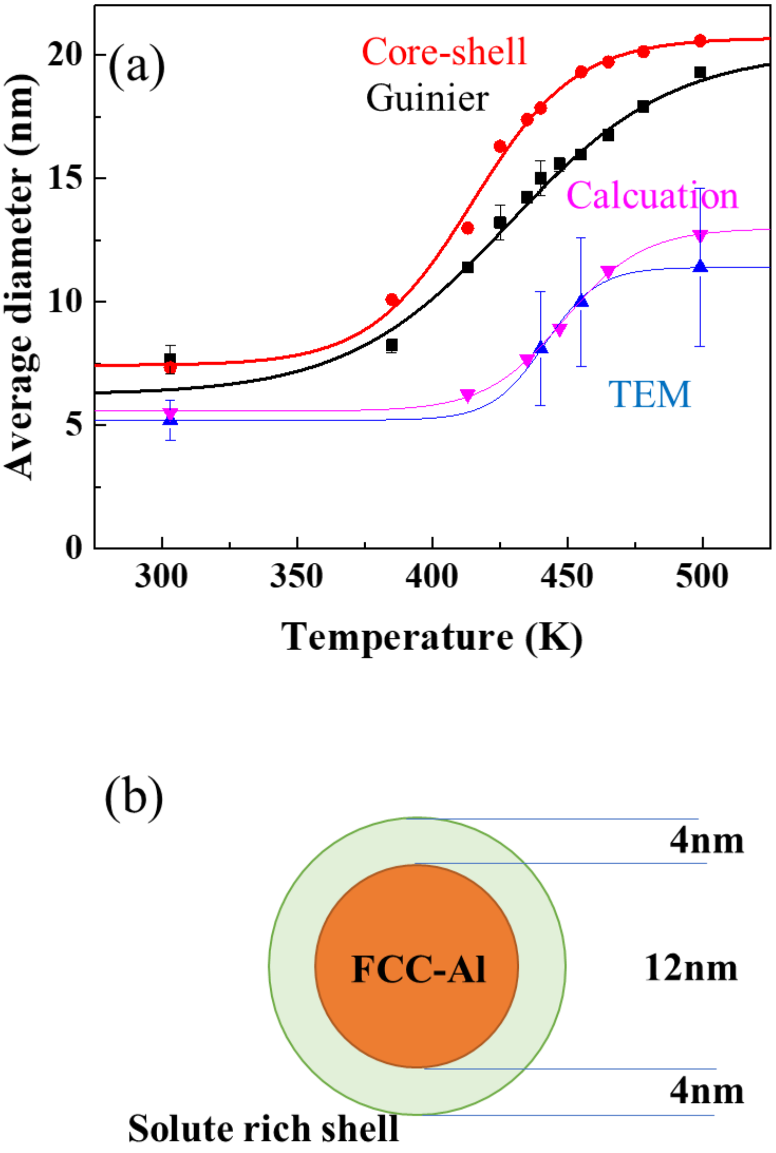

Figure 4.14. (a) Diameter of precipitated FCC-Al in MM2 versus annealing temperature. (b)final structure of FCC-Al in amorphous matrix at 552 K obtained from core-shell model.

4.5.2. Cooling process for in-situ precipitation of FCC-Al

Precipitation of crystalline phase requires enough thermal energy for diffusion of solute elements. At the same time, undercooling (driving force) is required for nucleation of crystalline phase. Thus, cooling process is also considerable issue for developing MG composite. MG composite containing “in-situ” dendritic crystalline phases is one of the widely considered issue [73]. But. cooling rate control needs the appropriate GFA of the system. So, in-situ technique for developing MG composite with marginal glass systems has not been considered.

Melt-spinning is the casting technique that can produce wide and long thin plate effectively. Cu wheel speed, melt injection force, and liquid of injected temperature are the factors that can control the solidification rate of the melt-spun alloys. Since the MM2 can form a mixing structure of glassy matrix and FCC-Al phases in ribbon form, we systematically investigated the effect of cooling rate on the phase formation and microstructure of this MG composite. To control the cooling rate, Cu wheel speed (from 3000 rpm to 1000 rpm) and nozzle size (from 1 mm to 7 mm) were adjusted. As a results of retarded cooling rate, thickness of ribbon was increased from 18 μm to 45 μm. Figure 4.15 (a) is the image of as-spun MM2 with the thickness of 18 μm, which is the same sample that was studied in previous chapter. Figure 4.15 (b) shows the TEM image of MM2 with 45 μm of thickness. From now on, as-spun MM2 with thickness of 18 μm, 30 μm and 45 μm will be denoted 18μm MM2, 30μm MM2 and 45μm MM2, respectively The precipitate size of 18μm MM2 and 45μm MM2 are nearly identical, but number density of FCC-Al in 45μm MM2 seems much higher than that of MM2. X-ray analysis was conducted to confirm the volume fraction enhancement in thicker (=slower cooling rate) MM2. Figure 4.16 is synchrotron SAXS results of 18μm, 30μm and 45μm MM2. Similar position of maxima and increased intensity clearly claim that the volume fraction of FCC-Al can be increased with the cooling rate without apparent size changes. For the detailed structural analysis, atom probe tomography (APT) analysis was performed for the 45μm MM2 sample. Figure 4.17(a) shows the APT reconstructions. At the early stage of FCC-Al growth, composition difference between the interface and the matrix is small. Thus, the morphology of Al-rich region is difficult to distinguish due to their diffused interface, but one can define the Al-enriched regions with the approximate 5 nm width. (position of Al atoms shown by green dots). Figure 4.17(b) is the line profile of the average composition from the center of the 5nm sized FCC-Al. Due to the low solubility of Al, the concentration of RE elements a in small range of distance increased. Comparison between the frequency distributions of elemental concentrations and binomial distributions are useful for quantifying the fine scale clustering effects of constituent elements in alloys [74]. Figure 4.18 is the results of the frequency distribution analysis. The deviation of the experimental frequency distribution curves (solid lines) gives the p- and μ-value. When the p-value is less than 0.05, it is assumed that the alloy is not homogeneous and there is high density of elemental clustering within the alloy. And μ-value ranges between 0 and 1, where 0 represents a random homogeneous and 1 represents a complete ordering of the constituent atoms [74]. As shown in the table inserted in figure 4.18, Al has the small p-value with 0.9 μ-value. Consequently, it was experimentally confirmed that 45μm MM2 also has the 5nm size of FCC-Al in amorphous matrix as 18μm MM2 does.

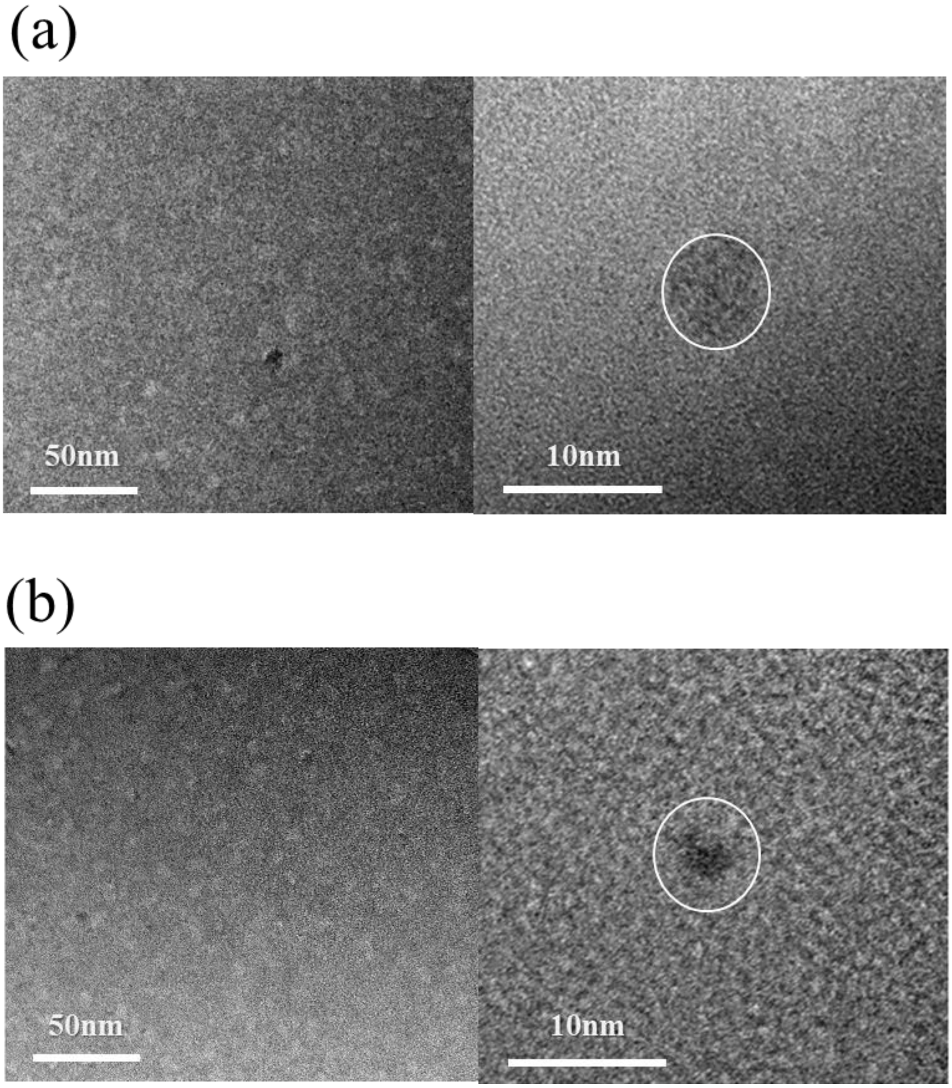

Figure 4.15. TEM images of (a)as-spun MM2 with 18 μm of thickness and (b)MM2 with 45 μm thickness, which was spun with relatively slow quench rate.

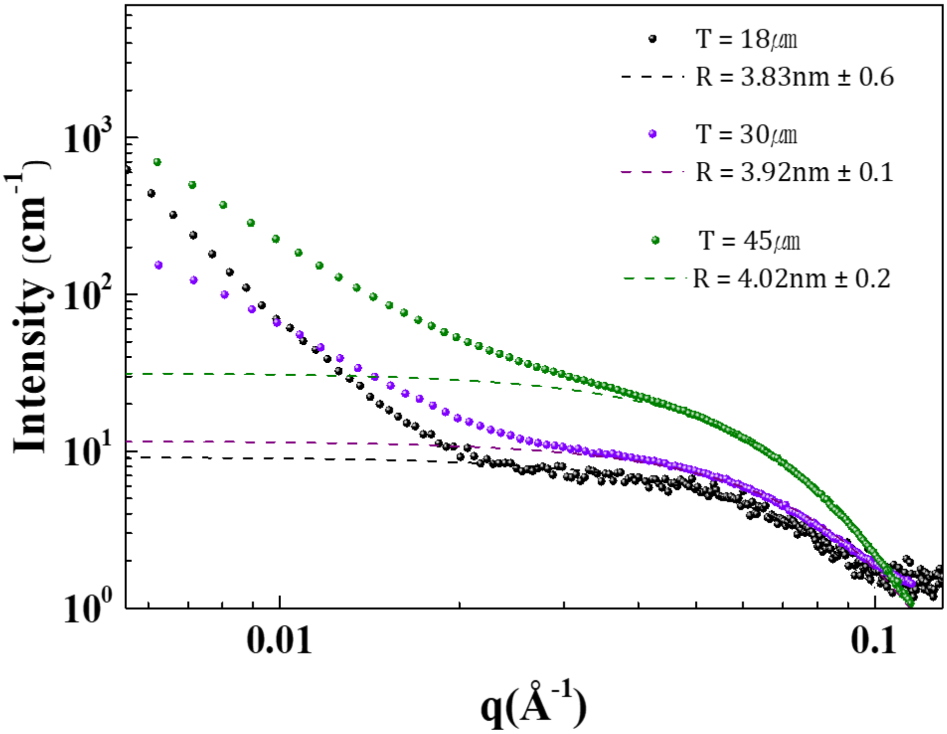

Figure 4.16. SAXS graph of MM2, 30 μm MM2 and 45μm MM2. Dashed lines are fitting results of guinier plot and calculated average size values are displayed in graph together.

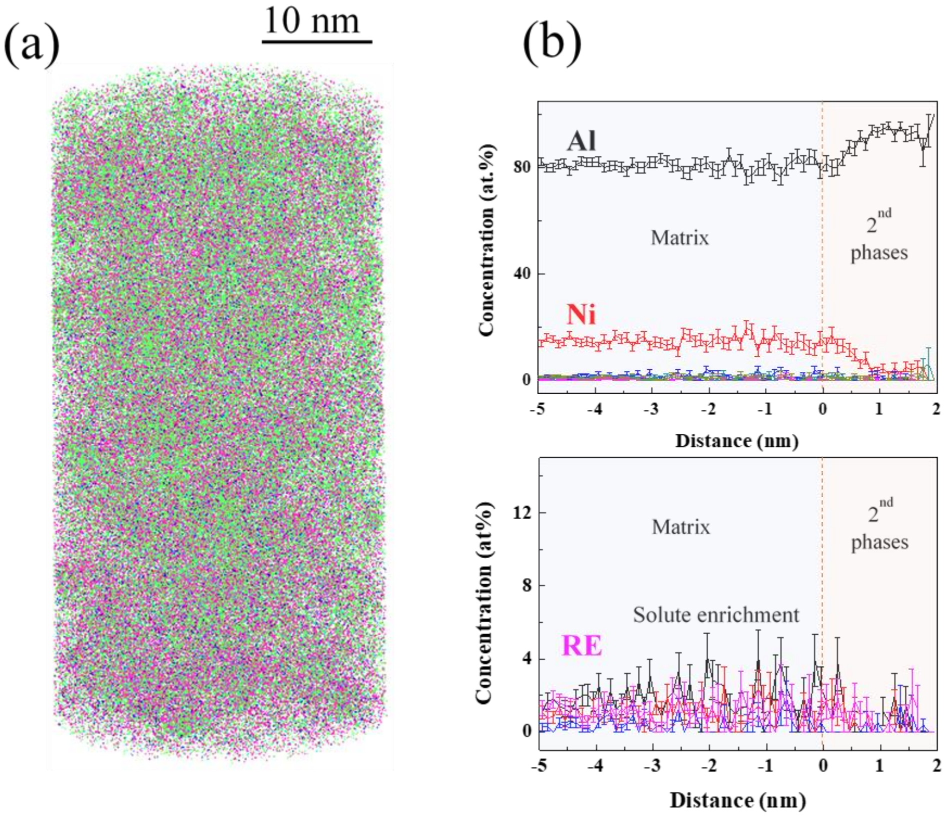

Figure 4.17. (a) APT reconstruction showing the distribution of the alloy metallic elements (Al-Green, Ni-Purple, Ce-Light blue, La-Orange, Nd-Navy blue, Pr-Blue) and (b) composition line profile from the center of the 5 nm sized FCC-Al.

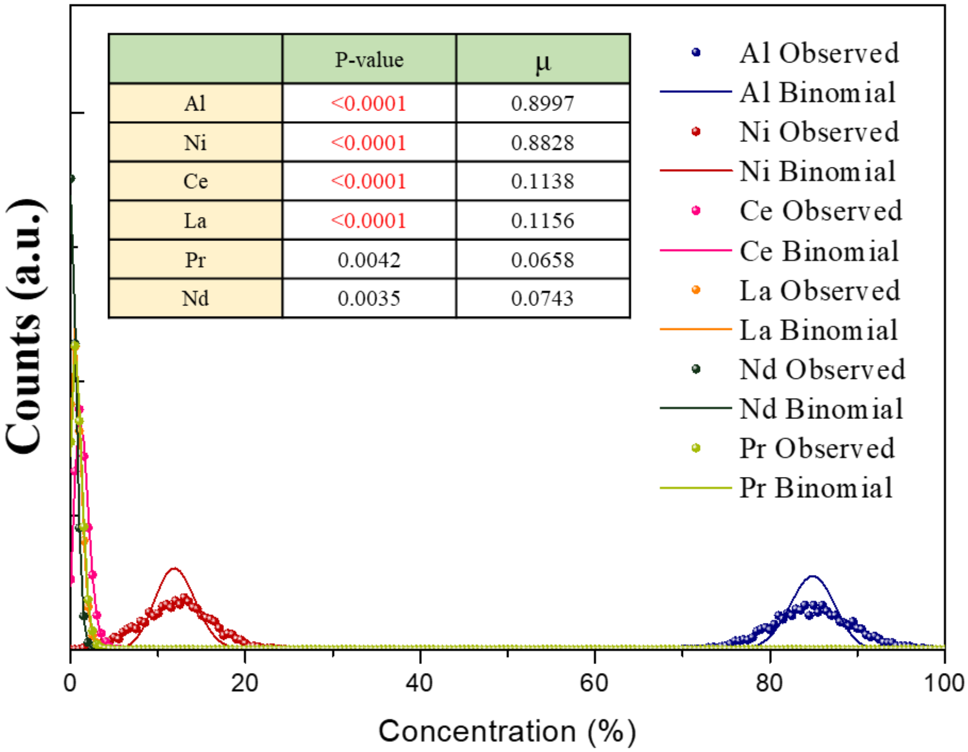

	P-value	μ
Al	<0.0001	0.8997
Ni	<0.0001	0.8828
Ce	<0.0001	0.1138
La	<0.0001	0.1156
Pr	0.0042	0.0658
Nd	0.0035	0.0743

Figure 4.18. Statistical binomial frequency distribution analysis results A bin size for frequency distributions is 0.5 at.%. The results of the binomial fit p-value and μ- parameters are listed in the inset tables.

4.6. Summary

In this chapter, crystallization behavior of FCC-Al in $Al_{90-x}Ni_{10}MM_x$ (x=2,4,6 at%) was carefully studied. As partial distribution function for MM2 and MM6 clearly determined, addition of MM can change the local atomic bonding nature (Al-RE bonding) of the system. changed atomic structures (MM2 → MM6) result in the enhanced glass stability with the higher T_x. Thus, MM2 and MM4 can possess the high number density of Al-MRO in their amorphous matrix, which can act as the nucleation site for the FCC-Al. In thermodynamic viewpoint, however, primary crystallization of FCC-Al in off-eutectic MM2 and MM4 is not favorable. But, by considering kinetical situation, it was confirmed that extended liquidus line of FCC-Al can stabilize the FCC-Al stable zone. Two different thermal-pathway (heating or cooling processes) for precipitation of FCC-Al in MM2 revealed that size and density of FCC-Al can be controlled separately. This means that the nucleation rate of FCC-Al is faster than the cooling rate induced by melt-spinning. Thus, to reveal the origin of the FCC-Al in as-spun MM2, it is required to investigate the transient incubation time for nucleation of FCC-Al.

Chapter 5.

Understanding of nucleation kinetics of FCC-Al

5.1. Introduction

For Al-TM-RE metallic glasses which follow the primary crystallization behavior, the nucleation kinetics of FCC-Al have attracted much attention due to their importance in the fundamental phase transformation. Nucleation of FCC-Al can be considered as the process that involves the formation of Al clusters (or embryos) that can evolve into nuclei when the critical free energy of clusters starts to have negative value. Like this, instead of direct and immediate crystallization of FCC-Al, the amorphous samples undergo a period of incubation time (or transient time) τ. Thus, the transient effect is crucial for understanding of the transformation behavior of Al-based metallic glasses. The incubation time also can provide the information for the glass formation ability of the alloys. In the case of bulk scaled glass formers such as Pb-, Zr-, Mg- based system, isothermal calorimetry study is conducted to measure the incubation time at the give temperature. However, exothermic signal from the growth of embedded clusters in Al marginal glasses limit the proper interpretation of the incubation time. Therefore, clear understanding about the incubation time for primary crystallization of FCC-Al is of importance for precise microstructure tuning of Al-based metallic glass.

In this chapter, based on the classical nucleation theory, nucleation incubation time of FCC-Al in MM2 and MM4 is measured by using FDSC. Through the direct measurement of incubation time of FCC-Al in MM2 and MM4, it is expected that one can solve the questions. (1) How can as-spun MM2 possess the FCC-Al but as-spun MM4 does not. (2) How can MM2 ribbon quenched with slower cooling rate has the higher number density of FCC-Al.

5.2. Fast heating calorimetry study for FCC-Al in Al-based metallic glasses

5.2.1. Hidden glass transition signal

Numerous works over the wide range of compositions have been conducted to understand the crystallization behavior and glass forming ability of Al-TM-RE systems [75,76]. However, most of these researches were induced within limited thermal condition measured by differential scanning calorimetry at the order of 0.1 K/s of heating rate. High number density of Al-MRO in amorphous matrix can be grown up by the diffused Al before the metallic glass transform into super cooled liquid. Early exothermal signal induced by the growth of embedded MRO overlap the endothermic heat flow from glass transition, So, conventional DSC cannot detect the clear glass transition phenomenon in the Al-based alloys with more than 86 at% Al [77,78]. To overcome this practical constraint, differential fast scanning calorimetry with scanning rates up to the order of 10^6 K/s was developed. Extreme fast heating rate of FDSC can increase the sensitivity of the thermal signal too. Therefore, in-situ exploration of the glass transition and crystallization behavior of Al-based MGs became possible [79].

Figure 5.1 is the FDSC results showing heat flow vs temperature at the heating rate of 3000 K/s. Unlike the conventional DSC, endothermic heat flow related with T_g are clearly detected, and their values are 481.5 K and 585.5 K for MM2 and MM4, respectively. T_x of MM2 and MM4 are 515.7 K and 635.4 K which are around 120 K higher than the temperature observed from conventional DSC ($T_{x,MM2}$ = 405.7 K, $T_{x,MM4}$ = 506.1 K). Figure 5.2 (a) is the graph that shows the T_g & T_p change depending on heating rate. Increasing T_g and T_x with the heating rate demonstrate that the glass transition and crystallization are of kinetic nature. Thus, temperature change of T_g and T_x follow the Kissinger equation:

$$\ln\left(\frac{\phi}{T_{onset}^2}\right) = -\frac{E_{act}}{R\,T_{onset}} + Const \qquad . \qquad \text{Eq. 5-1}$$

In here, ϕ is heating rate, T_{onset} is the value of the onset temperature (T_g or T_x) at the given heating rate, ϕ. E_{act} is the activation energy for glass transition or crystallization. R is the gas constant. The activation energy for glass transition and crystallization for MM2 and MM4 can be calculated via fitting the experimental results in figure 5.2(a) with the Kissinger equation. Fitting results are shown in figure 5.2(b). Calculated activation energy in MM2 for glass transition and crystallization is similar with each other (36.6 kJ/mol for glass transition and 37.4 kJ/mol for crystallization). In the case of MM4, activation energy for glass transition and crystallization are 72.3 kJ/mol and 98.2 kJ/mol, respectively. Typically, T_g requires higher activation energy than that of crystallization [80,81]. But the activation energy of glass transition and crystallization in MM2 is similar with each other. And the fitted value itself is also relatively lower than reference [60]. This means that glass stability of MM2 is relatively low and it is easy to be devitrified due to the high number density of Al-MRO.

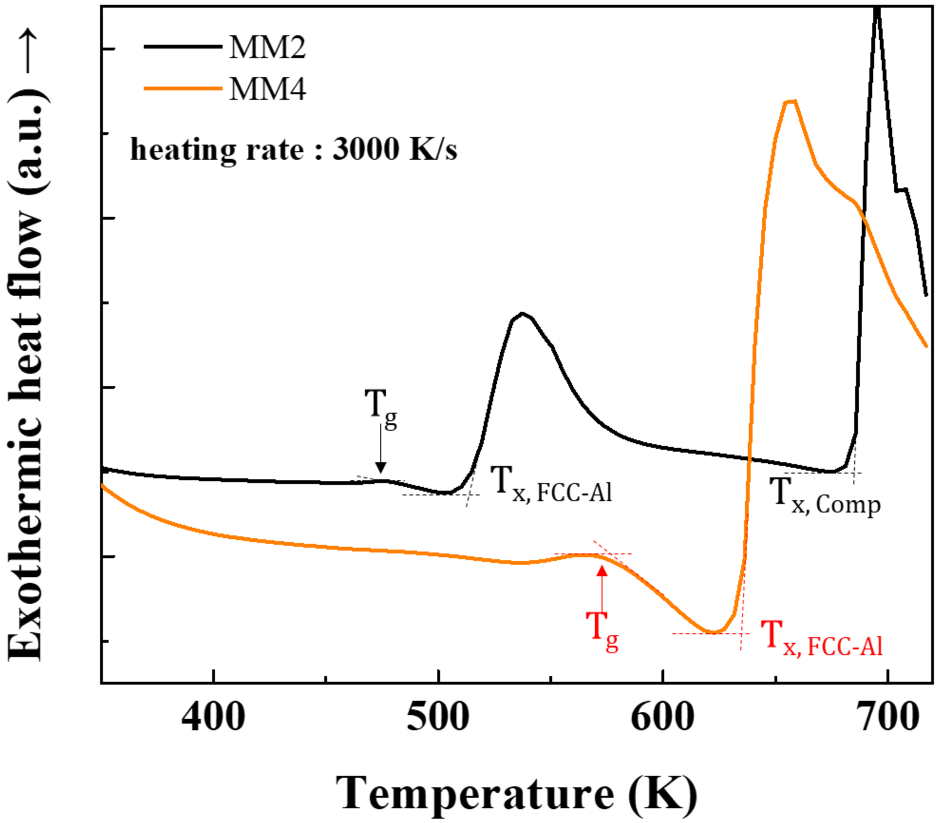

Figure 5.1. FDSC traces of MM2 and MM4, which were scanned with the heating rate of 3000 K/s

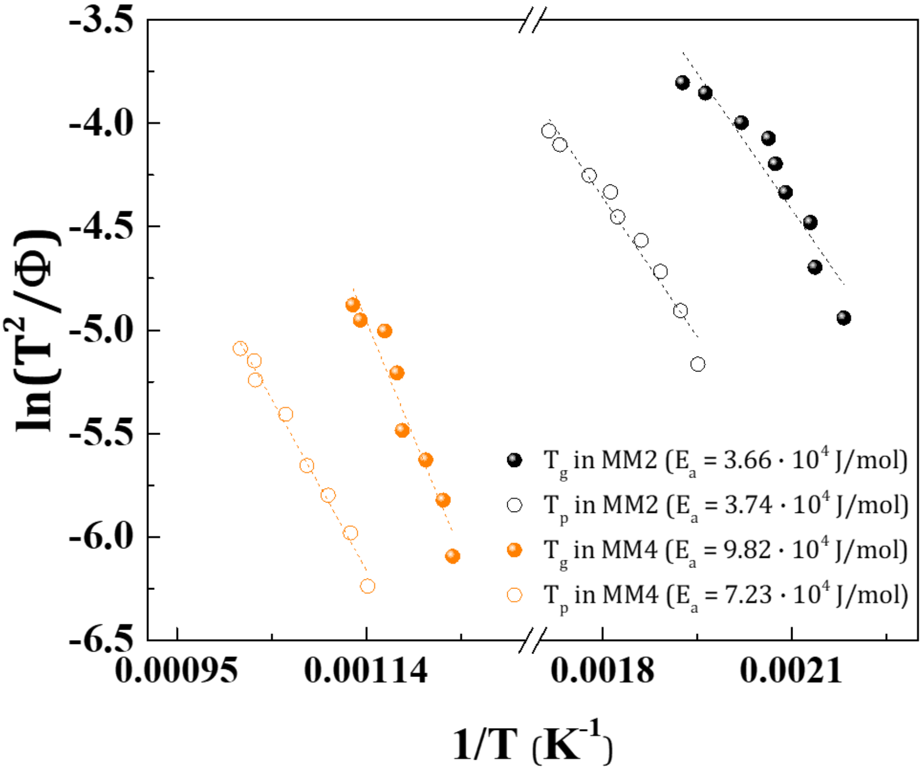

Figure 5.2. Kissinger plot results for glass transition and crystallization activation energy in MM2 and MM4

5.2.2. Modified VFT relation for diffusion behavior

According to references [82-86], the glass transition in cooling and heating processes is defined as:

$$\left\{\frac{1}{T}|\phi|\tau_R\right\}\Big|_{T=T_g} \cong 1 \qquad . \qquad \text{Eq. 5-2}$$

T is the temperatue, ϕ represents the heating rate, τ_R is the characteristic relaxation time. The glass transition on cooling or heating process can be determined by the relaxation time depending on the temperature. From this Arrhenius type of correlation, the conventional Bartenev-Ritland equation can be derived [83,84];

$$\frac{1}{T_g} = A - B\log|\phi| \qquad . \qquad \text{Eq. 5-3}$$

This equation can be expressed in the form of Vogel-Fulcher-Tammann correlation :

$$\frac{1}{(T_g - T_0)} = A_1 - B_1\log|\phi| \qquad . \qquad \text{Eq. 5-4}$$

Where T_0 is the Vogel temperature, A_1 and B_1 are constant. Equation 5-4 allows the accurate fit of T_g as shown in figure 5.3. The best fit to the experimental T_g data give us the fitted values of A_1, B_1 and T_0 as summarized in table 5.1.

During the crystallization in the continuous heating process, growth dominates at the peak temperature, T_p. Therefore, Kissinger plot of crystallization kinetics can be affected by the temperature dependence of the growth rate, U. Extension of the Kissinger plot toward the ultrafast heating rate provides more detailed information about the behavior of the undercooled liquid in wider temperature range. The temperature-dependence of the growth rate can be defined by equation 4-15. For growth of FCC-Al governed by diffusion of solute elements at the interface of crystal/amorphous matrix is given by

$$\frac{D}{a} = C\eta(T)^{-\xi} = U_{kin} \quad . \qquad \text{Eq. 5-5}$$

Ediger et.al suggested that the decoupling can be described by the form of $D \propto \eta^{-\xi}$. ξ is the function of temperature in the entire range and expressed by [84]

$$\xi = \frac{1 - T_o/T}{1 - T_o/T_c} \quad . \qquad \text{Eq. 5-6}$$

T_d is the decoupling temperature (or it has the same physical meaning with T_c, the critical temperature) where the supercooled liquid with solid state can be divided. In metallic glasses, the diffusion behavior can be distinguished in two temperature regimes. First, in the liquid state, there is a transition from the dynamics of a high temperature state [88]. Far above the T_d, the dynamics of liquid flow is not homogeneous due to the coherent motions of atoms, while single-atom translational motion is limited by the rigidity of the cages of surrounding particles. This state is often explained by a Vogel-Fulcher law. At a critical temperature, T_d, the dynamics of the supercooled melt changes from the homogeneous viscous flow to the pseudoarrested low-temperature flow. Second, when the liquid cooling below T_d, the liquid like diffusion is predicted to freeze in and diffusion follows the classical Arrhenius law. At high temperature far above T_g, ξ is 1, and application of Stokes-Einstein relation is feasible [87].

The temperature dependence of η is unchanged at the decoupling interval located close to T_g. Then, η can be governed in the entire temperature range by the VFT-type equation;

$$\eta = \eta_0 \cdot \exp\left(\frac{2.3}{B_1(T-T_0)}\right) \quad . \qquad \text{Eq. 5-7}$$

From the discussions and definitions above, the diffusion coefficient can be defined differently above and below T_d as:

$$D = \begin{cases} D_\eta = D_0 \cdot \exp\left(-\frac{2.3}{B_1(T-T_0)}\right) \; (for\, T \geq T_d) \\ D_\eta^{-\xi} = D_0 \cdot \exp^{-\xi}\left(-\frac{2.3}{B_1(T-T_0)}\right) \; (for\, T \leq T_d) \end{cases} \quad . \qquad \text{Eq. 5-8}$$

Figure 5.4 exhibits the obtained $\ln(U_{kin})$ curves with Kissinger-type plot. The best fit to the experimental data yields T_d = 436.24±3.1 K for MM2 and 488.23±2.1 for MM4, respectively. Figure 5.5 shows the Arrhenius graph of the diffusivity of MM2 and MM4 over a temperature range covering from super-cooled liquid region to solid state region. D_0 is a kinetic pre-factor and has no direct significance, because the absolute value cannot be determined.

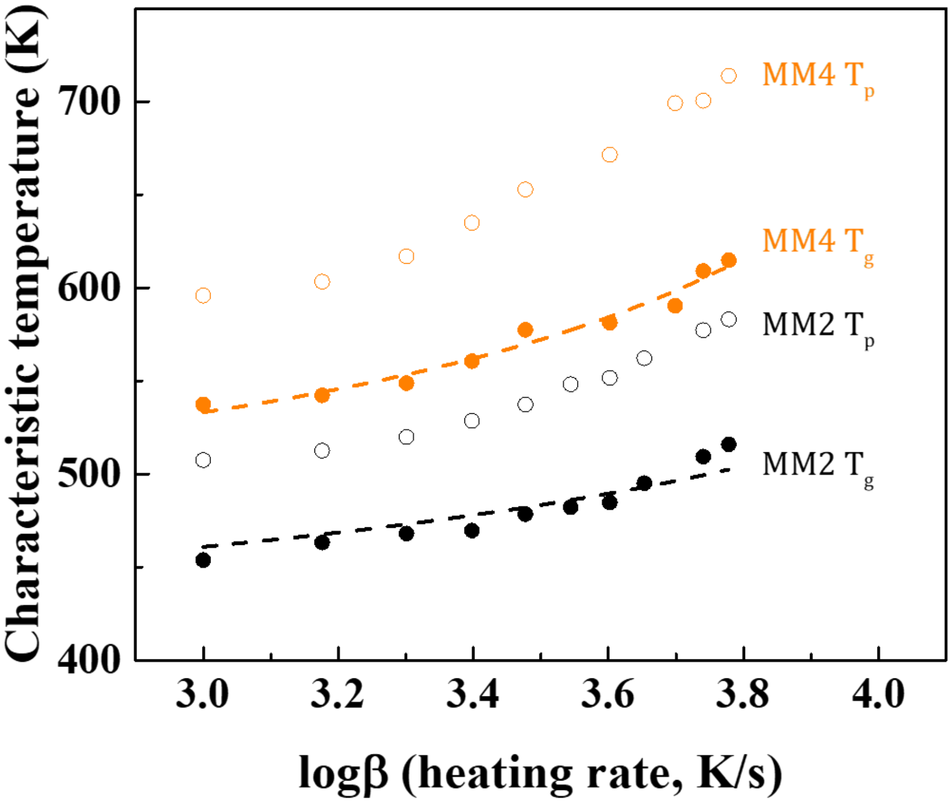

Figure 5.3. T_g and T_p of MM2 and MM4 as a function of heating rates

	T_g (3000 K/s)	T_o	A_1	B_1	T_D
MM2	481.5	381.11	0.029	0.0055	436.24±3.1
MM4	515.7	436.48	0.028	0.0059	488.23±2.1

Table 5.1. Summary of best fit results from modified VFT equation

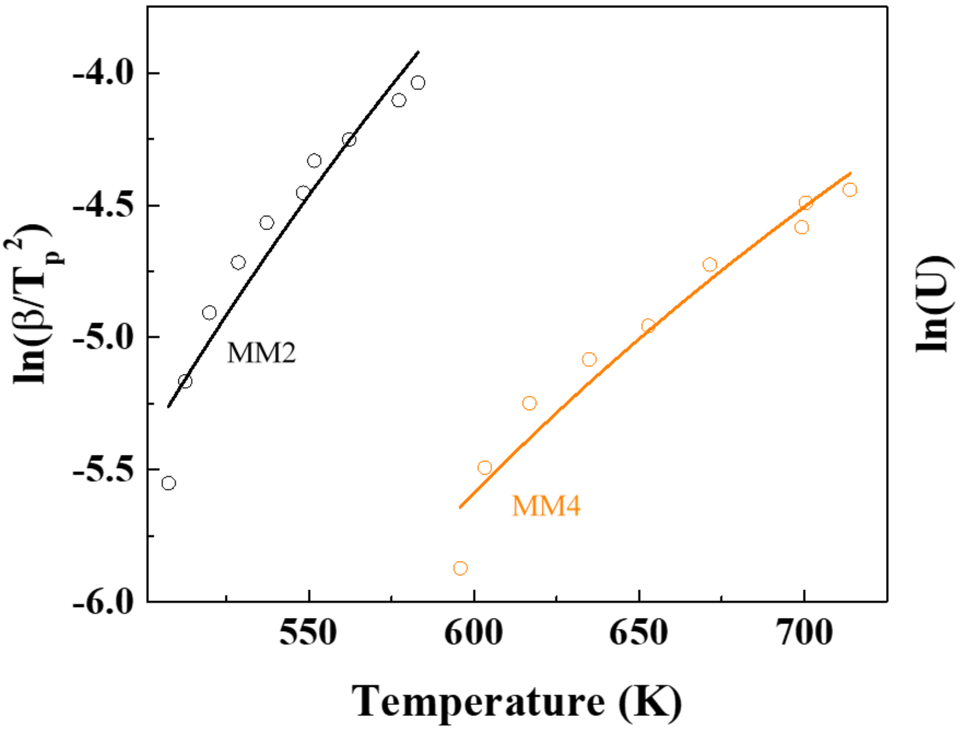

Figure 5.4. Kissinger plot with the normalized growth rate of FCC-Al in MM2 and MM4

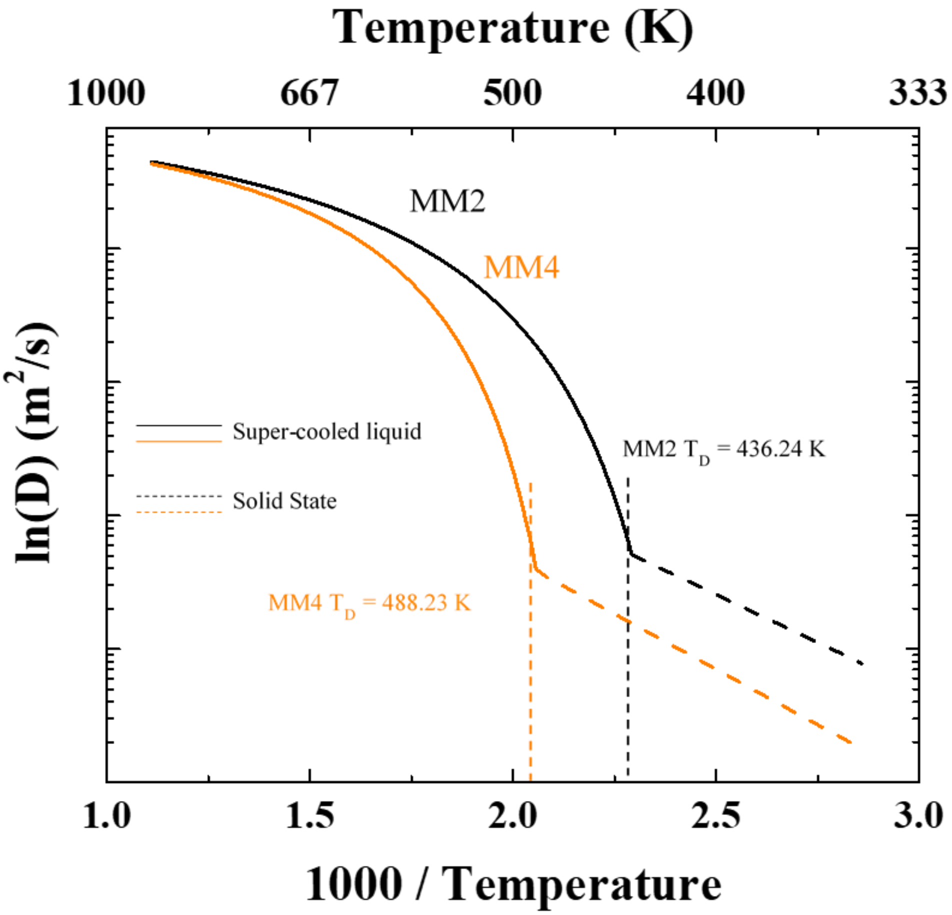

Figure 5.5. Diffusion kinetics of MM2 and MM4

5.3. Experimental study of nucleation kinetics

5.3.1. Measurement of nucleation incubation time

Transient incubation time (τ) for nucleation is the time that is required to promote the nucleation in a system. It defines the duration time for the onset of the steady-state distribution and demonstration of the nucleation rate $I(t)$, towards to the steady state $I_{SS}(t)$ [89]. Incubation time, τ, also has a relation with the random walk zone, Δ, because clusters needs some time to diffuse through the random walk zone. Most of all, prediction of incubation time can give us the direct insight related with the glass forming ability of the glassy alloys. Typically, isothermal test below T_g is the common method for detecting the beginning time for crystallization [90,91]. However, for some Al-based marginal MGs with poor GFA, the signal from the primary crystallization is so weak that the crystallization peak in the isothermal annealing is hard to detect [92]. In addition, as shown in figure 5.6, growth signal from embedded Al cluster accelerates early exothermic onset before reaching to the annealing temperature. It was considered that the direct TEM analysis is the only method for transient incubation time and nucleation rate. Through the TEM images of annealed samples, it is possible to evaluate the transient incubation time by plotting the crystal's number density and annealing conditions [93]. However, TEM analysis of Al-based MGs with nanocrystals is too difficult, and time-consuming technique. MD simulation is also effective way to calculate the incubation time and steady state nucleation rate [94]. But it is difficult to get the exact simulation results on multicomponent system more than 3 elements.

Recently, Y.Shen et. al. [95] proposed new technique for monitoring of incubation time based on the relaxation effect induced by annealing. Figure 5.7 is the schematic image explaining how incubation time can be obtained. Under the isothermal condition, structural relaxation can evolve the T_g with the annealing time (Stage 0 → Stage I). Up to now, no clear crystalline phases can be detected as shown in XRD. After the nucleation of primary FCC-Al, due to the limited solubility of Ni and RE, solute enriched area with their thickness about 3 nm can occur around the FCC-Al [56], hence further increase of T_g. Consequently, the break point in the trend of T_g change induced by structural relaxation and compositional fluctuation should coincide with the incubation time for primary crystallization. This measurement requires clear observation of T_g.

Figure 5.8(a) is the thermal segment for incubation time measurement. As-spun MM2 is heated up to 403 K (=130 °C) with the 40000 K/s and holds for 750 and 1500 seconds, respectively. Just after the pre-annealing, T_g and T_x was scanned with the heating rate of 3000 K/s. Figure 5.8(b) is the FDSC traces which are T_g and T_x marked on it. One can see that T_g and T_x are increased with the pre-annealing time. A series of pre-annealing & scanning tests was performed in 403 K (=130 °C) of annealing temperature, and collection of T_g and T_x are summarized in figure 5.7. With the increased annealing time, T_g and T_x are shifted to higher temperature. The change of T_g shows the clear inflection point at 950 seconds. Interestingly, one can see that the inflection tendency of T_x is exactly same with that of T_g. To confirm the validity of the results in figure 5.7, pre-annealing & scanning test is performed again at the annealing temperature of 423 K (=150 °C). Like the results of figure 5.9, break point of T_g and T_x in figure 5.10(a) place at the 10 seconds together. This indicates that the incubation time for nucleation at 423 K (=150 °C) is 10 seconds. Figure 5.10(b) is the XRD data of the samples which are isothermally annealed at 423 K (=150 °C) for 5 and 15 seconds. From XRD results, at 150 °C, the sample annealed for 5 second only shows the diffused pattern that is same with the figure 4.3 (a). In contrast, for the sample annealed for 15 seconds beyond the incubation time (=10 seconds) diffused peak related with the FCC-Al. These results confirm that the value of incubation time measured by the FDSC pre-annealing & scanning is proper. In contrast with T_g, metastable amorphous phases always show T_x in continuous heating. Thus, utilizing of T_x for pre-annealing & scanning method for the incubation time is promising way for measuring the incubation time even with commercial DSC with moderate heating rate.

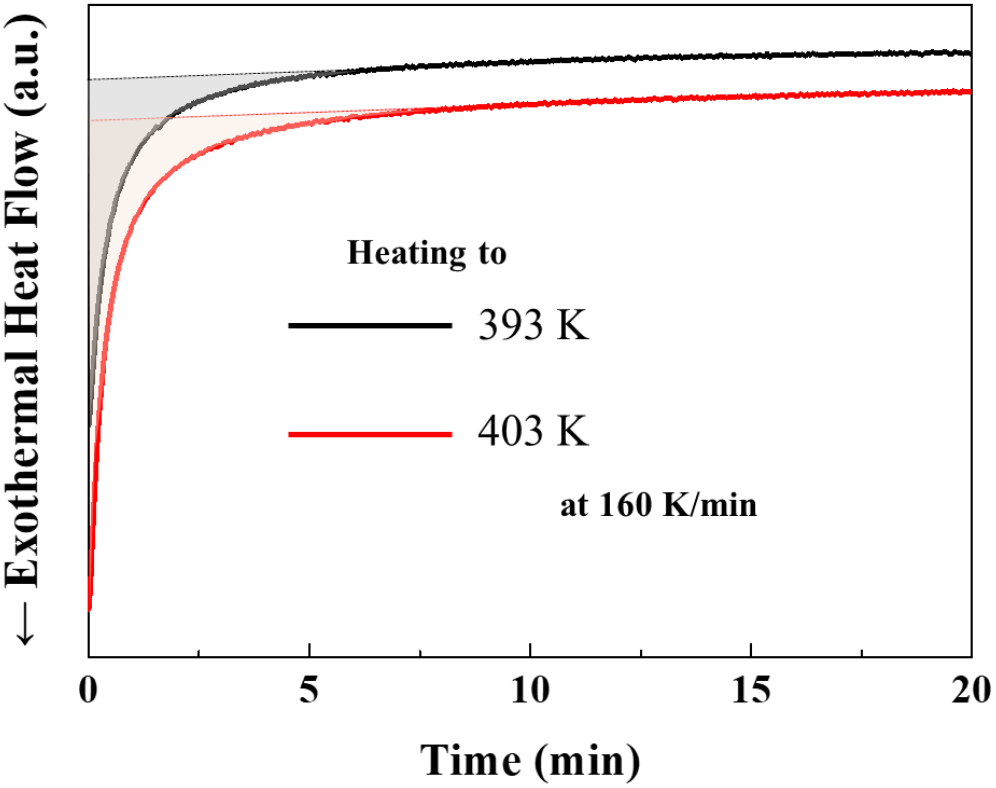

Figure 5.6. Isothermal heat flow of MM2 measured from conventional DSC

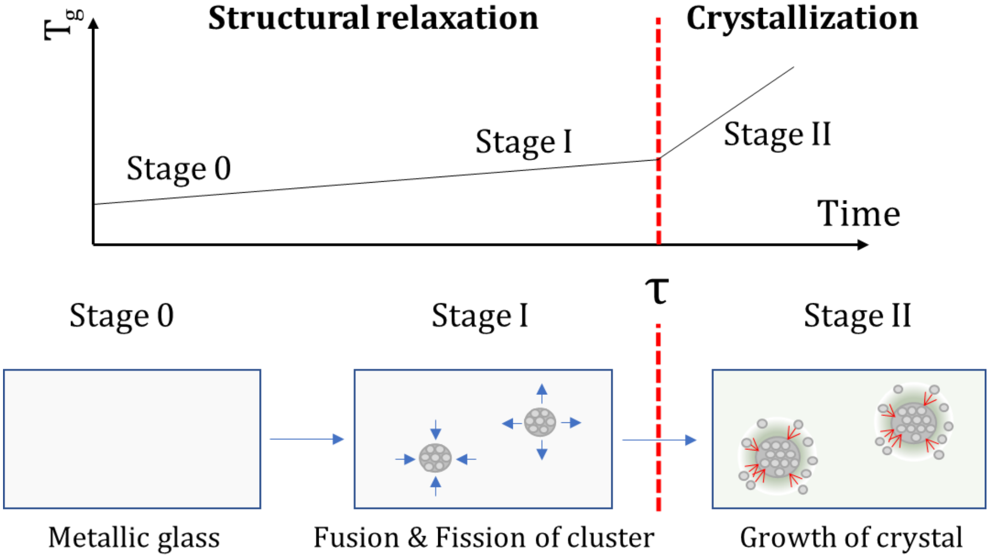

Figure 5.7. Schematic illustration showing how to measure the incubation time via FDSC

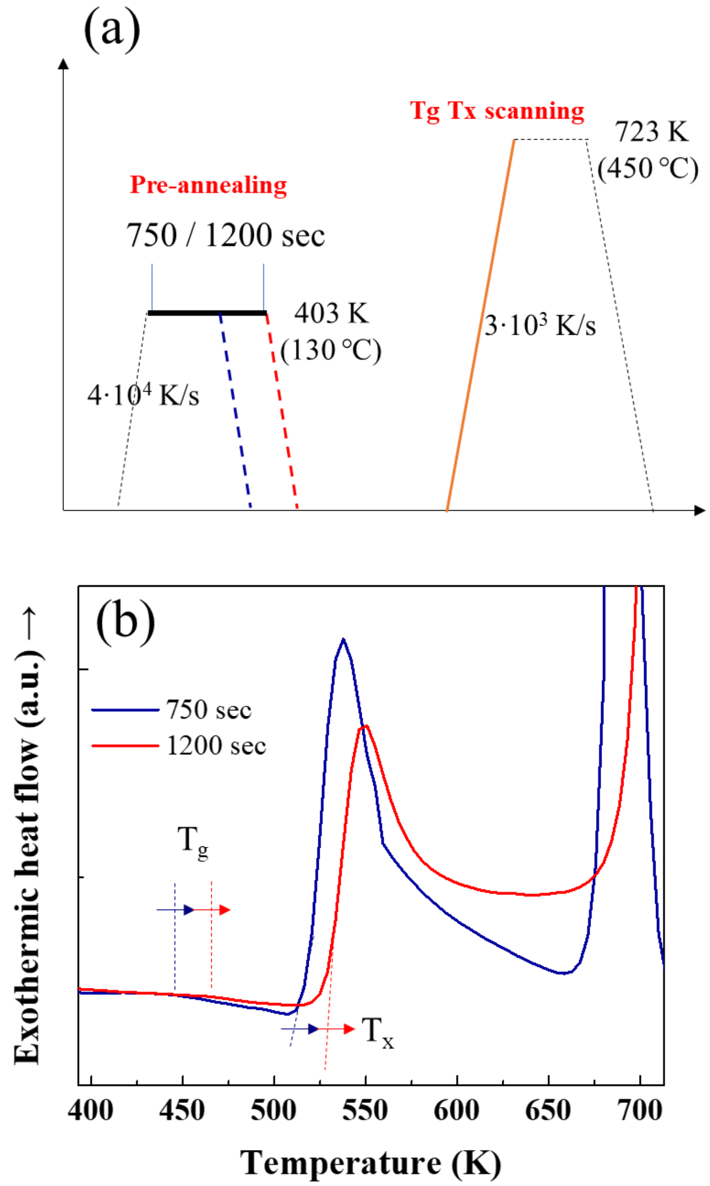

Figure 5.8. (a) Pre-annealing & scanning thermal segment for incubation time measurement and (b) FDSC results showing shift of traces induced by pre-annealing.

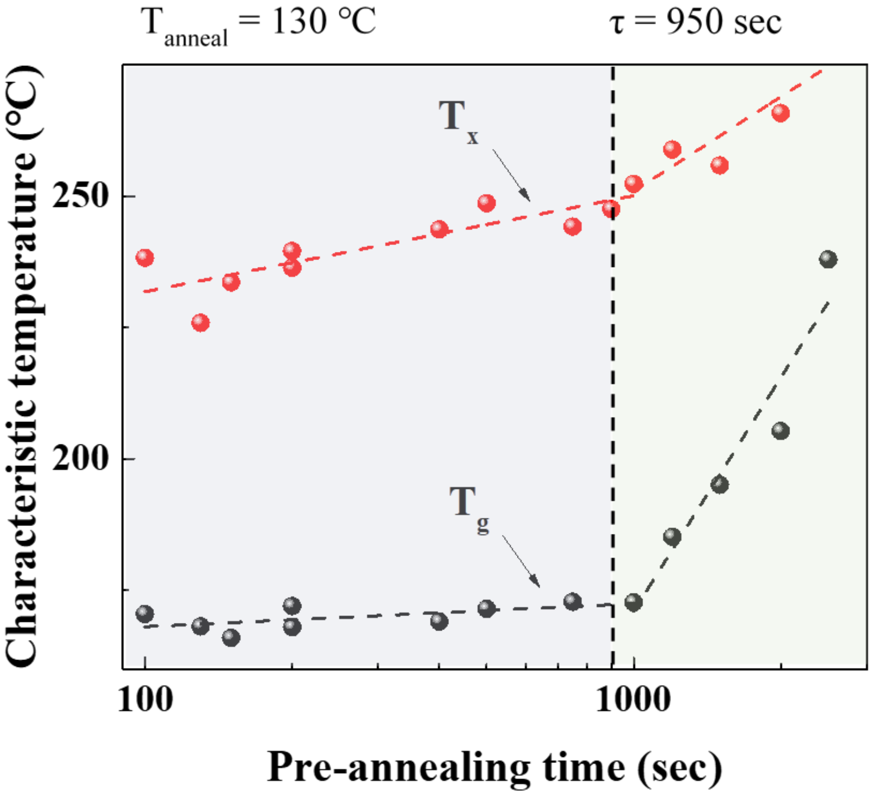

Figure 5.9. Diagram showing the T_g and T_x change depending on the pre-annealing time (annealing at 130 °C). Deflection point (dashed line) represent the incubation time for nucleation of FCC-Al

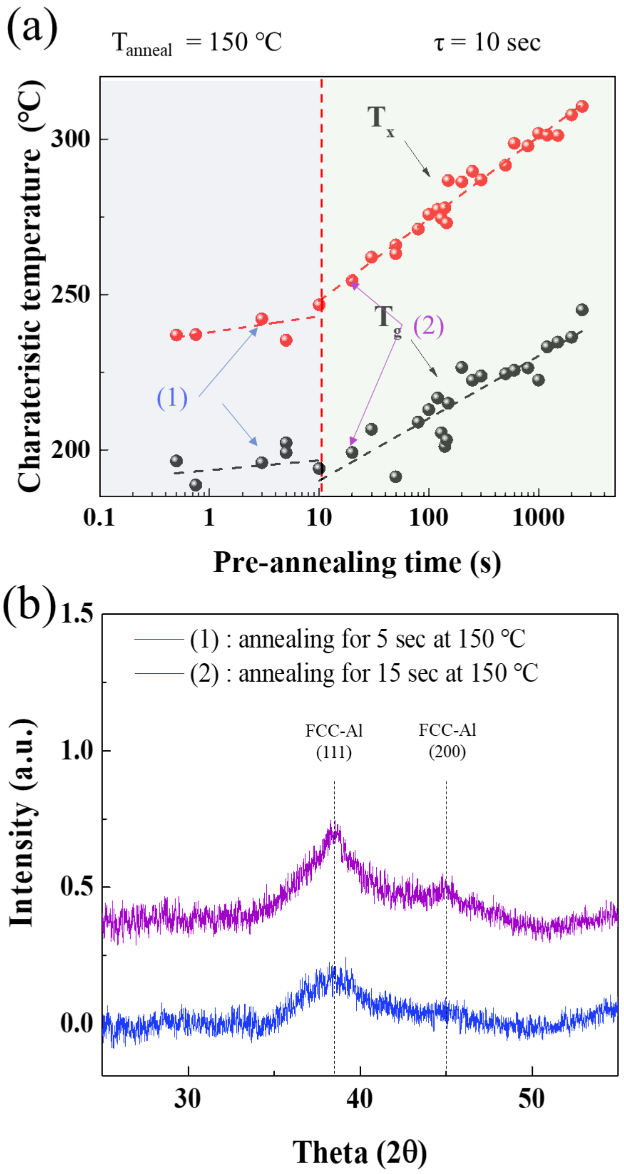

Figure 5.10. (a) Diagram showing the T_g and T_x change depending on the pre-annealing time (annealing at 150 °C). Deflection point at 10 seconds means incubation time at 150 °C. (b) XRD results of the sampled annealing at 150 °C for 5 seconds and 15 seconds.

5.3.2. Evaluation of TTT curves with thermophysical parameters

Incubation time corresponds to the inverse of nucleation rate for the certain piece of volume of melt [96]. This means that combination of incubation time at various temperature range can draw the TTT (time-temperature-transformation) curve of FCC-Al. By using the pre-annealing & scanning method, incubation time of FCC-Al in MM2 and MM4 is observed for various temperature range.

Figure 5.11 shows the representative break point results of MM2 for the other three annealing temperature, 140 °C, 160 °C and 180 °C. Interestingly, in contrast with 413 K (figure 5.11 (a)) and 433 K (figure 5.11(b)), there is no clear deflection of T_g in 453 K (figure 5.11(c)). From the certain temperature, the degree of structural relaxation becomes saturated, and relaxation effect on T_g change also become weak. Thus, T_g does not work as the incubation parameter from the certain annealing temperature. Representative break point results obtained from MM4 is summarized in figure 5.12. MM4 is more stable glass than MM2. Regardless of the annealing temperature, deflection of T_g in MM4 is clearly observed. 240 °C results shows the clear inflection and saturation point of T_g, T_x at 8 second and 100 second, respectively. Slow diffusion of RE elements limits the growth of FCC-Al and volume fraction become saturated [72, 96] The limited growth kinetics is the reason saturation of T_g and T_x occurred at 240 °C in MM4.

As shown in figure 5.13, collected incubation times of MM2 and MM4 is resulted in the nose shaped curvature which signify the TTT curve of FCC-Al. To conclude the suitability of this TTT diagram, a measurement-based calculation was developed to calculate TTT curves by fitting the measured incubation time. One of the commonly used approach for TTT curve calculation is the Uhlmann's equation for volume fraction X [79,80]:

$$X \approx \frac{1}{3}\pi J_v U^3 \tau^4 \qquad . \qquad \text{Eq. 5-5}$$

Here, J_v is the nucleation frequency per unit volume and U is the growth rate τ is time. For glass formation, X should be negligible value ($X = 10^{-6}$). Because of the influence of the viscosity on the crystallization around T_g of undercooled liquid, relation of viscosity and temperature, which is the parameter of the growth rate, is uncertain. This thermophysical limitation hinders the calculation of growth rate and proper application of above equation [61].

Simply, onset of crystallization can be defined as when the stochastic nucleation events occur within a volume V at a given temperature after a time τ by

$$I_{SS} V \tau = 1 \qquad . \qquad \text{Eq. 5-6}$$

By Inserting the equation 4-14 and 4-15 in 5-6, the onset time for nucleation (= incubation time, τ) can be expressed as :

$$\ln(\tau) = \Gamma + \frac{B}{T - T_0} - \ln T + \frac{C}{T \Delta G_v^2} \qquad . \qquad \text{Eq. 5-7}$$

Where, T_0 is the extrapolation temperature of T_g at infinitely low cooling rates which has the same definition of T_0 in equation 3-4. B is a constant of the order 10^3K that can be adapted for wide range of glass formers. C is the variation given by $C = (16\pi/3k)\sigma^3 f(\theta)$, and Prefactor Γ is expressed as $\Gamma = \ln(3\pi a^3 \eta_0/$

$\rho_s V k)$. The onset time and temperature in figure 5.10 were used in equation 5-7 and the assessed TTT diagram is plotted over the experimental results. The fitted parameter values are also displayed together. It is evident that best fit of TTT is well matched with the experimental points.

Nose point (time, temperature) in MM2 and MM4 is (0.12 sec, 433 K) and (6.5 sec, 506 K), respectively. As-spun MM2 contains a few percent of nanocrystals. Effective cooling rate of melt spinning process is calculated by using the equation below [98]:

$$(\frac{\delta T}{\delta t})_{\chi} = -\frac{b_{wheel}(T_{Al.liquid}-T_{wheel})\chi}{2(b_{Al}+b_{wheel})t\sqrt{\pi\alpha_{Al}t}} \exp\left[-\frac{\chi}{2\sqrt{\alpha_{Al}t}}\right]^2 \quad . \qquad \text{Eq. 5-8}$$

In here, α_i and b_i is thermal conductivity and thermal storage coefficient of i, respectively. T_i is the initial temperature of i. χ is thickness of the as-spun ribbon. For the smooth calculation , it is assumed that wheel is pure copper and thermal property values of alloys ($Al_{90-x}N_{10}MM$) is taken from pure Al. Detailed values and units are listed in table 5.2. Blue and green dashed line in figure 5.13 is the calculated effective cooling rate for MM2 and 45μm MM2. Both of cooling rate passes the TTT curve of FCC-Al. The primary precipitate phase from the MM2 is the stable FCC-Al that can be precipitated even from melt spinning processes. Without obvious growth of FCC-Al, slower quench rate can arouse the higher number density of FCC-Al (chapter 4.5.2).

Homogeneous nucleation also can be expressed in the form of below equation.

$$I_{ss}^{hom} = \omega C_0 \exp\left(-\frac{\Delta G_m}{kT}\right)\exp\left(-\frac{\Delta G^*}{kT}\right) \quad . \qquad \text{Eq. 5-9}$$

Figure 5.14 shows the two exponential terms in equation 5-9; $\exp(-\Delta G^*/kT)$ is essentially the potential concentration of nuclei and the value is zero until a critical undercooling, ΔT_c is reached, after which it rises very rapidly. The other term, $\exp(-\Delta G_m/kT)$ is the atomic mobility. Since ΔG_m is constant, the value of this exponential term decreases rapidly with decreasing temperature. Note that at undercoolings smaller than ΔT_c, nucleation rate is zero because the driving force is too small, whereas at very high undercoolings nucleation rate is also negligible because diffusion is too slow. Simply saying, the growth of crystal can be limited due to the low migration rate of elements, but the undercooling can yield more nucleation of crystals.

Below the C nose, atomic migration term is dominant factor for nucleation and diffusion rate is limited. Thus, the isothermal annealing at below 433 K will yield the smaller size of FCC-Al than that of non-isothermal annealing. Figure 5.15 is the in-situ SAXS results obtained from the 403 K isothermal test of MM2. Samples was heated at 403 K. Every dashed line are SAXS curves taken every 2 minutes. From 0 min to 20min, position of maxima parabolically decreased with time and saturated after 20 minutes. Position of saturated SAXS curve is perfectly matched with the SAXS obtained at 435 K curve in figure 4.11.

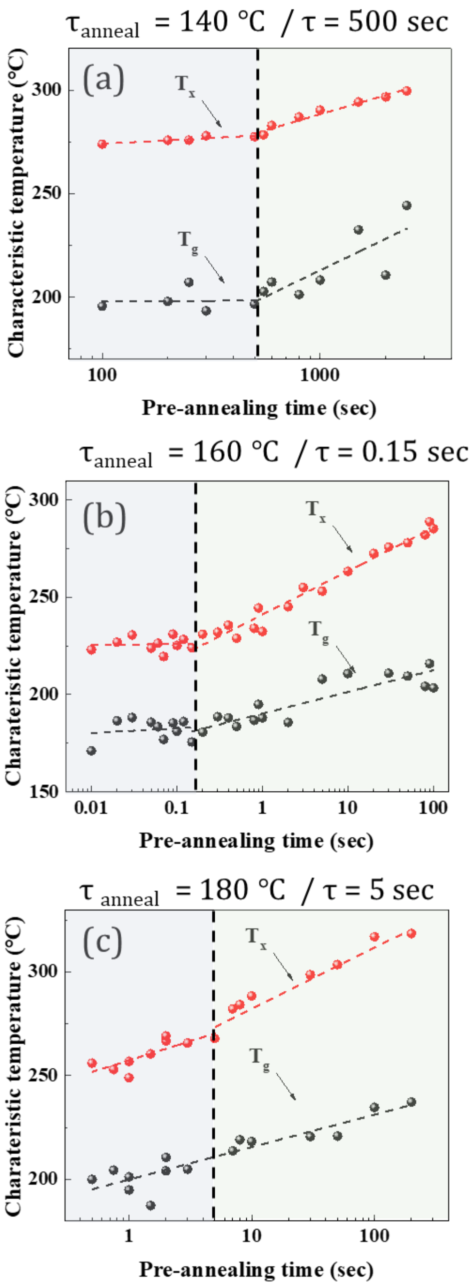

Figure 5.11. Representative pre-annealing & scanning results of MM2 conducted at annealing temperature of (a) 140 °C, (b) 160 °C and (c) 180 °C

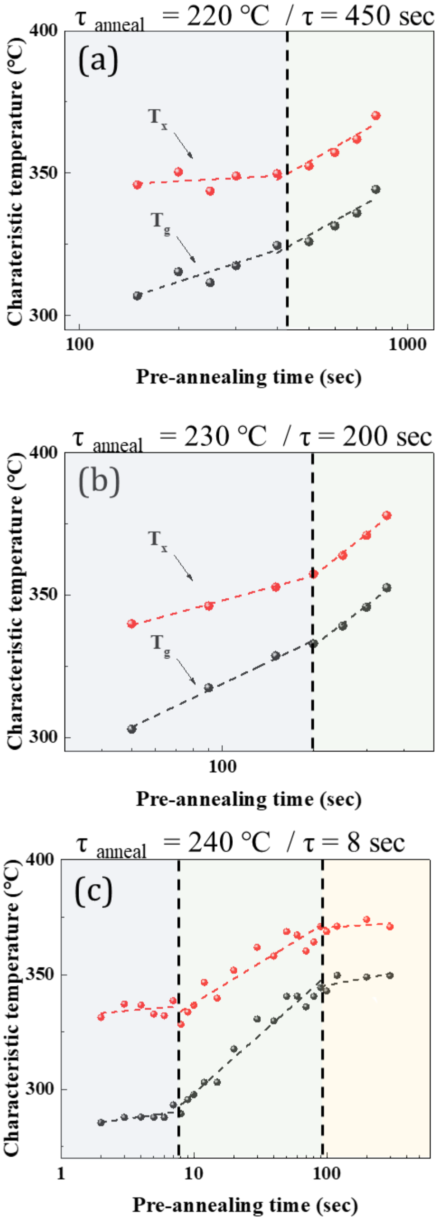

Figure 5.12. Representative pre-annealing & scanning results of MM4 conducted at annealing temperature of (a) 220 °C, (b) 230 °C and (c) 240 °C

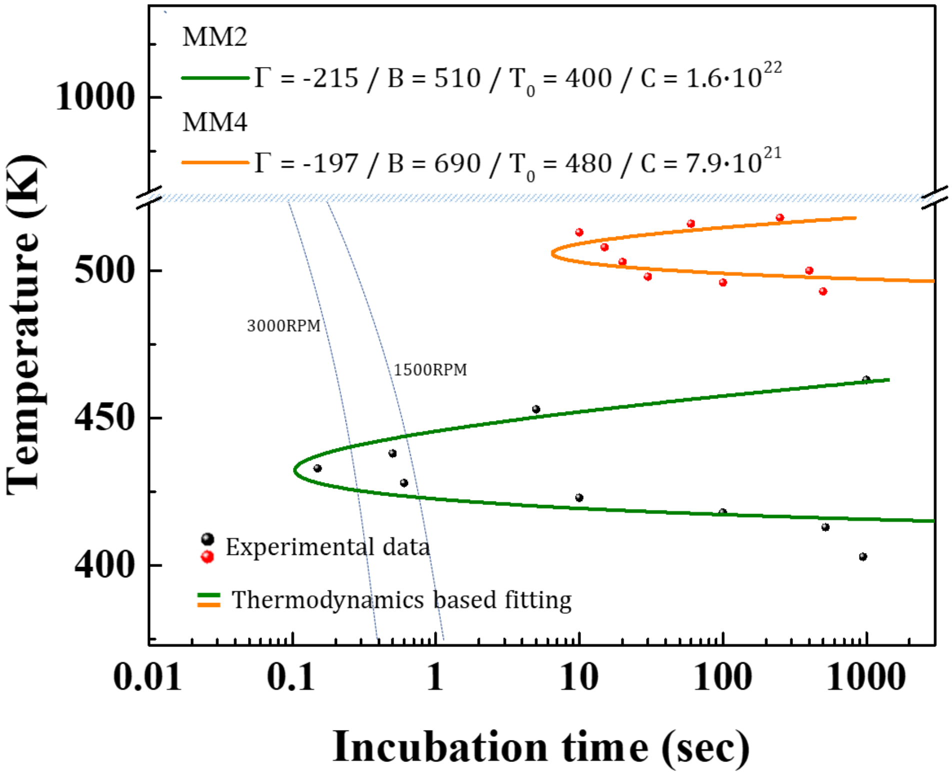

Figure 5.13. TTT diagram of FCC-Al in MM2 and MM4

‘

Parameter	Meaning	Al	Cu Wheel
Ti	Initial T (K)	1300 <	300
α	Thermal Conductivity (W/mk)	237	398
b	Thermal storage coefficient (WS$^{0.5}$/m^{2}K)	23730	37039
χ	Thickness (µm)	20 – 40	

Table 5.2. Modeling parameters and their values to estimate the cooling rate of melt-spun MM2

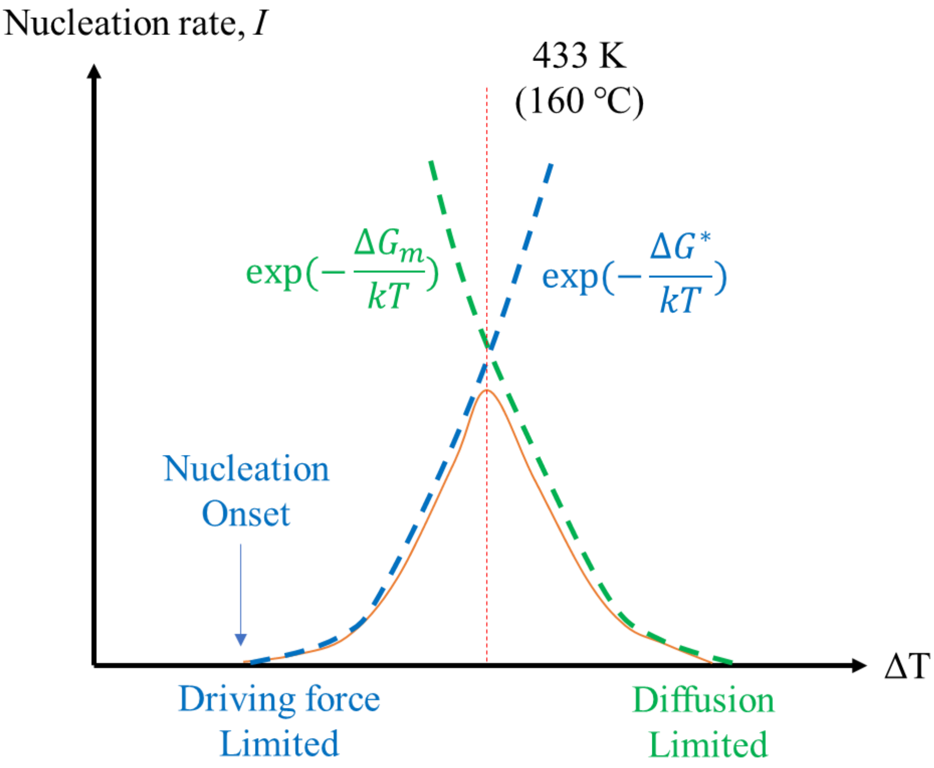

Figure 5.14. Schematic image explaining the two exponent terms that determines the nucleation rate of FCC-Al in MM2.

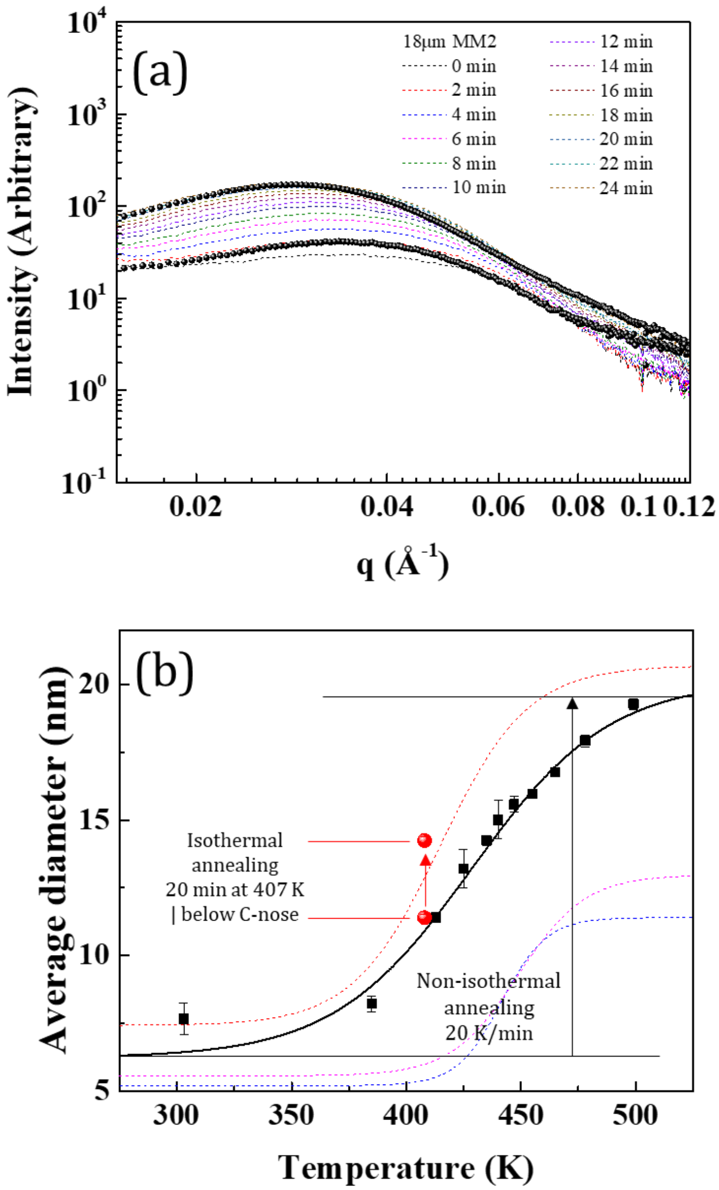

Figure 5.15. (a) Isothermal in-situ SAXS data of MM2 at annealing temperature 407 K (= 130 °C) below the C-nose (160 °C) and (b) calculated average diameter in the annealing condition of 1)non-isothermal annealing with the heating rate of 20 K/min and 2)isothermal annealing at 407 K (= 130 °C)

5.4. Summary

Up to now, due to the limited GFA and Al-MRO of the Al-based MGs, direct investigation of nucleation kinetics has been limited. Owing to the ultrafast FDSC, precise glass transition behavior, which give us the detailed information about the relaxation and diffusion behavior, can be observed. And through the T_g and T_x changes as a function of the pre-annealing time, it was possible to observe the incubation time of nucleation of FCC-Al. By collecting the incubation time at the wide range of annealing temperature, TTT diagram of FCC-Al in MM2 and MM4 was also obtained. This is the first reports for TTT diagram results in Al-based marginal glass system. Combination of effective cooling rate of melt-spinning process with TTT diagram clearly revealed that the nucleation of FCC-Al in MM2 is much faster than the melt-spinning cooling rate, and this is the reason why the cooling process is adaptable for the MM2. Consequently, it is expected that this novel kinetic analysis method can be applied to not only the Al-based metallic glasses but also the various systems with poor GFA.

Chapter 6.

Mechanical responses of $Al_{90-x}Ni_{10}MM_x$ MG

6.1. Introduction

Metallic glasses are known to have unique mechanical properties including high strength, relatively low elastic modulus and perfect elastic behavior [99]. However, due to the lack of deformation mechanism, MGs show no tensile plasticity and catastrophically fail. [100,101]. This quasi-brittle deformation manner governed by localized shear banding is the one of the main factors that barrier the use of metallic glasses in structural application.

Macro scale redistribution of shear bands can enhance the toughness of MGs by prohibiting the shear banding propagation [102]. And in a microscopic scale, accelerated activation of shear transformation zone (STZ), which represents a localized atomic arrangement, also can induce the easy nucleation of shear bands [103,104]. Al-TM-RE MGs are famous ductile glassy system which has been deeply studied to uncover the topological packing state of MGs [16]. Primary crystallization of FCC-Al in Al-TM-RE MGs is also a desirable factor for improving the mechanical properties. Despite such an achievement related to the atomic / micro level structural design, their relations with the mechanical responses remain poorly understood. As summarized in figure 6.1, atomic structure variation and microstructure of $Al_{90-x}Ni_{10}MM_x$ system was systematically studied in 3 ways : (1) Atomic structure tuning via MM addition (2) Heating process for FCC-Al crystallization in MM2 and (3) cooling process for limited size MM2. These three processes are based on the comprehensive understanding about phase stability of glasses and nucleation kinetics of FCC-Al. Thus, $Al_{90-x}Ni_{10}MM_x$ MGs can be used as a model material for exploring the effect of atomic / micro structural variation on mechanical properties. In this chapter, to give the profound understanding about mechanical responses of Al-based MGs, nano-scaled and micro-scaled mechanical test was performed.

6.2. Nano-scaled deformation of Al-based metallic glasses.

6.2.1. Nanohardness

To extend the understandings about the influence of (1) the atomic structural variation induced by compositional changes and (2) the micro structural variation introduced by FCC-Al nanocrystals on the mechanical dynamics, nanoindentation test was conducted. Figure 6.2(a) shows load-displacement curves exhibiting the pop-in behavior. Table 6.1 is the summary of the average value of hardness (*H*), reduced elastic modulus (E_r) and yield stress (σ_y) of MM2, MM4 and MM6. For the observation of σ_y, we approximated the maximum shear stress from the first pop-in of load-displacement curve. Figure 6.2(b)-(d) is the representative load-displacement curves showing the first pop-in of each sample. The initial portion up to a first pop-in corresponds to elastic deformation, as given by the Hertzian elastic contact solution which is defined as [105]

$$p = \frac{4}{3} E_r R_{con}^{0.5} h^{1.5} \quad . \qquad \text{Eq. 6-1}$$

Here, p is the applied load by the indentation tip, h is the displacement, R_{con} is the tip radius and E_r is the value reduced elastic modulus. From the very first pop-in, which is showing the first deviation between the Hertzian solution and loading curve, the σ_y that leads to the initiation of the first shear band can be evaluated by [106].

$$\sigma_y = 0.31 (\frac{6E_r^2}{\pi^3 R^2} p)^{1/3} \quad . \qquad \text{Eq. 6-2}$$

MM ($Ce_{50.19}La_{25.31}Nd_{19.5}Pr_{4.99}$) is the relatively large atom (ε_{Ce} : 1.82 Å, ε_{La} : 1.82 Å, ε_{Nd} : 1.82 Å) with the lower electronegativities (φCe : 1.12, φLa : 1.11, φNd : 1.14) than that of Aluminum (ε: 1.43 Å, φ: 1.61). Thus, addition of more MM accounts for the atomic bonding nature (Al-RE bonding) with high W_{Al-RE}, and results in the enhancement of H, E_r and σ_y of as-spun samples. As shown in chapter 4, initial transformation upon devitrification for MM2 is the primary nanocrystallization of FCC-Al. Such microstructures can be classified as a nanophase composite and is clearly responsible for the unprecedented high strength. But, along with the as-spun state, studies related to the mechanical behaviors were only limited to the basic mechanical properties. By comparison of the mechanical dynamics of as-spun MM2, MM4 and MM6, we could be deeply comprehended the deformation behaviors of MM2 with FCC-Al nanocrystals. Figure 6.3 shows the hardness changes as a function of V_f of precipitated FCC-Al. For the experimental continuity, annealing conditions for hardness test were same as the in-situ SAXS test in chapter 4.3.1. From room temperature (V_f = 5 %) to 455 K (V_f = 30 %), hardness increases proportionally to annealing temperature. After 465 K (V_f = 45 %), annealed MM2 loses their ductility and the value of hardness is saturated. Because of the low solubility of Ni and RE elements in Al, Ni and MM elements are isolated around FCC-Al after the annealing process. [109] Approximate compositions of the solute enriched area around the FCC-Al is calculated in chapter 4

Figure 6.4 is the nanoindentation results of as-spun MM2 with different thickness. And the average hardness, reduced elastic modulus and yield strength are denoted in table 6.1. From as-spun MM2 with 18μm thickness (V_f = 5%) to 45μm MM2 (V_f = 35%), hardness value increases from 3.51 to 4.09 GPa. 35 % of V_f can be achieved by annealing up to 455 K. hardness of 455 K MM2 is 4.5 GPa much higher than that of 45μm MM2. Due to the structural relaxation and thicker solute enriched area, even though 45μm MM2 shows the same volume fraction with 455K MM, hardness of annealed sample (heating process) are higher than that of thicker samples (cooling rate controlled process)

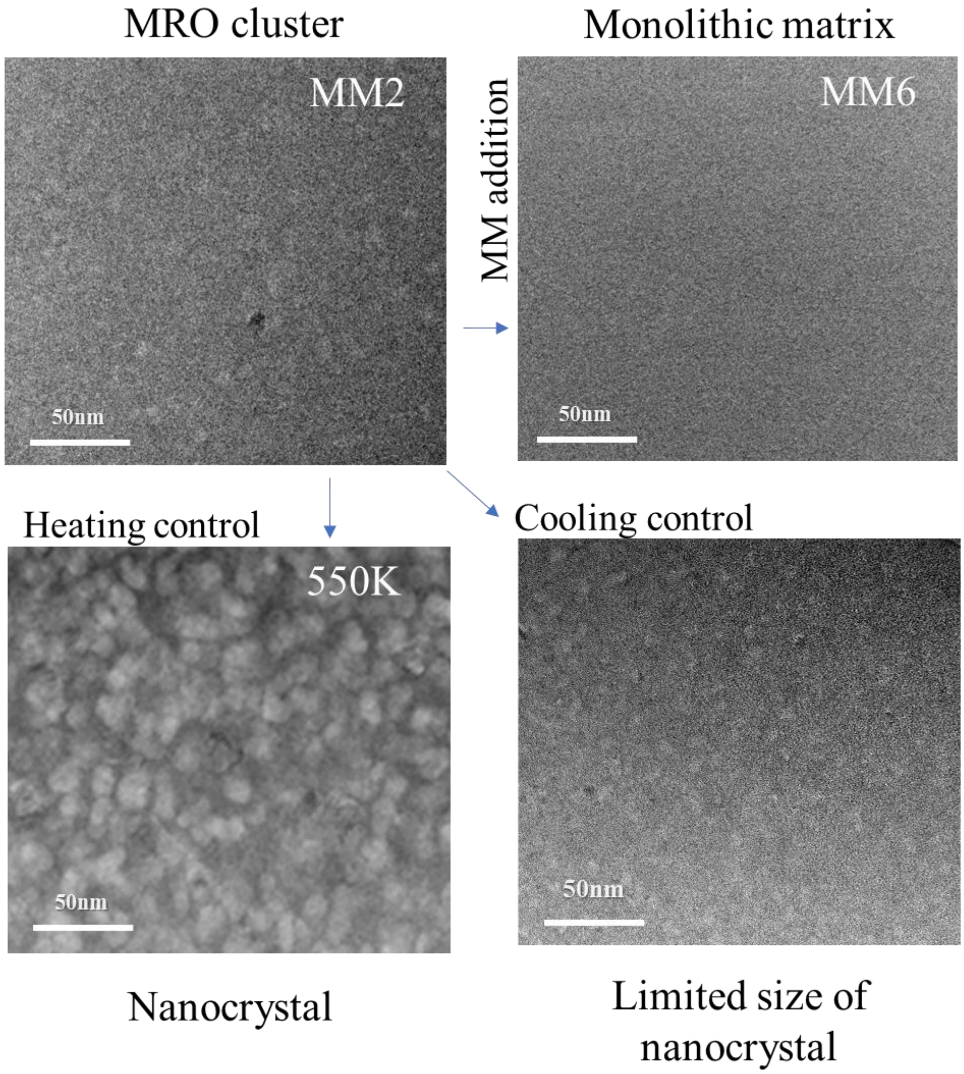

Figure 6.1. Various microstructure change in MM2 depending on the thermal pathway for nucleation of FCC-Al

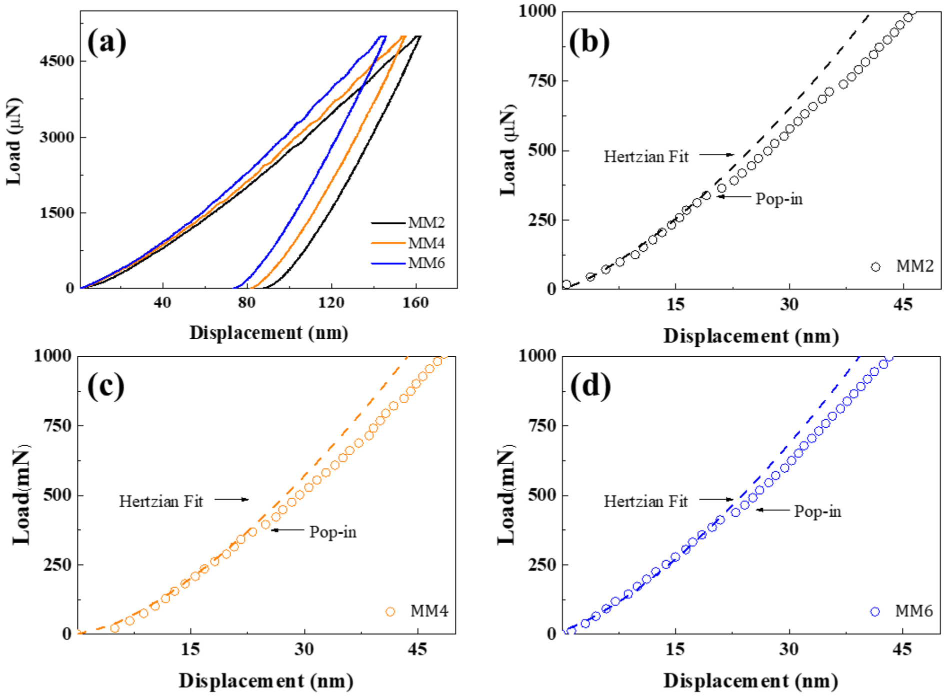

Figure 6.2. load-displacement curve of MM2, MM4, MM6 with the table showing hardness (H, GPa), reduced elastic modulus (E_r, GPa), and yield stress (σ_y, GPa). the representative nanoindentation curves of (b) MM2, (c) MM4, and (d) MM6 with first pop-in where the Hertzian fit starts to deviate from.

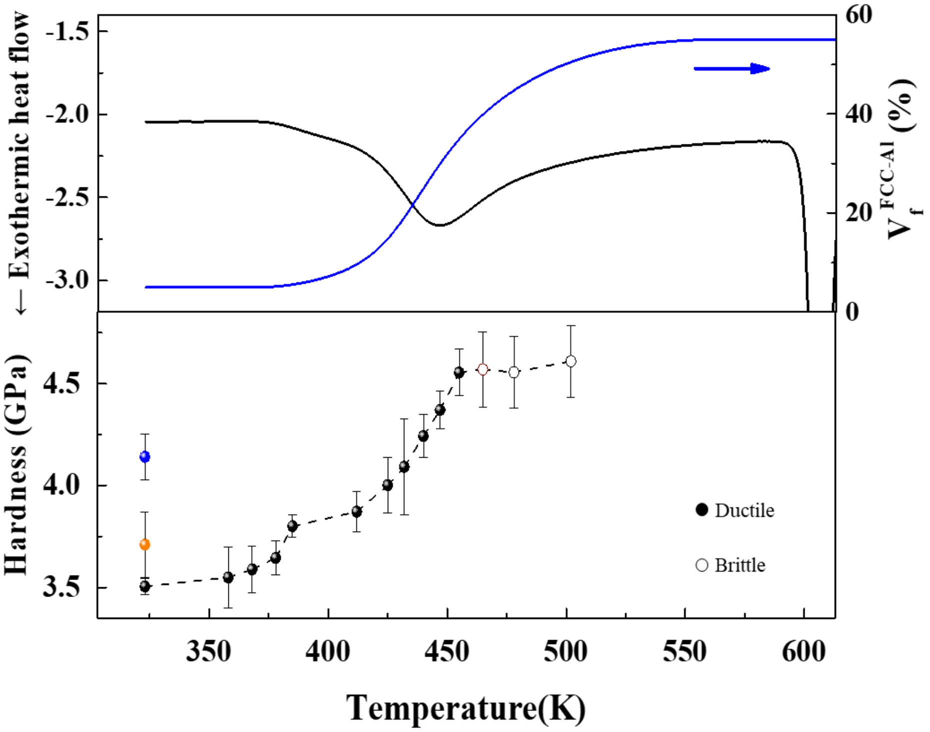

Figure 6.3. Relation between Volume fraction (V_f) of FCC-Al (blue line) and hardness(H) of MM2 composite depending on the annealing temperature. V_f is proportional to the area of crystallization peak (ΔH_X = 58.77 J/g).

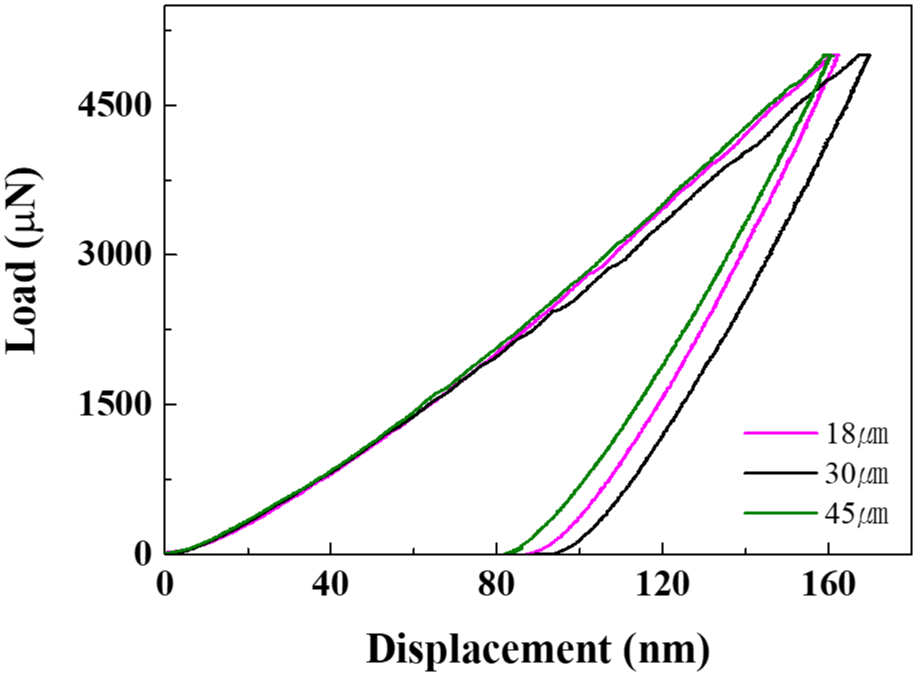

Figure 6.4. Load-displacement curve of MM2, 30μm MM2 and 45μm MM2.

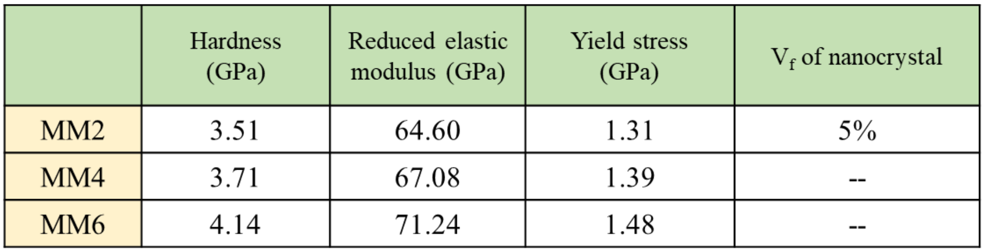

	Hardness (GPa)	Reduced elastic modulus (GPa)	Yield stress (GPa)	V_f of nanocrystal
MM2	3.51	64.60	1.31	5%
MM4	3.71	67.08	1.39	--
MM6	4.14	71.24	1.48	--

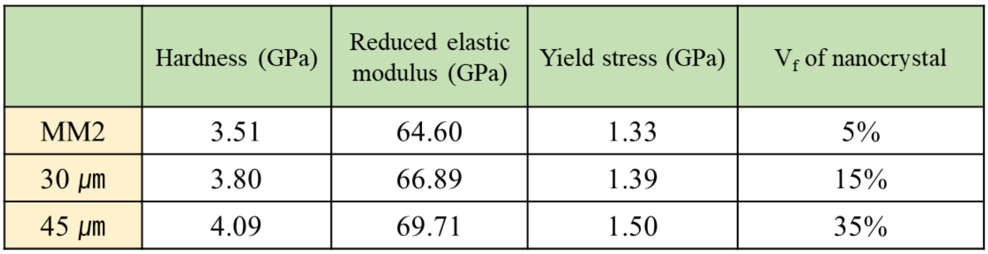

	Hardness (GPa)	Reduced elastic modulus (GPa)	Yield stress (GPa)	V_f of nanocrystal
MM2	3.51	64.60	1.33	5%
30 μm	3.80	66.89	1.39	15%
45 μm	4.09	69.71	1.50	35%

Table 6.1. Average value of hardness (*H*), reduced elastic modulus (E_r) and yield stress (σ_y) of MM2, MM4 MM6 and MM2 with various thickness

6.2.2. Room temperature creep displacement test

It is often considered that amorphous matrix has partially different atomic bonding ambient and so the response of each atomic configurations to the macroscopic loading conditions can be different [108]. This difference results in the time-dependent deformation dynamics which can be explained by Kelvin model. STZs confined within an elastic medium can be reversed by back-stress, and the elastic field can occur stress relaxation leading to macroscopic anelasticity. Phenomenologically, creep behavior is explained in terms of formation, interaction and activation energy of the STZs. Creep mechanism in MGs is also accomplished through the creation, and annihilation of STZs [109]. In this point of view, investigation of creep displacement and anelastic recovery at room temperature is one of the keys to understand the shear deformation. Creep measurements of this research were performed according to the following sequence: after loading the samples up to 30 mN at 2 mN/s, the tip was held at the maximum load for 100 seconds; after unloading at 2 mN/s, the tip was kept forcing for another 100 seconds at 0.02 mN to let the sample recover the anelastic deformation. Creep displacement curves of as-spun samples and annealed MM2 during the constant load (= 30 mN for 100 seconds) are shown in figure 6.5 (a) and (b). During the holding period, the displacement increased rapidly and then started to show the linear increase. For the numerical comparisons, strain rate sensitivity, $m_{ss} = \delta \ln H / \delta \ln \dot{\varepsilon}$ is calculated. Simply put, a positive and high value of m_{ss} often implies reduced tendency for the localization of plastic deformation [110,111]. The strain rate ($\boldsymbol{\dot{\varepsilon} = (1/h_p)(\frac{dh_p}{dt})}$) in nanoindentation is defined as a function of contact depth ($\boldsymbol{h_p = h(t) -}$

$\mathbf{0.75P/(dp/dh(t))}$). When analyzing the indentation depth depending on the time (***h(t)***), the creep displacement-time curves are required to be fitted to following empirical equation;

$$\mathrm{h(t)} = h_0 + a(t - t_o)^b + \mathrm{kt} \quad . \qquad \text{Eq. 6-3}$$

where, h_o, a, t_o, b and k are fitting constant. Hardness depending on the contact depth is defined as $H = P/\pi \boldsymbol{R}^2$. **R** is contact radius ($\mathbf{R} = \sqrt{2\mathrm{R_i h_p} - \mathrm{h_p^2}}$). Calculated m_{ss} values of each sample are marked in figure 6.5(a. b) with the creep displacement curves. The calculated value of m_{ss} is 0.0042 for as-spun MM2, 0.0036 for as-spun MM4 and 0.0032 for as-spun MM6. Compare to soft FCC-Al clusters, atomic mobility around the RE-centered clusters would be suppressed due to their strong bonding nature and low diffusivity of large MM. Consequently, addition of more MM in the amorphous matrix retard the easy creation of STZs and stress relaxation of elastic field. However, m_{ss} of annealed MM2 clearly increases from 0.0042 to 0.017. When the FCC-Al nanocrystals precipitate from the glassy matrix, mass density difference of FCC-Al and amorphous matrix cause the enhancement of strain energy at the interface of FCC-Al. [112] Due to the interface with higher strain energy, abnormal atomic movement products the larger creep displacement [113]. Figure 6.5 (c) and (d) present the anelastic recovery for the as-spun and annealed MM2. Anelastic recovery after creep displacement does not consider the viscoplastic term. The viscoelastic and anelastic deformation can be described with a generalized Kelvin model [114,115], in which can be defined as equation below;

$$\mathrm{h} = \sum_{i=1}^{h} h_i \left(1 - e^{-\frac{t}{\tau_i}}\right) + \frac{t}{\mu_0} \quad . \qquad \text{Eq. 6-4}$$

Where, h_i is the indentation depth and τ_i is the retardation time for the activation of the ith anelastic process. In the second term on the right side of the equation 6-4, t is the time and μ_0 is a constant proportional to the viscosity coefficient of the last dashpot. The anelastic recovery in figure 6.5(c) and (d) are fitted by a series of two exponential decays. Calculated parameters are listed in Table 6.2. The value of h_1 and τ_1 related to the first component of the anelastic deformation has no clear trend. However, the value of h_2 increases with the MM addition or annealing temperature, whereas τ_2 decreases. It was reported that the relaxation intensity (h_i) and the characteristic relaxation time (τ_i) of anelastic process depend on the degree of structural relaxation. To put it concretely, relatively stiffer rigid metallic glass can have the lower h_i and higher τ_i. Creep displacement results claim that addition of MM and precipitation of FCC-Al lead to the aggressive stress relaxation of elastic field during the creep segment.

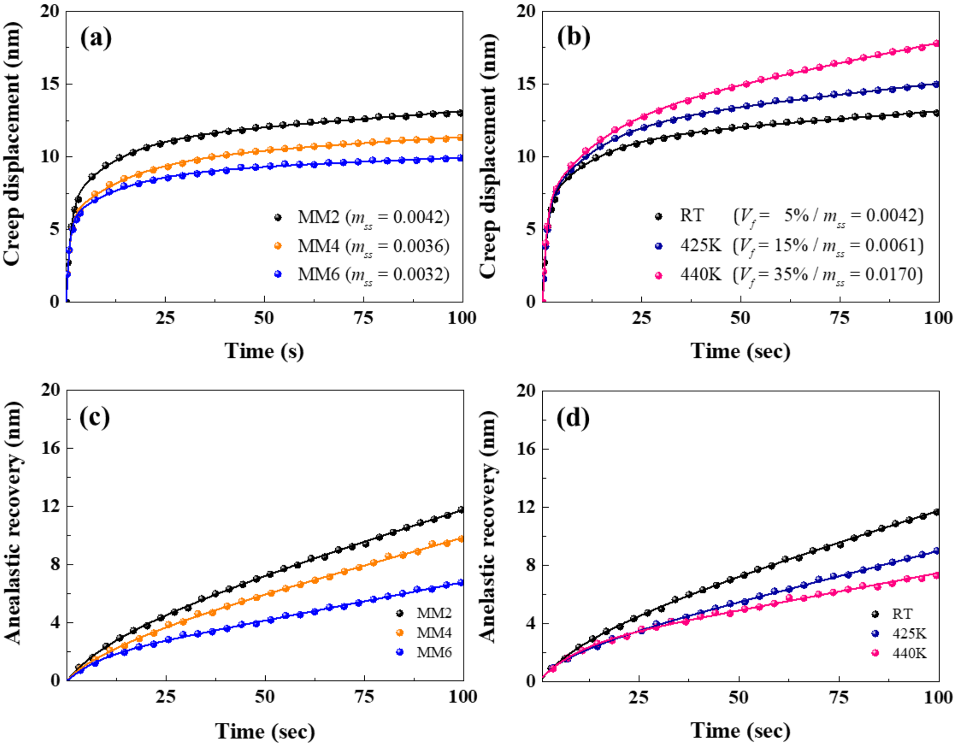

Figure 6.5. Corrected creep curves of (a) as-spun samples and (b) annealed MM2 samples. (c) and (d) is creep recovery curves for as-spun and annealed MM2 samples, respectively.

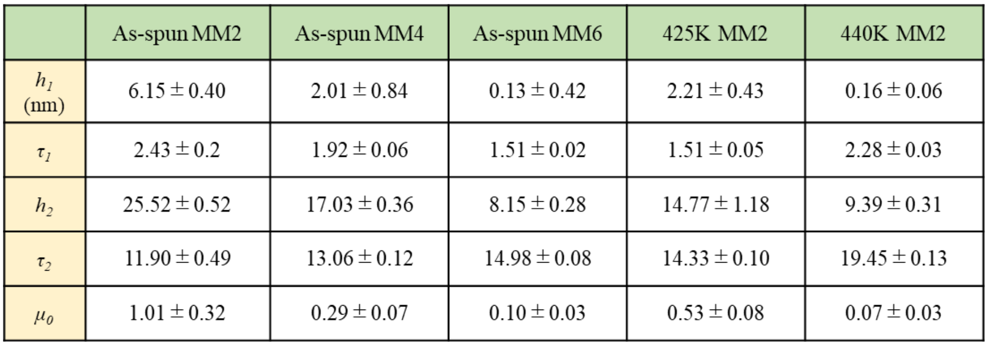

	As-spun MM2	As-spun MM4	As-spun MM6	425K MM2	440K MM2
h_1 (nm)	6.15 ± 0.40	2.01 ± 0.84	0.13 ± 0.42	2.21 ± 0.43	0.16 ± 0.06
τ_1	2.43 ± 0.2	1.92 ± 0.06	1.51 ± 0.02	1.51 ± 0.05	2.28 ± 0.03
h_2	25.52 ± 0.52	17.03 ± 0.36	8.15 ± 0.28	14.77 ± 1.18	9.39 ± 0.31
τ_2	11.90 ± 0.49	13.06 ± 0.12	14.98 ± 0.08	14.33 ± 0.10	19.45 ± 0.13
μ_0	1.01 ± 0.32	0.29 ± 0.07	0.10 ± 0.03	0.53 ± 0.08	0.07 ± 0.03

Table 6.2. Positron lifetimes (LT) and corresponding intensities for evaluationg the RT creep data in as-spun samples and annealed MM2 samples

6.2.3. Statistical analysis of first pop-in for shear band nucleation

Shear band nucleation is a stochastic event, that requires the significantly large number of observations for statistical analysis. J. Perepezko et.al reported that effective approach for statistical analysis based on the nanoindentation measurements. Because of the rapid propagation rate, the pop-in is a nucleation-controlled process [116]. The first pop-in event of indentation is related with the threshold load for shear band nucleation. So, distribution of first pop-in load can represent the nucleation statistics in shear band.

Figure 6.6 is the load versus pop-in in the form of a probability distribution for an as-spun MM2 and MM6 where a distinct 2nd shoulders are existing on the high load side of the distribution. The black solid lines in figure 6.6 are the kernel density of the experimental data based upon 100-200 individual nanoindentation measurement. Interestingly, both of distribution curves shows clear bimodal distribution of nucleation sites. Red and blue dashed lines are separated gaussian distribution, which are obtained by multiple peak fitting of bimodal kernel density. The origin of the bimodal distribution of shear band nucleation is not clearly revealed yet, but the intensity ratio of two gaussian distribution in bimodal distribution clearly reflect the shear band nucleation behavior that can be changed depending on the degree of structural relaxation, composition and loading rate [117].

Comparison of probability distribution of MM2 and MM6 clearly displays that addition of MM (MM2 → MM6) shift the distribution to higher loads and distinctively enhance the shoulder peak on the high load side of the distribution. As confirmed in PDF analysis of chapter 4.2.2, MM6 is the glassy alloy having high density of RE-centered clusters. When the RE-centered clusters with strong bonding energy are introduced in matrix, higher activation energy is required for shear band nucleation. Figure 6.7 shows the bimodal distribution of as-spun MM2 ($V_{f,FCC-Al}$ = 5%), 425K MM2 ($V_{f,FCC-Al}$ = 15%) and 455K MM2 ($V_{f,FCC-Al}$= 35%). With the increased annealing temperature, width of the bimodal distribution is enlarged but the area of fitted high load peak is clearly shrunk from 15% to 5%. Soft core – hard shell structure of precipitated FCC-Al increases the hardness and yield stress as shown in figure 6.3. But the crystal interface and compositional fluctuation around it can works as the heterogeneous nucleation site of shear band [118]. Consequently, one can say that the MG with large intensity of high load peak has the brittle manner but the introducing of amorphous-crystalline interfaces in MG can has the possibility for ductility increase.

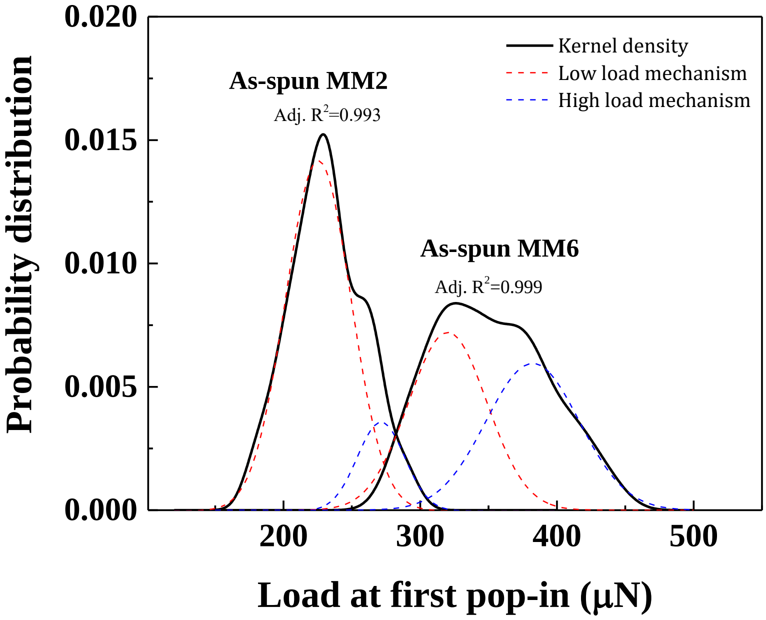

Figure 6.6. Probability function for the load at first pop-ins in MM2 and MM6. Dashed red and blue lines are fitted gaussian distribution representing the hidden S.B nucleation mechanisms

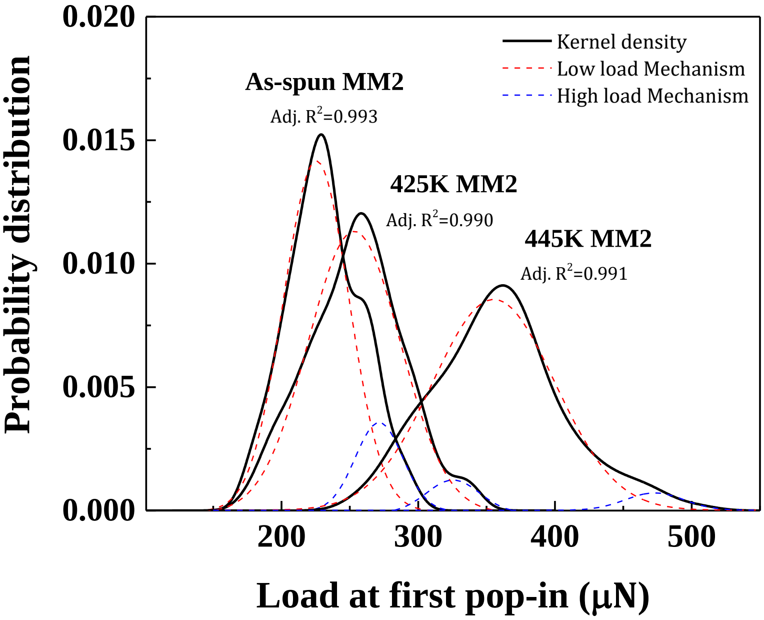

Figure 6.7. Probability function for the load at first pop-ins in as-spun MM2 and annealed MM2. Dashed red and blue lines are fitted gaussian distribution representing the hidden S.B nucleation mechanisms

6.2.4. Statistical analysis of pop-ins size for deformation dynamics

Attempting to acquire the deeper understanding about the mechanical responses effect by the MM addition and partial precipitation of FCC-Al, statistical analysis of pop-in behavior was conducted by follow the same investigation method in chapter 3. On the loading stages of load-displacement curves, discrete pop-ins are observed as results of intermittent deformation of MGs. These pop-in behaviors are corresponded to intermittent shear deformation which is the collective activation of microscopic plastic events, like shear transition zones (STZ) carrying a long-range elastic stress field-like an Eshelby inclusion [119,120].

Cumulative probability distribution of each samples has the universal scaling law distribution function accompanied with the equation 3-6. The cumulative distribution of shear burst below $\mathbf{S_c}$ (cut-off value) follows a power-law relation defined as equation 3-6. When the cumulative distribution has the relatively large β_S the distribution has the sharper drop of P(>S), which is equivalent to the relatively larger number of small-size of strain bursts. Conversely, the smaller value of β_S means the wider distribution that is not concentrated in a small S range. Shear burst undergoes the cooperative atomic motion which results in the formation of concordant region of STZs [121]. These shear bursts following the power-law relation can be comprehended in terms of the local inelastic rearrangement of concordant regions, which remained in a jammed state [121,122]. With increasing shear burst size above S_c, the exponential decay factor takes effect. These large shear bursts overcome the rigidly jammed state and originate the propagation of macroscopic shear deformation from the spatial connection of the deformation units. Therefore, both of β_s and S_c can be applied to investigate the dynamic responses of shear bands during plastic deformation of metallic glasses.

Figure 6.8 (a) is the cumulative probability distribution (P(>S)) of the as-spun samples fitted by equation 3-6. Figure 6.8(b-d) are the size distribution histograms for the shear bursts. The solid lines exhibit the differentiation of the squared exponential decay function and dashed lines exhibit the cut off value obtained from the figure 6.8(a). As shown in figure 6.8, the value of β_s of MM2 is 0.247, 0.375 for MM4 and 0.551 for MM6, respectively. Based on the different results in each histogram (figure 6.8(b-d)) and the value of scale exponent (fig 6.8(a)), the relationship between β_s and the size distribution of shear bursts can be described in detail. Size distribution of MM2 (β_s = 0.247) shows the chaotic dynamics and the small gaussian-like peak at the S=0.01, which is similar with the shear dynamics of fragile Al-based metallic glasses [123]. Meanwhile, histogram of MM6 (β_s = 0.551) is characterized by a monolithically decreasing distribution of shear bursts that is concentrated within a smaller S range. The transition trend from gaussian distribution to power-law distribution in histogram implies a transition in deformation mechanism [132]. It means that in the viewpoint of shear burst dynamics, the dynamics changes from chaotic state (CDZ) to self-organized critical state (SDZ) with the addition of MM components . The value of S_c also increases from 0.013 to 0.017 with the MM contents. Small value of S_c indicates the reduction in the nucleation barrier for the chaotic shear burst, which is supported by the enlarged concordant region.

Previous reports have claimed that large concordant region results in the multiple nucleation of shear bands with complex deformation behavior due to the simultaneous occurrence of numerous shear deformation in relatively large volumes [124]. The Al clusters or nanocrystals embedded in the amorphous matrix of MM2 have the weaker thermal stability that cause the faster self-diffusion of aluminum atoms [53], and lower σ_y than amorphous matrix [54]. Thus, reduced β_s and S in MM2 can be attributed to the fact that the soft Al cluster which can act as soft spots preferred for the easy activation of shear deformation. After ergodically processing of the pop-ins by following the same methods conducted to the as-spun samples, size distributions and cumulative probability distribution of shear burst in annealed MM2 are shown in figure 6.9. The percentage of shear bursts larger than a certain value, i.e., the cumulative probability distribution P, is fitted by equation 3-6 and the calculated results (β_s, S_c) are also shown with the size distributions. In contrast with the shear burst histograms (figure 6.8(b)-(d)) of as-spun MM2, MM4 and MM6 samples having similar S ranges, maximum shear burst size of annealed MM2 are dramatically diminished with the annealing temperature. S_c decreases to certain value, but the value of β_s increase. Through the increase of V_f of FCC-Al, decrease of S_c indicates the reduction in the barrier for the shear bands with the minor increase of population at $S < S_c$. This results in the decrease of the critical stress for shear band nucleation. At the same time, the drastic increase of β_s means that the small shear bursts related with the jammed concordant regions (or SOC states) are considerably promoted by the interface between solute enriched matrix and nano scaled FCC-Al. The results of statistical analysis can be attributed the fact that introduction of soft α-Al can trigger the multiple nucleation (low S_c due to interface) but inhibit the propagation of shear bursts (high β_s due to solute enriched area with strong atomic bonding). This dispersed shear bursting behavior hinder the localized single shear band which can cause early fracture. Instead, the plasticity shows more homogeneous behavior in the form of multiple shear band, which result in high strains to macroscopic failure and an apparent ductility in the Al-based metallic glass composites.

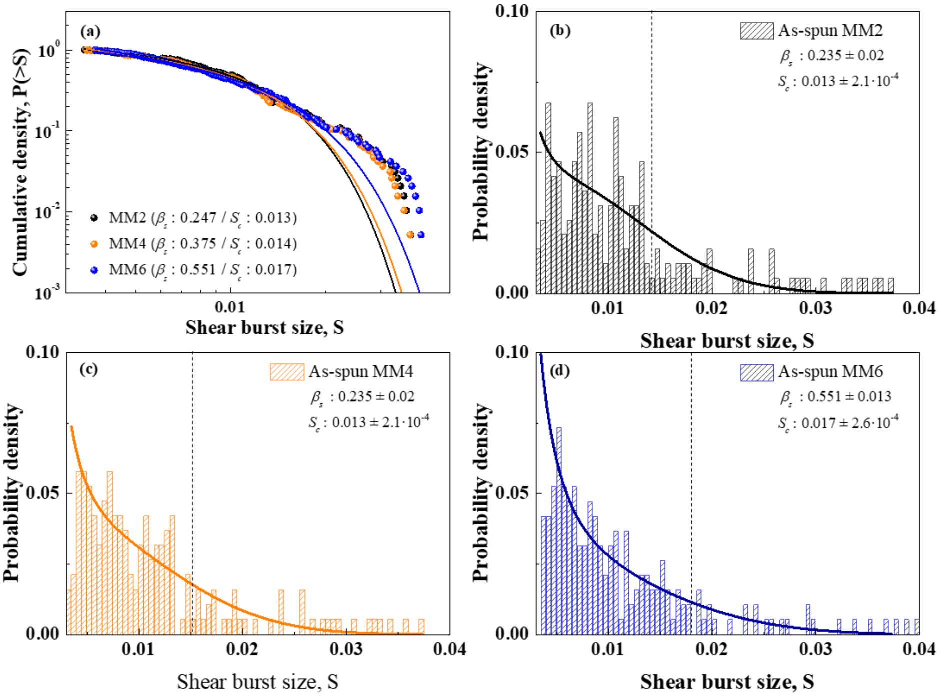

Figure 6.8. (a) Cumulative distribution of shear bursts. And size distribution (=histrogram) of shear bursts (S) collected from the loading curves of nanoindentation tests with (b) MM2, (c) MM4, (d) MM6. (Bin size for S is 5×10^{-4}).

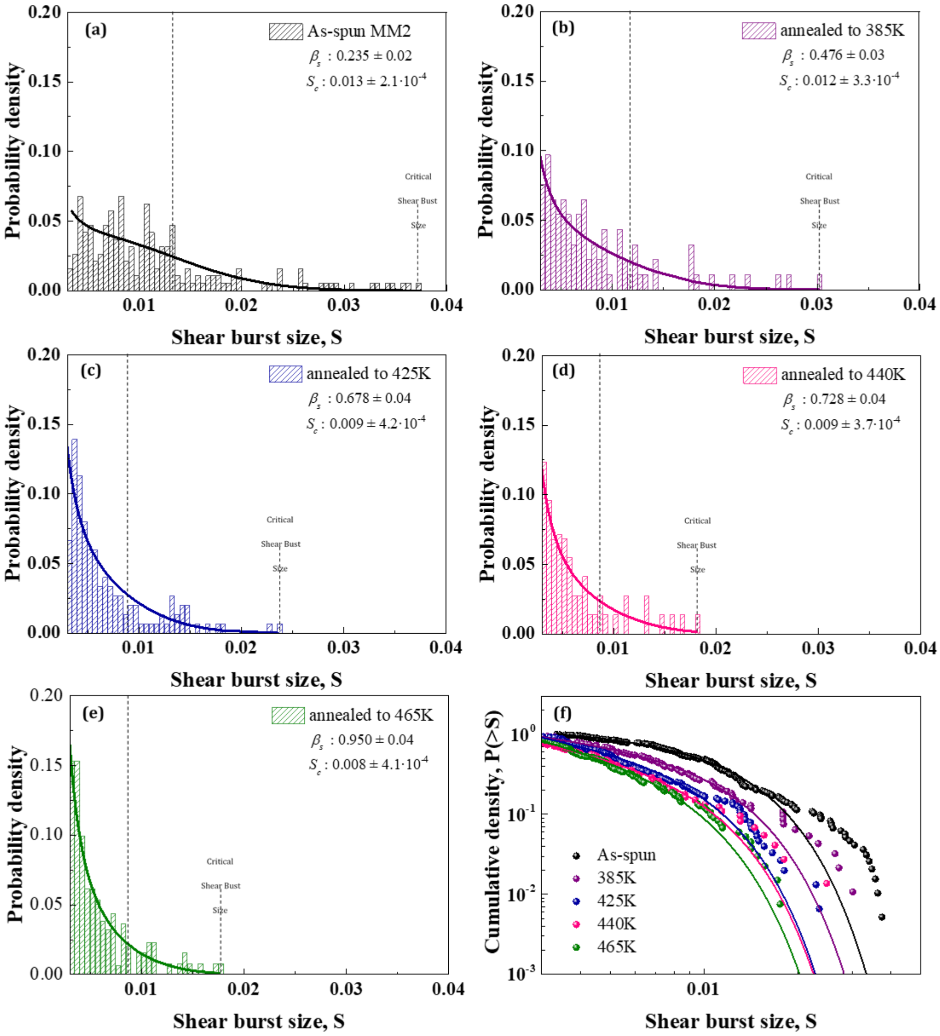

Figure 6.9. Size distribution (=histrogram) of shear bursts (S) collected from the loading curves of nanoindentation tests with (a) As-spun MM2, MM2 MG composite annealed to (b) 385 K, (c) 425 K, (d) 440 K , (e) 465 K. (Bin size for S is 5×10^{-4}) And (f) Cumulative distribution of shear bursts derived from the size distribution.

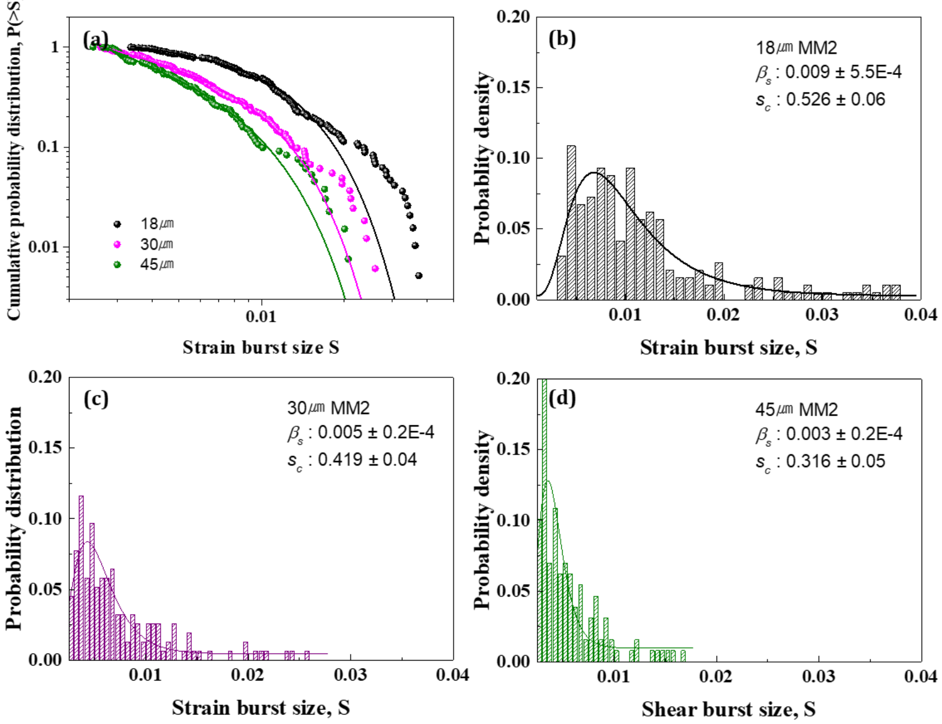

Figure 6.10. (a) Cumulative distribution of shear bursts. And size distribution (=histrogram) of shear bursts (*S*) collected from the loading curves of nanoindentation tests with (b) MM2, (c) 30μm MM2, and (d) 45μm MM2. (Bin size for *S* is 5×10^{-4}).

6.3. Macro-scaled deformation of Al-based metallic glasses

6.3.1. Ribbon bending test

Following the investigation of nano-scaled mechanical responses, macro-scaled bending test was performed to evaluate the macro-scaled deformation behavior of as-spun MM2, MM4 and MM6. Bending test is one of the effective methods to evaluate the flow stress and the degree of ductility of ribbon samples [125]. When the strain applied on the bended ribbon is higher than the elastic limitation, intensive shear steps take place at the apex of curvature and leave the permanently deformed area called as kink angle [126,127]. In the case of samples with brittle manner, the degree of shear localization would be large and leave higher shear steps, which yield the high kink angle after the bending test.

The value of strain applied on the curvature of the bended sample is defined as equation 6-5, and the estimated strain rate is equation 6-6 [128]

$$\varepsilon = \frac{d_t}{D-d} \quad . \qquad \text{Eq. 6-5}$$

$$\dot{\varepsilon} = \left|\frac{d\varepsilon}{dt}\right| = \left(\frac{Vd}{D-d}\right)^2 \quad . \qquad \text{Eq. 6-6}$$

Here, **v** (mm/s) is the approaching speed of the movable platen. **D** is distance (mm) between movable platen and fixed state, and **d_t** is the thickness (mm) of the sample. The ribbons were bended at the constant rate until reaching to the end position. The approximate geometry of ribbon sample during the bending is assumed to form the perfect circle.

To confirm the accuracy of bending deformation depending on the test condition, we induced various estimated strain rate by applying displacement speed (**v** = 0.05 mm/s and 1.0 mm/s) and adjusting the different final distances between fixed and movable plate (**D** = 0.7 mm and 2 mm). Figure 6.11 is the kink angle map showing the relation between permanently deformed kink angle and estimated strain rate. When the given **D** value is constant, kink angle decreases with the estimated strain rate ($\dot{\varepsilon}$). Propagation of shear deformation in MGs can be account for the liquid-like transition, which is kinetically occur depending on the exterior conditions, such as strain rate, applied stress. Consequently, this shear deformation kinetics come up with the reversed relation between kink angle size and the strain rate.

By applying the movement speed of 0.05 mm/s to the moving plate and 0.7 mm of final distance between the fixed and movable plate, different kinking happened on each sample as shown in optical microscopy images of figure 6.12. Measured kink angle of MM2, MM4 and MM6 is 35°, 39°, and 46°, respectively. When σ_y for the shear deformation is low, strain for the initiation of shear steps would also be low and leave the wider circular sector in kinked area. Thus, as dark-field OM image in figure 6.13, the circular sector in kinked area is reduced with the MM contents which affect σ_y of the $Al_{90-x}Ni_{10}MM_x$ amorphous alloy system. Based on the statistical analysis of shear burst discussed in the previous chapter, it is anticipated that soft MM2 with relatively low β_s, S_c has the ductile manner, which is a consequence of multiple shear bands induced by the chaotic dynamics of shear bursts. Due to this intrinsic deformation behavior, bended MM2 shows the lower kink angle with wider circular sector. In comparison, MM6 with relatively strong Al-RE bonding configuration has the higher kink angle and the brittle manner.

To link the understanding of the nano-scaled statistical analysis with microscopic plastic deformation, bending test also performed to the annealed MM2. Figure 6.14 display the cross-section image of bended ribbons manipulated by various thermal pathways. Each sample were bended by two parallel platens until their distance reaches to 0.7 mm with the platen speed of 0.75mm/s. Final strain applied on the surface of bended ribbon was 2.9 %. Precipitation of nano-scaled FCC-Al induces the solute enrichment, and this solute enriched area possessing high portion of strong atomic bonding would be the reason for the hardening. Interestingly, kink angle of annealed MM2 reduces with the V_f of FCC-Al. Consequently, the degree of the deviation between micro-scaled and nano-scaled elastic recovery is constantly increasing. This means that the precipitation of FCC-Al before having brittle solute enriched shell (>18 at%) is the key factor for increasing the hardness and ductility simultaneously.

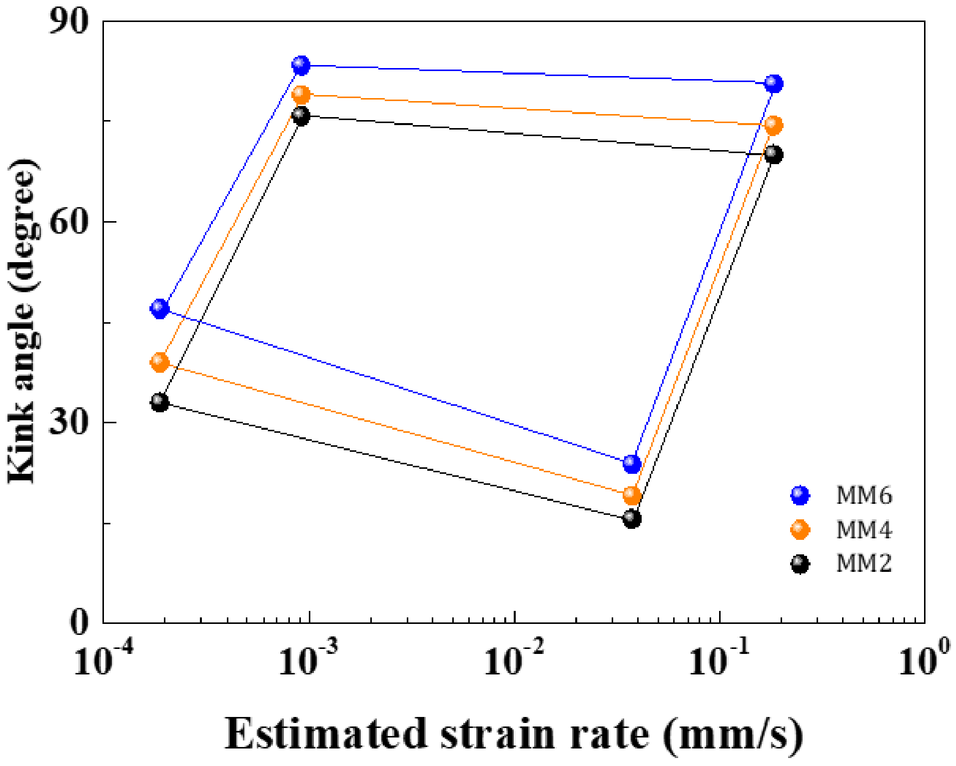

Figure 6.11. Kink angle map of as spun MM2, MM4 and MM6 depending on the estimated strain rate, which is a function of bending distance and speed.

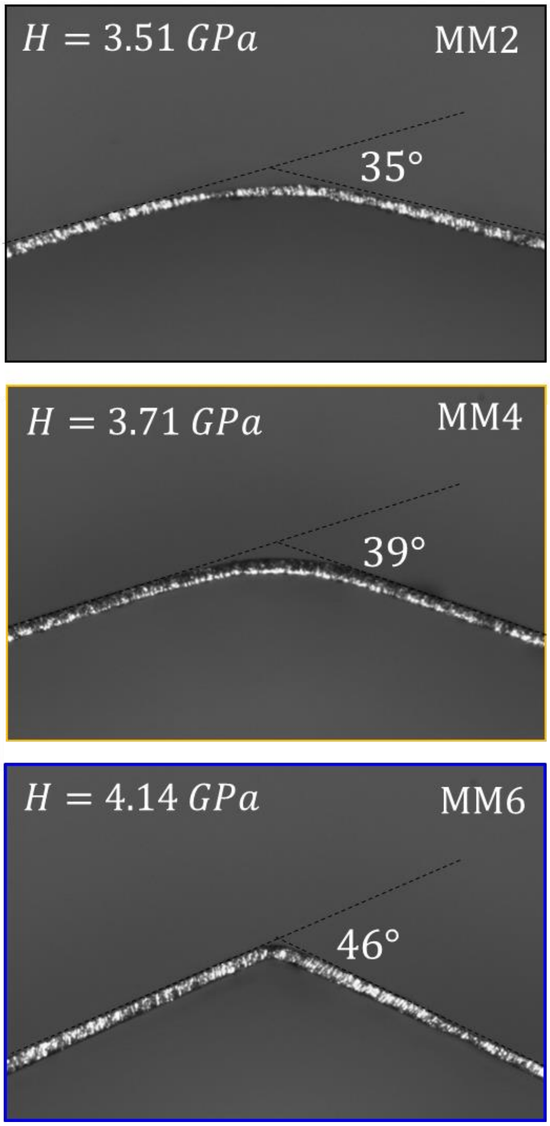

Figure 6.12. Cross-section image of bended MM2, MM4 and MM6 ribbons showing kink angle.

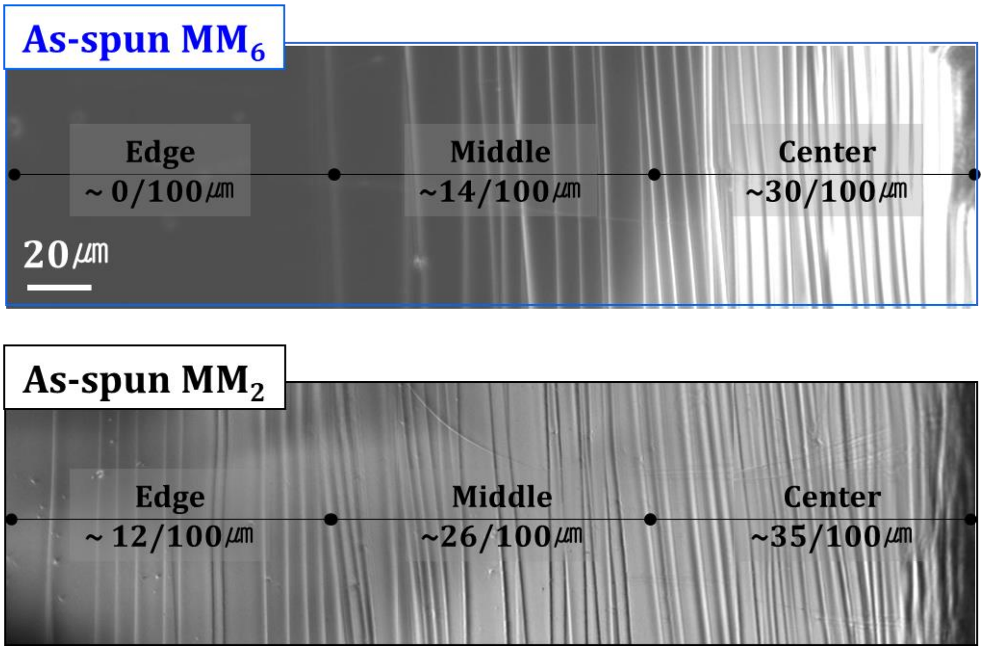

Figure 6.13. Dark-field OM image of bended MM2 and MM6 ribbon samples

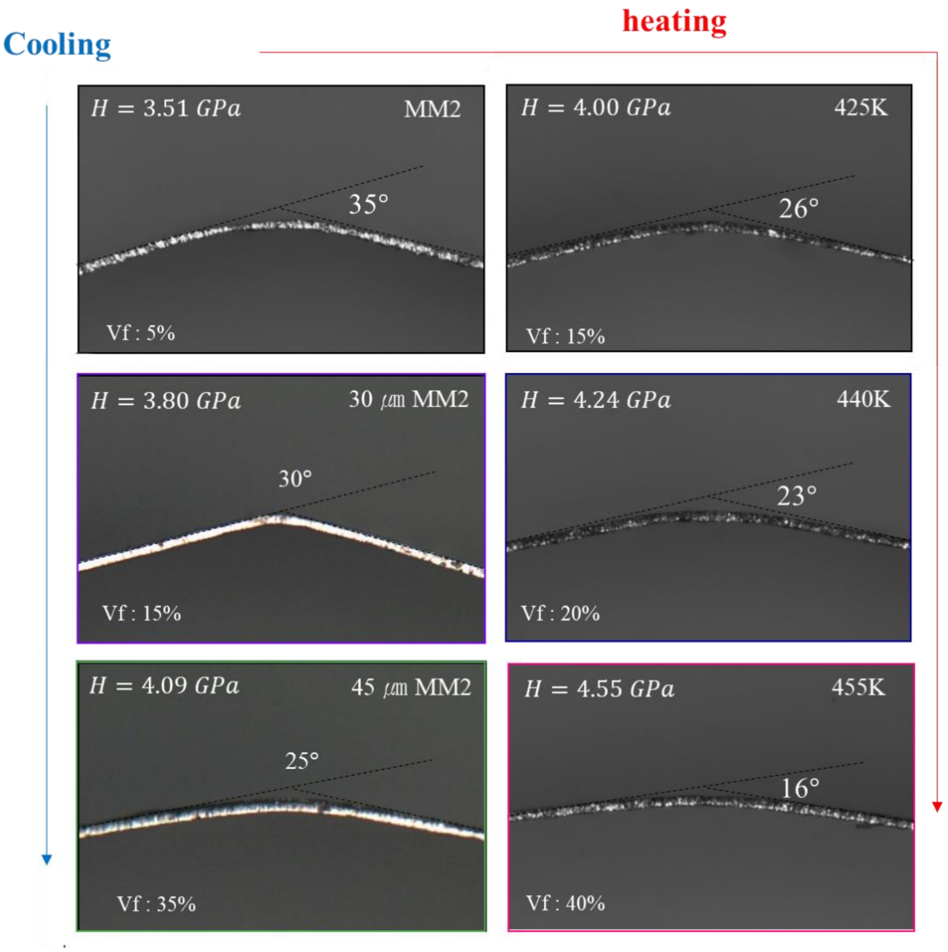

Figure 6.14. Cross-section image of bended MM2 ribbon samples which are prepared by various thermal pathway (As-spun. Annealing, cooling rate control)

6.3.2 Cyclic ribbon tensile test.

Bending test results certified that FCC-Al can extend the room temperature plasticity of Al-based MGs. In this chapter, to add the evidence for enhanced plasticity, tensile test is performed. 18μm MM2, 30μm MM2, 45μm MM2 ribbons were Quasi-statically tensioned through a tensile tester. Strain rate was $2 \cdot 10^{-4}/s$ and the gauge length of 5 mm is applied. To eliminate the geometrical factors, size of ribbon samples was polished and made into the tensile test specimen with width of ~ 3mm. Stress-strain (σ-ε) curves in figure 6.15 show an interesting non-linear behavior. At beginning, the curves show the obvious linear region followed by a significant deviation. The curved σ-ε relation, which is merely shown in bulk scaled specimen is repeatedly observed in every ribbon specimen. Related to this, one should consider the combination of various strain components.

It was reported [129] that glassy metallic alloys exhibit at least four type of strain component (1)ideal elasticity (recoverable, instantaneous), (2)anelasticity (recoverable, time-dependent) (c)viscoelasticity (permanent, time-dependent) and (d)instantaneous plasticity (permanent, instantaneous). Related to the curved σ-ε, Banerjee et.al al mentioned that portion of elastic and viscoelastic component must be considered together as shown in following equation that contains the viscosity as one of the variations [130].

$$\sigma = E_0\epsilon\left[1 - \chi\left\{\frac{1 - e^{-\beta}}{\beta}\right\}\right], (\beta = \frac{E_0\epsilon}{\alpha\eta}) \quad . \qquad \text{Eq. 6-7}$$

Where, E_0 is effective elastic modulus, χ is the portion of viscoelastic parts.

η is the viscosity value came from viscoelastic component. Consequently, one can say that viscoelastic and anelastic strain components, which are the function of temperature and time, restrict the proper observation of plasticity in ribbon tensile test. To overcome this experimental limitation, cyclic tensile test [131] was performed. Maximum stress for each tensile sequence was increased by 50 MPa from 600 MPa until catastrophic failure occurs. Figure 6.16 shows the representative cyclic tensile test results. The degree of deviation of σ-ε curves (colored area) means the percentage of permanent deformation. and the width between the dashed line represent the elastically deformed area. maximum stress is increased from 903 MPa (MM2) to 1112 MPa (45μm MM2). And ratio of plastic deformation vs elastic deformation ($\varepsilon_{pl}/\varepsilon_{el}$) is also increased almost 5 times higher from 0.038 (MM2) to 0.21 (45μm MM2). This results clearly suggest that precipitation of higher number density of FCC-Al can increase the strength and ductility

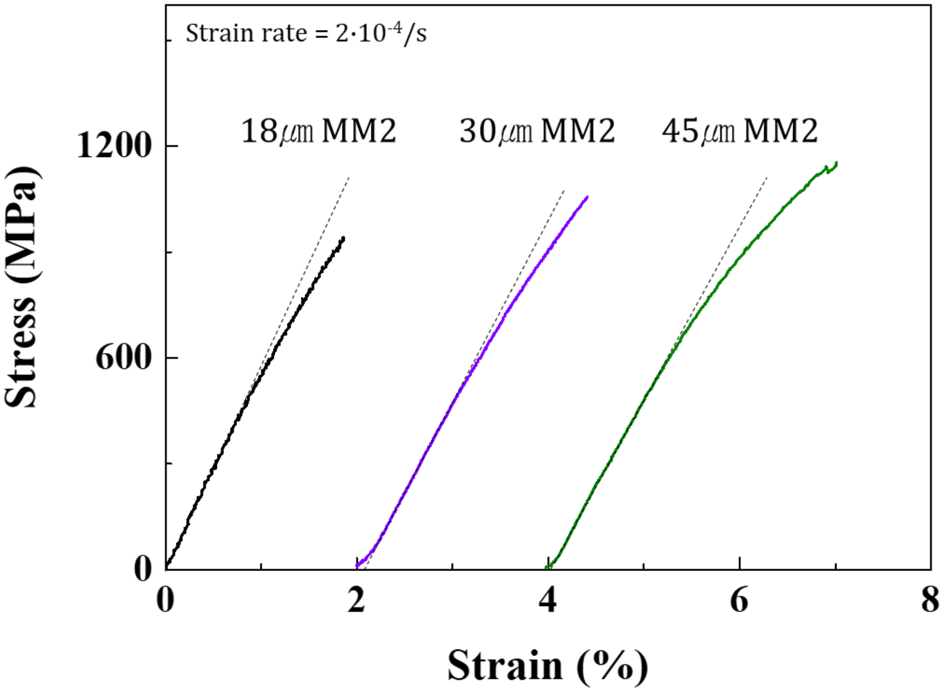

Figure 6.15. uniaxial tensile test results of MM2, 30μm MM2 and 45μm MM2. Inserted image shows the preparing method for ribbon tensile test.

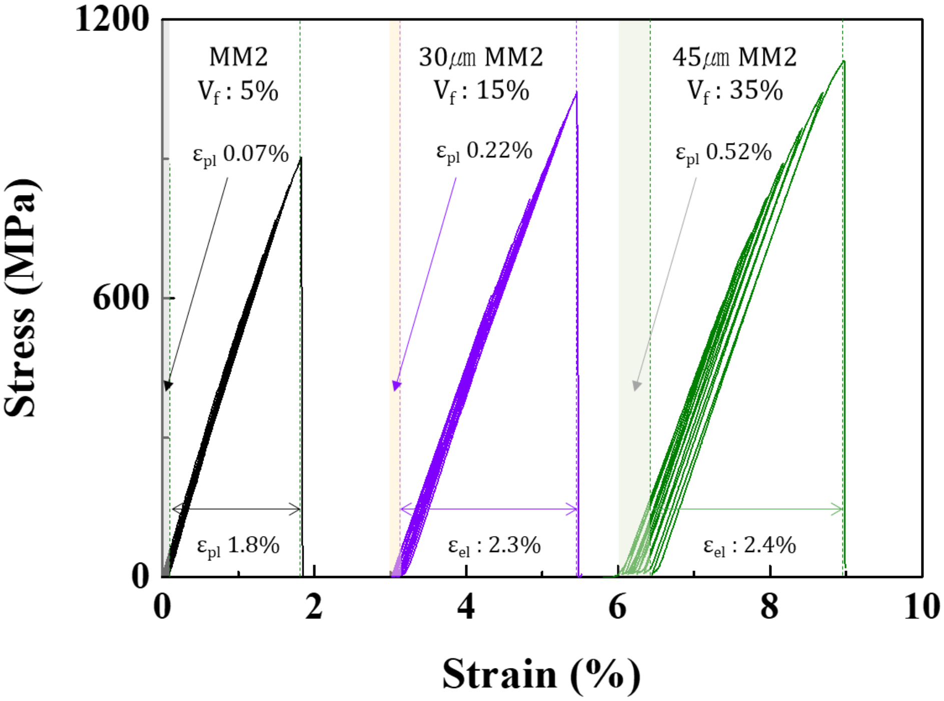

Figure 6.16. cyclic tensile test results of MM2, 30μm MM2 and 45μm MM2. ε_{el} and ε_{pl} represent the portion of elastically deformed area and plastically deformed area, respectively.

6.4 Summary

To reveal the mechanical responses of $Al_{90-x}Ni_{10}MM_x$ MGs, which can be changed depending on the MM compositions and volume fraction of FCCl-Al, comprehensive deformation analysis was conducted. Through the changed nature of the shear bursts depending on the MM composition and volume fraction of FCC-Al, it was confirmed that the lower barrier (low value of $\mathbf{S_c}$) for the chaotic shear deformation is the key for ductility of MGs. Macro-scaled bending test experimentally showed that samples with low $\mathbf{S_c}$ has a possibility to have the ductile manner. Abnormal ductility of hardened MM2 with FCC-Al was also verified via room temperature creep test. From the high strain rate sensitivity and low relaxation intensity in annealed MM2, it was experimentally confirmed that FCC-Al was working as the source for easy nucleation of shear deformation. Finally, cyclic tensile test clearly showed that precipitation of MM2 increases both of the strength and ductility of Al-based MG.

Chapter 7.

Conclusions

Al-TM-RE metallic glass with FCC-Al nanocrystal have the attractive combination of high strength and low density. High density of FCC-Al (~ $10^{23}m^{-3}$), which are precipitated from the catalytic precursor upon low temperature induces the solute-enriched area around their interface and results in the improved mechanical properties. Therefore, the analysis of the nucleation kinetics of FCC-Al is important to manipulate the Al-based metallic glass with optimized properties. In this study, research topic can be grouped into 3 topics: (1) Understand of the phase stability of Al-TM-RE glass formers, (2) Quantitative investigation of the nucleation kinetics of FCC-Al and (3) Comprehensive explanation about the mechanical responses effected by partially precipitated FCC-Al.

Based on the Miracle's topological mode, many researchers have tried to explain the relation between atomic structure and crystallization behavior of the Al-based system. And recently it was concluded that the spatial heterogeneities induced by the high portion of Al-MRO is the origin of the low temperature precipitation of FCC-Al. Interestingly, due to the large size of RE elements, small tuning of RE in Al-TM-RE system can dramatically change their bonding structure of the system including density of Al-MRO. To investigate the RE effect on the thermal properties and crystallization behavior, multiple REs were added in $Al_{84}Ni_{10}RE_6$ system with the equiatomic ratio. As a result, it was confirmed that addition of multiple REs can increases the fragility of the system that presents the atomic packing efficiency. The width of super-cooled liquid region of $Al_{84}Ni_{10}RE_6$ also increased with the number of REs. In addition, crystallization mode of $Al_{84}Ni_{10}RE_6$ can be changed from eutectic crystallization to primary crystallization by the proper selection of REs.

Combining with the nucleation kinetics and FDSC, the nucleation kinetics of FCC-Al in $Al_{88}Ni_{10}MM_2$ was intensively studied. $Al_{86}Ni_{10}MM_4$ $Al_{84}Ni_{10}MM_6$ were also used to help the understanding. $Al_{88}Ni_{10}MM_2$ is the metallic glass which possesses the small portion of FCC-Al in as-spun state. Through the TEM and in-situ SAXS analysis, it was confirmed that the pre-crystallized FCC-Al and newly precipitated FCC-Al in annealed $Al_{88}Ni_{10}MM_2$ grow up to diameter of 14 nm. Interestingly, cooling process also adapted to control the size and number density of the FCC-Al. Pre-annealing and scanning FDSC experiments revealed the evolution of the T_g and T_x with annealing time. When the given annealing time is longer than the incubation time for nucleation of FCC-Al, the degree of the evolution of T_g and T_x can be increased further. Based on these experimental factors, incubation time for nucleation was measured through the wide temperature range. Consequently, TTT diagram for FCC-Al in $Al_{88}Ni_{10}MM_2$ and $Al_{86}Ni_{10}MM_4$ was successfully obtained. Comparison of the effective melt-spinning cooling rate and TTT diagram of FCC-Al in $Al_{88}Ni_{10}MM_2$ revealed that cooling path of melt-spinning process passes the c-nose of FCC-Al.

FCC-Al has been considered as the 2nd phase that can enhance the strength and ductility of Al-based system. But, no clear results about room temperature plasticity of Al-based metallic glass has been reported yet. To claim their plasticity, comprehensive deformation analysis was conducted on $Al_{90-x}Ni_{10}MM_x$ metallic glasses from nano-scale to macro-scale by using various technique. Through the statistical analysis of first pop-in and pop-ins, it was confirmed that the precipitation of FCC-Al decreased the Sc value which means the barrier for the chaotic shear deformation. Finally, cyclic tensile test clearly showed that precipitation of FCC-Al increases both of the strength and ductility of Al-based MG.

From the results of this study, crystallization behavior of FCC-Al was deeply studied and TTT-diagram that can explain the crystallization behavior of FCC-Al was obtained. It is expected that the sound understanding of relation between mechanical properties and structural variation of Al-based MGs will contribute significantly to the new strategies for developing not only Al-based system but also the overall glass forming systems and metallic glass composites.

Bibliography

1. A.L. Greer, E. Mar, *MRS Bull.* **32,** 611 (2007).
2. J.J Kruzic, *Adv. Eng. Mater.* **18,** 1308 (2016)
3. H.A. Davies, J. Non-Crystalline Solids, 17, 266 (1975)
4. R.I Wu, G. Wilde, and J.H. Perepezko, *Mater. Sci Eng,* **A 301,** 12 (2001)
5. I. Gallino, R. Busch, *JOM,* **69,** 2171 (2017)
6. P. Predecki, B.C. Giessen, N.J. Grant. *Transactions of the Metallurgical Society of AIME.* **233,** 1438 (1965)
7. H.A. Davies. K.B Hull, *Scripta Metall.* **6,** 241 (1972)
8. A. Inoue, A. Kitamura, T. Masumoto. *J. Mater.Sci,* **16,** 1895-1908 (1981)
9. Y. He, S.J Poon, G.J. Shiflet. *Science,* **241,** 1640-1642 1988
10. B.J. Yang, J.H. Yao, Y.S. Chao, J.Q. Wang, E. Ma, *Phil. Mag,* **90,** 3215-3231 (2010)
11. N.C. Wu, L. Zuo, J.Q. Wang, E. Ma, *Acta Mater,* **108,** 143-151 (2016)
12. S.Y. Kim, G.Y. Lee, G.H. Park, H.A. Kim, A.Y. Lee, S. Scudino, K. G. Prashanth, D.H. Kim, J. Eckert, M.H. Lee, *Sci, Rep,* **8,** 1090 (2018)
13. Z.P. Chen, J.E. Gao, Y. Wu, H. Wang, X.J. Liu, Z.P. Liu, Sci, Rep, 3, 03353 (2013)
14. A.L Greer, *Science,* **267,** 1947-1953 (1995)
15. D. Kan, X. Li, B. Yang, H. Yang, J. Wang, *J. Mate Sci & Tech,* **31,** 489-492 (2015)
16. A. Inoue, Y. Kawamura, H.M. Kimura, H. Mano, *J. Mata and Nanocryst. Mater,* **10**, 129-136 (2001)

17. M. Salehi, S.G. Shabestari, S.M.A. Boutorabi, *Mater Sci and Eng,* **A586,** 407-412 (2013)

18. U. Köster, P. Weiss, *J. Non-Cryst. Solids*. **17,** 359–368 (1975)

19. U. Köster, U. Herald, Glassy Metals I, edited by H. Beck, and H.-J. Güntherodt, Springer-Verlag, Berlin, 225. 1981

20. R.D. Sá Liaboa, C. Bolfarini, W.J. Botta F, C. S. Kiminami, *Appl. Phys. Lett,* **86,** 211904 (2005)

21. Q. Li Q, E. Johnson, M.B Madsen, A Johansen, L. Sarholt-Kristensen. *Philos. Mag. B,* **66,** 427 (1992)

22. G. Wilde, N. Boucharat, R.J. Hebert, H. Rösner, W.S. Tong, J.H. Perepezko, *Adv. Eng. Mater,* **5,** 125. (2003)

23. E. Pekarskaya, J.F. Löffler, W.L.Johnson, Acta Mater. **51,** 4045-4057 (2003)

24. K.F. Kelton. *J. Non-Cryst. Solids.* **274,** 147, (2000)

25. A. Inoue, M. Yamamoto, H.M. Kimura, T. Masumoto. *J. Mater. Sci,* **6,** 194, (1987)

26. A. Inoue, Y. Bizen, H.M. Kimura, T. Masumoto, M. Sakamoto. *J. Mater. Sci* **23,** 3640, (1988)

27. K.F. Kelton, Intermetallics. **14,** 996 (2006).

28. H.A. Kramer, *Physica,* **7,** 284 (1940)

29. J. Schroers, Y. Wu, R. Busch, W.L. Johnson, Acta Mater, 49, 2773 (2001)

30. J. Deubener, R. Briickner, M. Sternitzke, *J. Non-Cryst. Solids,* 163 1 (1993)

31. D.R. Allen, J.C. Foley, J.H. Perepezko, *Acta Mater,* **46,** 431, (1998)

32. K.F. Kelton, T.K. Croat, A.K. Gangopadhyay, L.Q. Xing, A.L. Greer, M. Weyland, X. Li, K. Rajan, *J. Non-Cryst. Solids,* **317,** 71 (2003)

33. U. Köster, J. Meinhardt, *Mater..Sci. Eng,* **A178,** 271 (1994)
34. S.D. Imhoff, J. Ilavsky, F. Zhang, P.Jemian, P.G. Evans, J.H. Perepezko, *J. Appl. Phys.* **111,** 063525 (2012)
35. K.W. Kim, J. Kim, Y.D. Yun, H. Ahn, B. Min, N.H. Kim, S. Rah, H.Y. Kim, C.S. Lee, I.D. Seo, W.W. Lee, H.J Choi, K.S. Jin, Biodesign, **5,** 24 (2017)
36. B. Geiser, D. Larson, E. Oltman, S. Gerstl, D. Reinhard, T. Kelly, T. Prosa, *Microsc. Microanal,* **15,** 292 (2009)
37. A. Inoue. *Acta Mater*. **48,** 279 (2000)
38. H.W. Sheng, Y.Q. Cheng, P.L. Lee, S.D. Shastri, E. Ma, *Acta Mater,* **56,** 6364 (2008)
39. Aiwu Zhu, Gary J. Shiflet, Daniel B. Miracle, *Scripta Mater,* **50,** 987 (2004)
40. X. LI, X. Bian, L. Hu, Y. Wu, J. Guo, J. Zhang, *J. Appl. Phys,* **101,** 103540 (2007)
41. L. Zhang, K.J. Chen, X.F. Huang, Y.S. Wu, X.F. Bian, *J. Phys. Condens. Matter*, **13,** 5947 (2001)
42. J.H. Perepezko, R.J. Herbert, W.S. Tong, *Intermetallics*, **10,** 1079 (2002)
43. V.A. Podergin, *Poroshkovaya Metallurgiya, **8,*** 76, (1966)
44. E.S. Park, J.Y. Lee, D.H. Kim, A. Gebert, L. Schultz, J. Appl. Phys. 104, 023520 (2008)
45. Y.Q. Cheng, A.J. Cao, H.W. Sheng, E. Ma, *Acta Mater.* **56,** 5263, (2008)
46. X.L. Bian, G. Wang, K.C. Chan, J.L. Ren, Y.L. Gao, Q.J. Zhai, *Appl. Phys. Lett.* **103,** 101907, (2013)
47. S. Papanikolaou, D.M. Dimiduk, W. Choi, J.P. Sethna, M.D. Uchic, C.F. Woodward, S. Zapperi, *Nature* **490,** 517 (2012).

48. B.A. Sun, H.B. Yu, W. Jiao, H.Y. Bai, D.Q. Zhao, W.H. Wang, *Phys. Rev. Lett.* **105,** 035501 (2010)
49. D.V. Louzguine-Luzgin, A. Inoue, *J. Mater. Res,* **21,** 1347 (2006)
50. M. Mansouri, A. Simchi, N. Varahram and E.S. Park, *Mater Sci & Eng A,* **604,** 92 (2014)
51. Y. Liu, G. Schumacher, X.F. Bian, J. Banhart, J. Non Cryst Solids, 422, 26 (2015)
52. T. Egami, Y. Waseda, *J. Non Cryst. Solids,* **64,** 113 (1984)
53. X.W. Fang, C.Z. Wang, Y.X. Yao, Z.J. Ding, K.M. Ho, *Phys. Rev. B,* **83,** 224203 (2011)
54. G.B. Bokas, L. Zhao, J.H. Perepezko, I. Szlufarska, Scr. Mater, 61, 423 (2009)
55. D.R.G. Mitchell, T.C. Petersen, *Microsc. Res. Tech.* **75,** 153 (2012)
56. T.Y. Hsieh, T. Egami, Y. He, S.J. Poon, *J. Non Cryst. Solids,* **135,** 248, (1991)
57. H.Tan, Y. Zhang, D. Ma, Y.P. Feng, Y. Li, *Acta Mater*, **51,** 4551 (2003)
58. Y.E. Kalay, L.S. Chumbley, M.J. Kramer, I.E. Anderson., *Intermetallics,* **18,** 1676 (2010)
59. C. Fan, D.V. Louzguine, C. Li, A. Inoue, *Appl. Phys. Lett,* **75,** 340 (1999)
60. Y.Shen, J.H. Perepezko, *J. Alloy. Compd,* **707,** 3 (2017)
61. J.H. Perepezko, K. Hildal, *Phil Mag,* **86,** 3681 (2006)
62. F. Spaepen, Solid State Phys, 47, 1-32 (1994)
63. D. Turnbull, *Contemp. Phys.* **10,** 473 (1969)
64. K. Kosiba, S. Scudino, R. Kobold, U. Kühn, A. L. Greer, J. Eckert, S. Pauly, *Acta Mater,* **127**, 416 (2017)

65. D.C. Hofmann, J.Y. Suh, A. Wiest, G. Duan, M.L. Lind, M.D. Demetriou, W.L. Johnson, *Nature,* **451,** 1085 (2008)

66. A.L. Greer, *Metal. Mater. Trans.* **A27,** 549 (1996)

67. M.D. Ediger, P. Harrowell, L. Yu, *J. Chem. Phys.* **128**, 034709 (2008)

68. D.Lee, J.J. Vlassak, *Scr Mater,* **165,** 73 (2019)

69. B.Yang, J.W.P. Schmelzer, B.Zhao, Y. Gao, C. Schick, *Scripta Mater,* **162**, 146 (2019)

70. D.L. Messurier, R. Winter, C. M. Martin, *J. Appl. Crystallogr,* **39,** 589 (2006)

71. H.S. Kim, P.J. Warren, B. Cantor, H.R. Lee, *Nanostruct. Mater.* **11,** 241 (1999)

72. K. Hono, Y.Zhang, A. Inoue, T. Sakurai, *Mat. Trans. JIM,* **36,** 909 (1995)

73. C.C. Hays, C.P. Kim, W.L. Johnson, *Phys. Rev Lett,* **84,** 2901 (2000)

74. M.P. Moody, L.T. Stephenson, A.V. Ceguerra, S.P. Ringer, *Microsc. Res. Tech*. **71,** 542 (2008)

75. E. Posan, G. Ujj, A. Kiss, B. Telek, K. Rak, M. Udvardy, A. Inoue, *Prog. Mater. Sci*. **43,** 365 (1998)

76. A. P. Tsai, A. Inoue, T. Masumoto, *Metall. Trans. A.* **19** 1369 (1988)

77. Z. Zhang, W. Zhou, X.Z. Xiong, L.T. Kong, J.F. Li, *Intermetallics* **24,** 1 (2012)

78. X. Hu, J. Guo, G. Fan, T. Feng, *J. Alloys Compd.* **574,** 18 (2013)

79. M.Gao, J.H. Perepezko, *Thermo Acta,* **677,** 91 (2019)

80. A. Inoue, N. Matsumoto, T. Masumoto, *Mater. Trans. JIM*, **31,** 493 (1990)

81. F. Ye, K. Lu, *J. Non-Cryst. Solids*, **262,** 228 (2000)

82. I.S. Gutzow, J.W. Schmelzer, The Vitreous State: Thermodynamics,

Structure, Rheology, and Crystallization, second ed. Springer, Berlin, 2013.

83. I.S. Gutzow, O.V. Mazurin, J.W. Schmelzer, S.V. Todorova, B.B. Petroff, A.I. Priven, Glasses and the Glass Transition, John Wiley & Sons, Weinheim, 2011
84. T.V. Tropin, J.W.P. Schmelzer, C. Schick, *J. Non-Cryst. Solids*, **357,** 1291 (2011)
85. J.W. Schmelzer, *J. Chem. Phys.* **136,** 074512 (2012)
86. J.W.P. Schmelzer, T.V. Tropin, *J. Non-Cryst. Solids,* **407,** 170 (2015)
87. F. Faupel, W. Frank, M.P. Macht, H. Mehrer, V. Naundoft, K. Rätzke, H.R. Schober, S.K. Sharma, H. Teichler, *Rev. Mod. Phys,* **75,** 237 (2003)
88. W. Götze, A. Sjögren, *J. Non-Cryst. Solids,* **161,** 131 (1991)
89. V.M. Fokin, E.D. Zanotto, N.S. Yuritsyn, J.W.P. Schmelzer, *J.Non-Cryst. Solids,* **352,** 2681 (2006)
90. B. Zhang, D.Q. Zhao, M.X. Pan, W.H. Wang, A.L. Greer, Phys. Rev. Lett. 94, 205502 (2005)
91. W.L. Johnson, Fundamental aspects of bulk metallic glass formation in multicomponent alloys, in Materials Science Forum, 1996, Trans Tech Publ
92. L.Q. Xing, A. Mukhopadhyay, W.E. Buhro, K.F. Kelton, *Philos. Mag. Lett.* **84,** 293 (2004)
93. J. Deubener, R. Briickner, M. Sternitzke, *J. Non-Cryst. Solids*, **163,** 1 (1993)
94. Y. Sato, C. Nakai, M. Wakeda, S. Ogata, *Sci. Rep,* **7,** 7194 (2017)
95. Y. Shen, J.H. Perepezko, *J. Non-Cryst. Solids,* **502,** 9 (2018)
96. D. Erdemir, A.Y. Lee, A.S. Myerson, *Chemical Research*, **42,** 621 (2009)
97. Y.Li, JOM, 57, 60 (2005)

98. S. Liu, C. Cui, X. Wang, N. Li, J. Shi, S. Cui, P. Chen, *Metals,* **7,** 204 2017
99. C. Gilbert, R.O. Ritchie, W.L. Johnson, *Appl. Phys. Lett,* **71,** 476 (1997)
100. A.Inoue, T. Zhang, T. Masumoto, *Mater Trans JIM,* **36,** 429 (1994)
101. W.L. Johnson, *MRS Bull,* **24,** 42 1999
102. Y. Leng, T.H. Courtney, *J. Mater. Sci,* **26,** 588 (1991)
103. A.S. Argon, *Acta Metall* **27,** 47 (1979)
104. F. Spaepen. *Acta Metall,* **25,** 407 (1977)
105. H. Bei, Z.P. Lu, E.P. George, *Phy. Rev. Lett,* **93,** 125504 (2004)
106. D. Tönnies, K. Samwer, P. M. Derlet, C. A. Volkert, *Appl. Phy. Lett.* **106,** 171907 (2015)
107. N. Tian, M. Ohnuma, T. Ohkubo, K. Hono, *Mater. Trans.* **46,** 2880 (2005)
108. Y.C. Hu, P.F. Guan, M.Z. Le, C.T. Liu, Y.Yang, H.Y.Bai, W.H.Wang, *Phy. Rev. B,* **93,** 214202, (2016)
109. Y.H. Chen, J.C. Huang, X.H. Du, X. Wang, *Intermetallics,* **68,** 101(2016)
110. R. Limbach, K. Kosiba, S. Pauly, *J. Non-Cryst Solids.* **459,** 130 (2017)
111. A. Bhattacharyya, G. Singh, K. Eswar Prasad, R. Narashimhan, U. Ramanurty, *Mater. Sci. Eng.* **A625**, (2015) 245
112. S. Zhang, T. Ichitsubo, Y. Yokoyama, T. Yamamoto, E. Matsubara, A.Inoue, *Mater. Trans.* **50,** (2009) 1340
113. C.C. Yuan, Z.W.Lv, C.M. Pang, W.W. Zhu, X.L. Wang, B.L, *J. All. Compd*, **806,** 246 (2019)
114. S. Yang, Y.W. Zhang, *J. Appl. Phys.* **95**, (2004) 3655
115. W.H. Li, Keesam Shin, C.G. Lee, B.C. Wei, T.H. Zhang, Y.Z. He, *Mater. Sci. Eng.* **A478,** 371 (2008)

116. E.R. Homer, *Acta Mater,* **63,** 44 (2014)
117. J.Q. Wang, J.H. Perepezko, *J. Chem. Phys,* **145,** 211803 (2016)
118. S.D. Feng, L. Li, K.C. Chan, L. Qi, L. Zhao, L.M. Wang, R.P. Liu, *J. All. Compd,* **770,** 896 (2019)
119. J.O. Krisponeit, S. Pitikaris, K.E. Avila, S. Küchemann, A. Krüger, K. Samwer, *Nat. Commun.* **5,** 3616 (2014)
120. M. Neudecker, S.G. Mayr, *Acta. Mater.* **57,** 1437 (2009)
121. G. Wang, N. Mattern, J. Bednarčík, R. Li, B. Zhang, J. Eckert, *Acta. Mater.* **60,** 3074, (2012)
122. Corey S. O'Hern, Leonardo E. Silbert, Andrea J. Liu, and Sidney R. Nagel, *Phys. Rev. E.* **68,** 011306 (2003)
123. W. Kim, H.S. Oh, E.S. Park, *Intermetallics,* **91,** 8 (2017)
124. X.L. Bian, G. Wang, K.C. Chan, J.L. Ren, Y.L. Gao, Q.J. Zhai, *Appl. Phys. Lett.* **103,** 101907 (2013)
125. D.G. Ast, D.J. Krenitsky, *Mater. Sci. Eng.* **43,** 241 (1980)
126. P.G. Zielinski, D.G. Ast, philos. Mag. 48 811 (1983)
127. Y. Leng, T.H. Courteny, *J. Mater. Sci.* **26,** 588 (1991)
128. E.P. Barth, F. Spaepen, R. Bye, S.K. Das, *Acta. Mater.* **45,** 423 (1997)
129. A.I. Taub, F. Spaepen, *J. Mat. Sci,* **16,** 3087, (1981)
130. A. Banerjee, C.Jiang, L.Lohiya, Y.Yang, Y.Lu, *J. Appl. Phys,* **119,** 155102 (2016)
131. H.Wang, D.Xing, H.Peng, F.Qin, F.Cao, G.Wang, J.Sun, *Scripta Mater,* **66,** 1041 (2012)
132. C. Wang, B.A. Sun, W.H. Wang, H.Y. Bai, *J. Appl. Phys,* **119,** 054902 (2016)

Abstract in Korean

초록

Al-TM-RE 비정질 합금의 나노결정화 거동 및 기계적 특성의 제어

김완

서울대학교 공과대학

재료공학부

비정질 합금은 고비강도, 높은 탄성한계, 내마모성 및 우수한 피로저항성을 가지는 것으로 알려져 있다. 그러나, 집중된 영역에서의 소성변형으로 인한 취성거동으로 인해 비정질 합금을 구조재료로 직접 활용하기에는 한계가 있었다. 비정질 합금에 항복강도 이상의 응력을 인가하면 나노크기의 shear transformation zone(STZ)들의 응집현상을 통해 전단띠가 형성되며, 전단띠의 급격한 성장은 급격한 파괴를 유발한다. 따라서 소성변형능이 개선된 비정질 합금을 개발하기 위해서는 원자/나노 단위에서의 구조적 특성과 이에 따른 비정질 합금의 기계적 특성 변화에 대한 이해가 필수적이다. 다양한 비정질 합금 조성군 중에서 Al-TM-RE (알루미늄-전이금속-희토류금속) 합금시스템의 경우, 비정질 합금의 구조적 변화에 따른 기계적 특성변화를 관찰하기에 적합한 합금 조성으로 알려져 있으며, 본 연구에서는 알루미늄계 비정질 합금의 구조제어 방법 및 이를 통한 기계적 특성 제어와 관련하여 종합적으로 분석하였다.

연질 알루미늄계 비정질 합금의 제조에 대해 최초로 보고된 이후로,

80 at% 이상의 알루미늄을 포함한 Al-TM-RE 시스템에 대해 집중적인 연구가 이루어져 왔다. 선행연구에 따르면, Al-TM-RE 비정질 합금 시스템은 1 GPa 수준의 높은 강도를 가질뿐 아니라, 적절한 열처리를 통해 비정질 기지 내부에 나노크기의 FCC-Al 결정상을 균일하게 석출시킬수 있다고 한다. 85 at%이상의 고알루미늄 조성영역에서 FCC-Al의 불균일 핵생성을 유발하는 Al-MRO (Medium range ordering)을 가지기 때문에 낮은 열처리 온도에서도 FCC-Al의 단독 석출이 가능하다. 또한 알루미늄은 TM 및 RE 원소를 거의 고용하지 못하므로, 열처리를 통해 연질의 FCC-Al을 성장시키면 계면을 따라서 TM 및 RE 원소가 누적된 경질의 solute-enriched area이 형성된다. 이를 통해 FCC-Al의 성장은 Al-TM-RE 비정질 합금의 강도를 최대 1.5 GPa 수준까지도 증가시킬 수 있다. 반면, FCC-Al의 단독석출이 가능한 고알루미늄 비정질 합금에 RE 원소를 다량으로 첨가하게 되면, FCC-Al의 결정화를 유발하는 Al-MRO의 밀도갯수는 감소하는 대신 안정한 RE-centered quasi-equivalent cluster 가 형성되므로 상대적인 비정질 형성능의 향상이 가능하다. RE 원소의 선별적 첨가는 과냉각액체영역 (super-cooled liquid region)의 비약적인 증가 또한 유발시킬수 있다. 이와 같이 넓은 과냉각액체영역을 가진 비정질 합금은 열가소성성형법을 통해 소성변형이 가능하므로, RE 첨가를 통한 과냉각액체영역의 향상은 매우 중요한 요소중 하나이다. 하지만, RE 첨가 비율이 높아지게 되면 일반적으로 알루미늄 비정질 합금은 더욱 취약해진다. 따라서 향상된 기계적 특성과 비정질 형성능을 가진 알루미늄계 비정질 합금의 개발을 이해서는 (1)원자단위구조에 따른 비정질 합금의 열적특성, (2) 조성에 따른 FCC-Al의 동적 핵생성 거동 변화 및 (3)합금첨가에 따른 원자구조와 FCC-Al 석출에 따른 나누구조 변화가 기계적 거동에 미치는 영향에

대한 심층적인 분석이 필수적이다.

본연구에서는 이러한 과학적, 공학적 문제를 해결하기 위해 $Al_{90-x}Ni_{10}RE_x$ (N= Nickel x=2,4,6) 비정질 합금을 이용하여 체계적인 실험을 수행하였다. 첫번째로 RE 원소 첨가 영향을 분석하기 위해 La, Ce, Nd, Gd, Y, Er 희토류 원소를 등가원소비로 다성분계 첨가하였을 때 보이는 알루미늄계 비정질 합금의 열적특성을 분석하였다. 이를 기반으로 높은 비정질 형성능을 가진 $Al_{90-x}Ni_{10}MM_x$ (MM=Ce rich misch metal, x=2,4,6) 비정질 합금 개발하였으며, MM 원소첨가량에 따른 FCC-Al 결정화 거동을 다양한 분석법을 통해 확인하였다. $Al_{90-x}Ni_{10}MM_x$ 합금에서의 FCC-Al의 결정화거동을 이해하기 위해 고분해능 투과전자현미경 (HR-TEM)과 실시간 X-선 산란분석 (In-situ SAXS)를 수행하였고, 이를 통해 가열공정뿐 아니라 냉각속도 제어 공정을 통해서도 FCC-Al 석출상의 크기 및 밀도갯수의 제어가 가능함을 확인하였다. FCC-Al의 독특한 결정화 거동을 설명하기 위해 고전핵생성이론 (classical nucleation theory)를 기반으로 하여, FCC-Al 동적 핵생성거동을 분석하였다. 특히, 고속가열 시차열분석기 (Flash-DSC)를 이용하여 열처리 온도에 따른 FCC-Al 핵생성을 위한 배양시간 (incubation time)을 정확하게 측정 하였다. 온도에 따른 FCC-Al 핵생성 배양시간에 대한 분석을 통해 궁극적으로 FCC-Al의 Time-Temperature-Transition diagram (TTT-diagram)의 작도가 가능하였다. 본 연구에서 제시한 TTT-diagram은 알루미늄 비정질 합금계에서는 최초로 보고되는 결과이다.

TTT-diagram을 기반으로 더욱 세밀한 FCC-Al 석출상의 크기 및 밀도의 제어가 가능하였고, 이를 통해 제조된 다양한 미세구조를 가진 비정질 합금들의 기계적 거동을 나노인덴테이션 분석으로 체계적으로 고

찰하였다. 또한 비정질 합금 리본 굽힘실험 (bending test) 및 반복응력실험 (cyclic tensile test)를 통해 FCC-Al 석출상의 적절한 제어를 통해 강도 및 연성이 동시에 향상 된 (overcoming of strength & ductility trade off) 우수한 특성의 알루미늄계 비정질 합금의 제조가 가능함을 확인하였다.

본 연구를 통해 제한된 비정질 형성능을 가진 알루미늄계 비정질 합금 시스템에서도 TTT-diagram의 작도가 가능하며, 강도와 연신율이 동시에 향상된 우수한 비정질 합금의 제조가 가능함을 확인할 수 있었다. 이러한 분석법은 비단 알루미늄계 뿐 아니라 다양한 비정질 합금 시스템에 보편적으로 적용이 가능한 것으로 기대 되며, 이를 통해 정성적인 분석에만 머물러 왔던 비정질 합금에서의 결정화 거동에 대해 보다 심도 깊은 논의가 가능 할 것으로 기대된다.

핵심어 : 비정질 합금, 동적 핵생성거동, 항온변태곡선, 나노인덴테이션, 고속시차열분석
학 번 : 2014-21450